Alma Mater Studiorum – Università di Bologna

DOTTORATO DI RICERCA IN MECCANICA E SCIENZE AVANZATE DELL'INGEGNERIA: DISEGNO E METODI DELL'INGEGNERIA INDUSTRIALE E SCIENZE AEROSPAZIALI
Ciclo XXIX

Settore Concorsuale di afferenza: 09/A1
Settore Scientifico disciplinare: ING-IND/06

Statistical analysis and modelling aspects of thermally driven turbulence

Presentata da
Riccardo Togni

Relatore
Prof. Elisabetta De Angelis

Coordinatore Dottorato
Prof. Nicolò Cavina

Esame finale anno 2017

Abstract

The present work aims to provide a deeper understanding of thermally driven turbulence and to address some modelling aspects related to the physics of the flow. For this purpose, two idealized systems are investigated by Direct Numerical Simulation: the rotating and non-rotating Rayleigh-Bénard convection. The preliminary study of the flow topologies shows how the coherent structures organise into different patterns depending on the rotation rate. From a statistical perspective, the analysis of the turbulent kinetic energy and temperature variance budgets allows to identify the flow regions where the production, the transport, and the dissipation of turbulent fluctuations occur. To provide a multi-scale description of the flows, a theoretical framework based on the Kolmogorov and Yaglom equations is applied for the first time to the Rayleigh-Bénard convection. The analysis shows how the spatial inhomogeneity modulates the dynamics at different scales and wall-distances. Inside the core of the flow, the space of scales can be divided into an inhomogeneity-dominated range at large scales, an inertial-like range at intermediate scales and a dissipative range at small scales. This classic scenario breaks close to the walls, where the inhomogeneous mechanisms and the viscous/diffusive processes are important at every scale and entail more complex dynamics. The same theoretical framework is extended to the filtered velocity and temperature fields of non-rotating Rayleigh-Bénard convection. The analysis of the filtered Kolmogorov and Yaglom equations reveals the influence of the residual scales on the filtered dynamics both in physical and scale space, highlighting the effect of the relative position between the filter length and the crossover that separates the inhomogeneity-dominated range from the quasi-homogeneous range. The assessment of the filtered and residual physics results to be instrumental for the correct use of the existing Large-Eddy Simulation models and for the development of new ones.

Sommario

Il presente elaborato di tesi ha l'obiettivo di approfondire la comprensione della convezione termica turbolenta e di affrontare alcuni aspetti legati alla modellazione fisica del fenomeno. A tale scopo, due sistemi ideali sono studiati mediante Simulazione Numerica Diretta: la convezione rotante e non-rotante di Rayleigh-Bénard. L'esame preliminare della topologia dei flussi illustra come le strutture coerenti si organizzino in configurazioni differenti a seconda della velocità di rotazione. Da un punto di vista statistico, l'analisi dei bilanci di energia cinetica turbolenta e di varianza di temperatura permette di identificare le regioni nei flussi dove avvengono la produzione, il trasporto e la dissipazione delle fluttuazioni turbolente. Allo scopo di fornire una descrizione scala-per-scala dei flussi, un quadro teorico basato sulle equazioni di Kolmogorov e di Yaglom è esteso per la prima volta alla convezione di Rayleigh-Bénard. L'analisi mostra come l'inomogeneità spaziale influenzi la dinamica a diverse scale e a diverse distanze dalle pareti. Al centro del flusso, lo spazio delle scale può essere diviso in un intervallo a grandi scale dominato dall'inomogeneità, un intervallo inerziale a scale intermedie e un intervallo dissipativo a piccole scale. Questo scenario classico scompare vicino alle pareti, dove i meccanismi indotti dalla inomogeneità spaziale e i processi viscosi e diffusivi sono importanti a tutte le scale e inducono una dinamica più complessa. Lo stesso quadro teorico è esteso ai campi filtrati di velocità e temperatura della convezione non-rotante di Rayleigh-Bénard. L'analisi delle equazioni filtrate di Kolmogorov e di Yaglom mostra l'influenza delle scale residue sulla dinamica filtrata sia nello spazio fisico che nello spazio delle scale, evidenziando l'effetto della posizione reciproca tra la lunghezza del filtro e la scala che separa il range dominato dall'inomogeneità dal range quasi omogeneo. La valutazione della fisica filtrata e della fisica residua risulta importante per l'uso corretto dei modelli attualmente impiegati in simulazione *Large-Eddy* e per lo sviluppo di nuovi.

Dedicato a mia madre, Tina, e a mio padre, Agostino.

Contents

Glossary

$C^u, C^\theta, \widetilde{C}^\theta, c^\theta$ model coefficients.
D fluid domain.
D_c^θ diffusive transport in the physical space of $\langle \delta\theta^2 \rangle$.
D_c^u viscous transport in the physical space of $\langle \delta u^2 \rangle$.
D_r^θ diffusive transfer in the space of scales of $\langle \delta\theta^2 \rangle$.
D_r^u viscous transfer in the space of scales of $\langle \delta u^2 \rangle$.
E^θ dissipation of $\langle \delta\theta^2 \rangle$.
E^u dissipation of $\langle \delta u^2 \rangle$.
$E_e^{\theta'}$ subgrid effective dissipation of $\langle \delta\theta'^2 \rangle$.
E_e^θ effective dissipation of $\langle \delta\theta^2 \rangle$.
$E_e^{u'}$ subgrid effective dissipation of $\langle \delta u'^2 \rangle$.
E_e^u effective dissipation of $\langle \delta u^2 \rangle$.
G filter function.
H distance between the horizontal plates.
H_i subtest heat flux component in the x_i-direction ($= \widehat{u_i^\star \theta^\star} - \hat{\bar{u}}_i^\star \hat{\bar{\theta}}^\star$).
I_c^θ inertial transport in the physical space of $\langle \delta\theta^2 \rangle$.
I_c^u inertial transport in the physical space of $\langle \delta u^2 \rangle$.
$I_r^{\theta'}$ subgrid inertial transfer in the space of scales of $\langle \delta\theta'^2 \rangle$.
I_r^θ inertial transfer in the space of scales of $\langle \delta\theta^2 \rangle$.
$I_r^{u'}$ subgrid inertial transfer in the space of scales of $\langle \delta u'^2 \rangle$.
I_r^u inertial transfer in the space of scales of $\langle \delta u^2 \rangle$.
K, K_N generic kurtosis and kurtosis of the normal distribution.
$K_{w^\star}, K_{\theta^\star}, K_{p^\star}$ kurtosis of $w^\star$, $\theta^\star$ and $p^\star$.
M_{ij}^u scale composite strain-rate tensor ($= \beta_{ij}^u - \hat{\alpha}_{ij}^u$).
M_i^θ scale composite heat flux ($= \beta_i^\theta - \hat{\alpha}_i^\theta$).
N_x, N_y, N_z numbers of fully dealiased modes and polynomials.
Nu Nusselt number ($= \langle q_z \rangle H / \Delta\Theta\kappa$).
Nu_0 Nusselt number in absence of rotation.
Nu_{cd} conductive component of the Nusselt number ($= -d\Theta/dz$).
Nu_{cv} convective component of the Nusselt number ($= \sqrt{PrRa}\,\langle w\theta \rangle$).
P pressure transport in the physical space of $\langle \delta u^2 \rangle$.
Pr Prandtl number ($= \nu/\kappa$).
Pr_t SGS Prandtl number.

$Q_i^\star$ temperature gradient component in the x_i-direction ($= \partial\theta^\star/\partial x_i$).
R autocorrelation function of div_π ($= \langle div_\pi(\boldsymbol{\rho}, z) div_\pi(\boldsymbol{\rho} + \boldsymbol{r}_{\boldsymbol{\rho}}, z)\rangle / div_\pi^2(\boldsymbol{\rho}, z)$).
Ra_c critical Rayleigh number.
Re Reynolds number ($= UH/\nu$).
Ro Rossby number ($= U_f/2\Omega H$).
S, S_N generic skewness and skewness of the normal distribution.
S_{ij} fluctuating strain-rate tensor ($= 0.5\,(\partial u_i/\partial x_j + \partial u_j/\partial x_i)$).
$S_{w^\star}, S_{\theta^\star}, S_{p^\star}$ skewness of $w^\star$, $\theta^\star$ and $p^\star$.
T time period spanned by a DNS.
$T_c^{\theta'}$ subgrid overall transport in the physical space of $\langle \delta\theta'^2 \rangle$.
T_c^{θ} overall transport in the physical space of $\langle \delta\theta^2 \rangle$.
$T_c^{u'}$ subgrid overall transport in the physical space of $\langle \delta u'^2 \rangle$.
T_c^{u} overall transport in the physical space of $\langle \delta u^2 \rangle$.
T_{ij} subtest stresses ($= \widehat{u_i^\star u_j^\star} - \hat{\bar{u}}_i^\star \hat{\bar{u}}_j^\star$).
U generic characteristic velocity or average velocity component in the x-direction.
U_f free-fall velocity ($= \sqrt{g\alpha\Delta\Theta H}$).
U_i average velocity component in the x_i-direction.
X dissipation of the temperature squared ($= 2\,(PrRa)^{-1/2}\,(Q_i^\star Q_i^\star)$).
$\Delta\Theta$ temperature difference between the lower and upper plate.
$\Delta\pi$ difference between the production for $1/Ro > 0$ and $1/Ro = 0$.
$\Delta\tau$ time interval between two consecutive storages.
$\Delta d_c^u, \Delta d_c^w$ difference between the viscous transports for $1/Ro > 0$ and $1/Ro = 0$.
$\Delta e^u, \Delta e^w$ difference between the dissipations for $1/Ro > 0$ and $1/Ro = 0$.
$\Delta i_c^u, \Delta i_c^w$ difference between the inertial transports for $1/Ro > 0$ and $1/Ro = 0$.
Δp difference between the pressure transport for $1/Ro > 0$ and $1/Ro = 0$.
$\Delta p_{sr}^u, \Delta p_{sr}^w$ difference between the pressure-strain rates for $1/Ro > 0$ and $1/Ro = 0$.
$\Delta x, \Delta y, \Delta z$ grid sizes along x, y and z.
Ω rotation rate.
$\Pi^{\theta'}$ subgrid production of $\langle \delta\theta'^2 \rangle$.
Π^{θ} production of $\langle \delta\theta^2 \rangle$.
$\Pi^{u'}$ subgrid production of $\langle \delta u'^2 \rangle$.
Π^{u} production of $\langle \delta u^2 \rangle$.
$\Pi_{\mathbf{II}}^u$ four-times the production of turbulent kinetic energy.
$\Pi_{\mathbf{I}}^u$ four-times the two-point cross-correlation between w and θ.
Θ average temperature.
α thermal expansion coefficient.
α_{ij}^u eddy-viscosity term $\ell_F^2 |\bar{S}^\star| \bar{S}_{ij}^\star$.
α_i^θ eddy-diffusivity term $\ell_F^2 |\bar{S}^\star| \bar{Q}_i^\star$.
$\bar{D}_c^\theta$ resolved diffusive transport in the physical space of $\langle \delta\bar{\theta}^2 \rangle$.
$\bar{D}_c^u$ resolved viscous transport in the physical space of $\langle \delta\bar{u}^2 \rangle$.
$\bar{D}_r^\theta$ resolved diffusive transfer in the space of scales of $\langle \delta\bar{\theta}^2 \rangle$.
$\bar{D}_r^u$ resolved viscous transfer in the space of scales of $\langle \delta\bar{u}^2 \rangle$.

$\bar{E}^{\theta}$ resolved dissipation of $\left\langle \delta\bar{\theta}^2 \right\rangle$.
$\bar{E}^{u}$ resolved dissipation of $\langle \delta\bar{u}^2 \rangle$.
$\bar{E}_e^{\theta}$ resolved effective dissipation of $\left\langle \delta\bar{\theta}^2 \right\rangle$.
$\bar{E}_e^{u}$ resolved effective dissipation of $\langle \delta\bar{u}^2 \rangle$.
$\bar{I}_c^{\theta}$ resolved inertial transport in the physical space of $\left\langle \delta\bar{\theta}^2 \right\rangle$.
$\bar{I}_c^{u}$ resolved inertial transport in the physical space of $\langle \delta\bar{u}^2 \rangle$.
$\bar{I}_r^{\theta}$ resolved inertial transfer in the space of scales of $\left\langle \delta\bar{\theta}^2 \right\rangle$.
$\bar{I}_r^{u}$ resolved inertial transfer in the space of scales of $\langle \delta\bar{u}^2 \rangle$.
$\bar{P}$ resolved pressure transport in the physical space of $\langle \delta\bar{u}^2 \rangle$.
$\bar{Q}_i$ resolved fluctuating temperature gradient $(= \partial\bar{\theta}/\partial x_i)$.
$\bar{S}_{ij}$ resolved fluctuating strain-rate tensor $(= 0.5\,(\partial\bar{u}_i/\partial x_j + \partial\bar{u}_j/\partial x_i))$.
$\bar{T}_c^{\theta}$ resolved overall transport in the physical space of $\left\langle \delta\bar{\theta}^2 \right\rangle$.
$\bar{T}_c^{u}$ resolved overall transport in the physical space of $\langle \delta\bar{u}^2 \rangle$.
$\bar{\Pi}^{\theta}$ resolved production of $\left\langle \delta\bar{\theta}^2 \right\rangle$.
$\bar{\Pi}^{u}$ resolved production of $\langle \delta\bar{u}^2 \rangle$.
$\bar{\chi}$ dissipation of resolved temperature variance $(= 2\,(PrRa)^{-1/2}\left(\partial\bar{\theta}/\partial x_j\right)\left(\partial\bar{\theta}/\partial x_j\right))$.
$\bar{\pi}^{\theta}$ production of resolved temperature variance.
$\bar{\pi}^{u}$ production of resolved turbulent kinetic energy.
$\bar{\tilde{\epsilon}}$ pseudo-dissipation of resolved energy $(= \sqrt{Pr/Ra}\,(\partial\bar{u}_i/\partial x_j)\,(\partial\bar{u}_i/\partial x_j))$.
$\bar{k}$ instantaneous resolved turbulent kinetic energy $(= 0.5\bar{u}_i\bar{u}_i)$.
$\bar{t}_c^{u}$ overall transport along z of resolved turbulent kinetic energy.
$\bar{t}_c^{\theta}$ overall transport along z of resolved temperature variance.
β generic variable.
β_{ij}^{u} test filter eddy-viscosity term $4\ell_F^2|\hat{\bar{S}}^{\star}|\hat{\bar{S}}_{ij}^{\star}$.
β_i^{θ} test filter eddy-diffusivity term $4\ell_F^2|\hat{\bar{S}}^{\star}|\hat{\bar{Q}}_i^{\star}$.
$\boldsymbol{\rho}$ position vector in the horizontal planes $(= (x, y))$.
$\boldsymbol{r_\rho}$ separation vector in the horizontal planes $(= (r_x, r_y))$.
$\boldsymbol{r}$ separation vector $(= (r_x, r_y, r_z))$.
χ dissipation of temperature variance $(= 2(PrRa)^{-1/2}(\partial\theta/\partial x_i)(\partial\theta/\partial x_i))$.
χ' dissipation of subgrid temperature variance $(= 2(PrRa)^{-1/2}(\partial\theta'/\partial x_i)(\partial\theta'/\partial x_i))$.
χ_{sgs} subgrid dissipation of resolved temperature variance $(= -2h_i\bar{Q}_i)$.
$\delta\theta$ fluctuating temperature increment $(= \theta(x_j + r_j/2, t) - \theta(x_j - r_j/2, t))$.
δ_θ thermal boundary layer thickness based on the maximum of $\langle u^2 \rangle (= \arg\max_{z\in[0,0.5]} \langle \theta^2 \rangle)$.
δ_θ^{sl} thermal boundary layer thickness based on the average temperature profile at the wall $(= (2d\Theta/dz|_{z=0})^{-1})$.
δ_{ij} Kronecker delta.
δ_u viscous boundary layer thickness $(= \arg\max_{z\in[0,0.5]} \langle u^2 \rangle)$.
$\delta f_i^{u}, \delta f_i^{\theta}$ velocity and thermal forcing increments.
$\delta u, \delta v, \delta w$ components of the fluctuating velocity increment in the x-, y- and z-directions.
δu_i fluctuating velocity increment $(= u_i(x_j + r_j/2, t) - u_i(x_j - r_j/2, t))$.

$\delta u_{\|}$ longitudinal velocity increment ($= \delta u_i r_i / r$).
$\delta u_\rho, \delta u_\phi, \delta w$ components of the fluctuating velocity increment in the ρ-, ϕ- and z-directions.
ℓ_0 generic integral length scale (e.g., $\int_0^\infty \left(\langle w(\boldsymbol{\rho}, z) w(\boldsymbol{\rho} + \boldsymbol{r_\rho}, z)\rangle \,/\, \langle w^2\left(\boldsymbol{\rho}, z\right)\rangle\right) dr_\rho$).
ℓ_F filter length.
ℓ_b^θ temperature boundary scale.
ℓ_b^u velocity boundary scale.
ℓ_c qualitative separation between ascending and descending clusters of plumes.
ℓ_c^θ temperature crossover scale.
ℓ_c^u velocity crossover scale.
$\ell_{b,min}^\theta$ smallest temperature boundary scale ($= \min\left(\ell_b^\theta\right)$).
$\ell_{b,min}^u$ smallest velocity boundary scale ($= \min\left(\ell_b^u\right)$).
$\ell_{c,min}^\theta$ smallest temperature crossover scale ($= \min\left(\ell_c^\theta\right)$).
$\ell_{c,min}^u$ smallest velocity crossover scale ($= \min\left(\ell_c^u\right)$).
ϵ dissipation of turbulent kinetic energy ($= 2\sqrt{PrRa}\left(S_{ij} S_{ij}\right)$).
ϵ_{ijk} Levi-Civita symbol.
ϵ_{sgs} subgrid dissipation of resolved turbulent kinetic energy ($= -\tau_{ij}\bar{S}_{ij}$).
η_b Batchelor length scale ($= \left(PrRa\right)^{-3/8} \epsilon^{-1/4}$).
η_k Kolmogorov length scale ($= \left(Pr/Ra\right)^{3/8} \epsilon^{-1/4}$).
$\hat{\rho}_i$ radial unit vector.
κ thermal diffusivity.
$\mathcal{E}_i$ resolved turbulent heat flux ($= \widehat{\bar{u}_i^\star \bar{\theta}^\star} - \hat{\bar{u}}_i^\star \hat{\bar{\theta}}^\star$.
$\mathcal{L}_{ij}$ resolved turbulent stresses ($= \widehat{\bar{u}_i^\star \bar{u}_j^\star} - \hat{\bar{u}}_i^\star \hat{\bar{u}}_j^\star$).
ν kinematic viscosity.
$\omega^\star$ component of the vorticity in the z-direction ($= \partial v^\star / \partial x - \partial u^\star / \partial y$).
$\pi^{\theta'}$ production of subgrid temperature variance.
$\pi^{u'}$ production of subgrid turbulent kinetic energy.
ρ, ϕ, z cylindrical coordinates.
σ reciprocal of a characteristic subgrid time scale.
$\tau_{ij}^\star$ subgrid-scale stress tensor ($= \overline{u_i^\star u_j^\star} - \bar{u}_i^\star \bar{u}_j^\star$).
τ_{ij} fluctuating subgrid-scale stress tensor.
θ fluctuating temperature.
$\tilde{\epsilon}$ pseudo-dissipation of turbulent kinetic energy ($= \sqrt{Pr/Ra}\left(\partial u_i / \partial x_j\right)\left(\partial u_i / \partial x_j\right)$).
$\tilde{\epsilon}'$ pseudo-dissipation of subgrid energy ($= \sqrt{Pr/Ra}\left(\partial u_i' / \partial x_j\right)\left(\partial u_i' / \partial x_j\right)$).
$\tilde{\epsilon}_x, \tilde{\epsilon}_y, \tilde{\epsilon}_z$ contributions of u, v and w to the pseudo-dissipation.
$\tilde{r}_\rho$ separation that maximizes Π^u ($= \underset{r_\rho \in [0,4]}{\arg\max}\, \Pi^u$).
div_π horizontal divergence of the velocity field ($= \partial u^\star / \partial x + \partial v^\star / \partial y$).
f_i^u, f_i^θ homogeneous, external velocity and thermal forcing.
g gravitational acceleration.
$h_i^\star$ subgrid-scale heat flux ($= \overline{u_i^\star \theta^\star} - \bar{u}_i^\star \bar{\theta}^\star$).
h_i fluctuating subgrid-scale heat flux.

h_ρ, h_ϕ, h_z components of the fluctuating SGS heat flux in the ρ-, ϕ- and z-directions.
i, j, k indexes.
k instantaneous turbulent kinetic energy (or simply energy) $(= 0.5 u_i u_i)$.
k' instantaneous subgrid turbulent kinetic energy $(= 0.5 u_i' u_i')$.
l_x, l_y, l_z sizes of the computational domain along x, y and z.
p fluctuating pressure.
q_z dimensional vertical heat flux $(= \theta^\star w^\star - \kappa \partial \theta^\star / \partial z)$.
r magnitude of $\boldsymbol{r}$.
r_i separation component in the x_i-direction.
r_x, r_y, r_z separation components in the x-, y- and z-directions.
r_ρ, r_ϕ, r_z separation components in the ρ-, ϕ- and z-directions.
t time.
$t_c^{\theta'}$ overall transport along z of subgrid temperature variance.
$t_c^{u'}$ overall transport along z of subgrid turbulent kinetic energy.
$t_{c,sgs}^{u}$ subgrid-scale transport of resolved turbulent kinetic energy.
$t_{c,sgs}^{\theta}$ subgrid-scale transport of resolved temperature variance.
u, v, w fluctuating velocity components in the x-, y- and z-directions.
u_i fluctuating velocity component in the x_i-direction.
x, y, z Cartesian coordinates.
x_i tensor coordinates, where $x = x_1$, $y = x_2$ and $z = x_3$.
z_{max} location of the maximum Ekman pumping $(= \arg\max_{z \in [0,0.5]} d \langle kw \rangle / dz)$.
$\bar{\cdot}$ filtering operation.
$\cdot'$ residual or subgrid component $(\beta' = \beta - \bar{\beta})$.
$\cdot^\dagger$ mid-point average $(\beta^\dagger = (\beta(x_j - r_j/2) + \beta(x_j + r_j/2))/2)$.
$\cdot^*$ normalization with respect to H/Nu.
$\cdot^\star$ fluctuating plus average component $(\beta^\star = \beta + \langle \beta \rangle)$.
$\cdot^{\mathbf{I}}, \cdot^{\mathbf{II}}$ quantity evaluated at points x_i^{I} and x_i^{II} respectively.
$\hat{\cdot}$ test filtering operation.
$\langle \cdot \rangle_+$ conditional average $(\langle \beta \rangle_+ = \langle \beta \rangle$ for $\beta > 0)$.
$\langle \cdot \rangle_-$ conditional average $(\langle \beta \rangle_- = \langle \beta \rangle$ for $\beta < 0)$.
$\langle \cdot \rangle_V$ volume average.
$\langle \cdot \rangle$ spatial and ensemble average.
$\langle \delta\theta^2 \rangle$ second-order temperature structure function $(= \langle \delta\theta \delta\theta \rangle)$.
$\langle \delta u^2 \rangle$ second-order velocity structure function $(= \langle \delta u_i \delta u_i \rangle)$.
$|\bar{S}^\star|$ characteristic resolved strain-rate $(= \sqrt{2 \bar{S}_{ij}^\star \bar{S}_{ij}^\star})$.

DNS Direct Numerical Simulation.

LES Large-Eddy Simulation.

p.d.f. probability density function.

RANS Reynolds-averaged Navier-Stokes.

RBC Rayleigh-Bénard convection.
RRBC rotating Rayleigh-Bénard convection.

SGS subgrid-scale.

Chapter 1

Introduction

Now as in the past, thermally driven turbulence represents a crucial subject in a wide range of sciences due to its relevance in nature and technology. Many examples of notable interest include geophysical flows like atmospheric convection [39], oceanic deep circulation [60] and the overturning of liquid metal in Earth's outer core [13], which sustains and eventually reverses the magnetic field that shields our planet from cosmic radiations [34]. In the astrophysical context, the fluid motions in the outer layer of the Sun [14] and giant planets [10] are driven and sustained essentially by temperature differences. Thermally driven turbulence is of relevant importance also in technological processes like the controlled growth of crystals from the melt in metal production [6] and industrial flows ranging from the passive cooling of nuclear reactors to indoor circulations in buildings and passenger cabins [35].

The processes mentioned in the previous paragraph, although extremely complex, are governed by the deterministic equations of hydrodynamics, namely the Navier-Stokes equations, plus some case-specific relations like the Maxwell's equations when the magneto-fluid dynamic interactions are relevant [94] or the equations for the flow phases in case of moist convection [97]. Although an accurate mathematical model can usually be derived starting from fundamental principles, an important limitation exists regarding the capability to solve it and, consequently, to predict the evolution in time of the relevant flow fields.

The analytic solution of the Navier-Stokes equations can be obtained only for a limited set of problems and just a few of them are of practical interest due to the simple geometries involved and the low Reynolds numbers needed to ensure the laminar regime. The most straightforward approach to solve turbulence is the Direct Numerical Simulation (DNS), where the governing equations are discretized and numerically solved. The mesh size and the time step must be small enough to capture all the length and time scales that naturally arise in turbulent flows. If the model is correct, the DNS provides a solution that is only affected by the errors introduced by the numerical discretization, thus the use of highly-accurate and high-order schemes is beneficial to get better results; these schemes, on the other hand, scarcely adapt to complex geometries and boundary conditions (considering, e.g., the spectral methods

[12]). Second and more important, the ranges of length and time scales that a DNS needs to resolve (i.e. from the smallest dissipative Kolmogorov scales to the largest scales imposed by boundary conditions or external forcing) dramatically increase with the turbulence intensity and the resolution requirement, expressed as the total number of grid points and time steps employed by the computation, results to be proportional to the 11/4 power of the Reynolds number. Therefore, most of the flows that are of interest in engineering and atmospheric studies are far beyond the capability of modern-day computers in terms of memory size and CPU performance, and DNS remains limited to low turbulent Reynolds numbers.

A different approach, the Large-Eddy Simulation (LES), numerically solves the large and more energetic scales of turbulence, whereas it models the effect of the small and dissipative ones. The accuracy of the solution relies mainly upon the capability of the model to reproduce the unresolved or subgrid dynamics, which is argued to be more universal and less affected by the boundary conditions with respect to the large-scale dynamics and, thus, easier to parameterize in terms of resolved quantities [71]. The latter scenario, conceptually introduced by Richardson [78] and formalized later by Kolmogorov [48], represents a good approximation for free-shear turbulence and for wall-bounded flows, provided to be sufficiently distant from the solid boundaries. In these cases, purely dissipative, eddy-viscosity models have been proved to satisfactorily reproduce the energy transfer between resolved and subgrid motion, as they can mimic the average direct cascade that naturally develops from large, energy-producing to small, dissipative scales.

The energetic eddies that need to be solved are very small close to the walls when high Reynolds numbers are considered, hence they are inevitably filtered out in LES of practical interest due limited computing capacities. On the other hand, the inhomogeneous and non-universal processes occurring at subgrid level in the proximity of solid boundaries cannot be accounted for by the eddy-viscosity closures; thus, different models need to be considered that adapt specifically to each class of flows due to the lack of universality of the subgrid scales. Evidently, the possibility to formulate a reliable closure depends on the degree of knowledge of the small-scale dynamics, which apparently can be provided only by experiments since DNS cannot solve flows at engineering and geophysical sizes. The experimental approach, on the other hand, is limited by the feasibility of the setup and the possibility to acquire some statistical quantities with both ease and accuracy; let us consider, as an example, all the technical issues in the measurement of the velocity and temperature fields in the atmospheric boundary layer [77].

The scenario depicted in the previous paragraphs points out the inherent challenge of predicting turbulent flows, even though an accurate model, i.e. the Navier-Stokes equations, is well known since the nineteenth century. An alternative approach that led to substantial breakthroughs in turbulence studies investigates a simplified and more treatable system, which preserves the essential features of more complex and practically relevant flows, by means of DNS, experiments, or theoretical analysis [1]. This methodology still suffers from the limitation of applicability

to low Reynolds numbers and simple geometries for feasibility reasons; however, we can arguably extend the results obtained for the canonical flow to the actual systems based on a conceptual rather than rigorous similarity. The knowledge that can be obtained following this approach has proved to be essential for the development of reliable models and, more in general, for the theoretical understanding of the turbulent phenomenon [85].

A paradigmatic system that contains the main physics of thermal convection, namely the balance between buoyant and viscous forces, is the Rayleigh-Bénard convection, which is generally defined as a fluid layer confined between two horizontal plates, heated from below and cooled from above [18]. In this thesis, the aforementioned system is numerically investigated both in absence and in presence of a background rotation by employing DNS data sets. As it will be thoroughly explained in the next sections of the introduction, this study is valuable from both a theoretical side, e.g. for the advancement of the phenomenological theory of thermal convection, and a practical side, as a starting point for the development of more reliable and physics-based models to be employed, for example, in LES.

1.1 The Rayleigh-Bénard system

Let us define the problem under investigation. We consider an incompressible fluid enclosed between two horizontal and infinite plates, where the temperature difference between the lower warm and the upper cold one is constant. The plates can be either static or rotating around a vertical axis directed opposite to the gravitational acceleration; in the first case, the system is called Rayleigh-Bénard convection (RBC), otherwise it is referred to as rotating Rayleigh-Bénard convection (RRBC).

For sufficiently small temperature differences and rotation rates, the material properties of the fluid can be assumed to be constant and the buoyancy force to be a linear function of temperature [89]. Within this approximation, attributed to Oberbeck [63] and Boussinesq [5], the governing equations of RRBC are the following continuity, momentum and temperature equations,

$$\frac{\partial u_i^\star}{\partial x_i} = 0, \tag{1.1a}$$

$$\frac{\partial u_i^\star}{\partial t} + \frac{\partial u_i^\star u_j^\star}{\partial x_j} + \frac{1}{Ro}\epsilon_{i3k}u_k^\star = -\frac{\partial p^\star}{\partial x_i} + \sqrt{\frac{Pr}{Ra}}\frac{\partial^2 u_i^\star}{\partial x_j \partial x_j} + \theta^\star \delta_{i3}, \tag{1.1b}$$

$$\frac{\partial \theta^\star}{\partial t} + \frac{\partial \theta^\star u_i^\star}{\partial x_i} = \frac{1}{\sqrt{PrRa}}\frac{\partial^2 \theta^\star}{\partial x_i \partial x_i}, \tag{1.1c}$$

where $i, j, k = 1, 2, 3$ (the summation over repeated indexes in implied), ϵ_{ijk} is the Levi-Civita symbol, δ_{ij} is the Kronecker delta and the variables $u^\star = u_1^\star$, $v^\star = u_2^\star$, $w^\star = u_3^\star$, $p^\star$ and $\theta^\star$ are, in order, the velocity components, the pressure and the temperature. The Cartesian coordinate system $(x, y, z) = (x_1, x_2, x_3)$ is solidal with

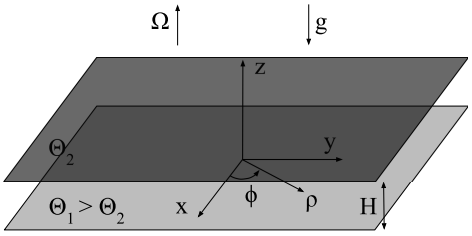

Figure 1.1: Sketch of the setup.

the plates, having the x, y axis along the horizontal directions and the vertical z axis pointing in the direction opposite to that of gravitational acceleration; see the sketch in figure 1.1. Equations (1.1)(a-c) are expressed in a non-dimensional form by employing the distance between the plates H, their temperature difference $\Delta\Theta$ and the free-fall velocity $U_f = \sqrt{g\alpha\Delta\Theta H}$ as characteristic scales, where g and α are the gravitational acceleration and the thermal expansion coefficient.

Three non-dimensional parameters drive the dynamics of the system, namely the Rayleigh number $Ra = g\alpha\Delta\Theta H^3/\nu\kappa$, the Rossby number $Ro = U_f/2\Omega H$ and the Prandtl number $Pr = \nu/\kappa$, where ν, κ and Ω are the kinematic viscosity, the thermal diffusivity and the angular frequency. The Rayleigh and the Rossby numbers indicate the ratio of buoyancy to viscous/diffusive damping, and buoyancy to Coriolis force respectively, whereas the Prandtl number compares viscous momentum and diffusive heat transports. In the limiting case of Ro approaching infinity, the Coriolis force $(1/Ro)\epsilon_{i3k}u_k^\star$ becomes equal to zero and the equations (1.1)(a-c) converge to the set for the non-rotating convection. The response of RBC and RRBC to the input parameters is generally quantified by the non-dimensional heat flux, namely the Nusselt number $Nu = \langle q_z \rangle H/\Delta\Theta\kappa$, and by the Reynolds number $Re = UH/\nu$, where q_z is the vertical heat flux, U is a characteristic velocity (e.g. a root-mean-square velocity) and $\langle\cdot\rangle$ denotes the spatial average along the homogeneous directions x and y, and the ensemble average over the different configurations.

A classic result of linear stability analysis states that convection in absence of rotation may occur only for Rayleigh numbers larger than the critical value $Ra_c = 1708$, otherwise the fluid is at rest and the equilibrium solution is stable [16]. Above the onset of convection, RBC eventually undergoes a series of transitions, depending on the Prandtl number, from steady motion organised in parallel roll cells to fully-developed turbulence without any permanent spatial pattern. Fully-developed turbulent RBC presents a highly fluctuating and nearly isothermal region in the interior and boundary layers close to the plates where the viscous and diffusive effects are important and the heat is transported essentially by conduction. The instability of the thermal boundary layers triggers the eruption of fluid from the near-wall region, giving rise to ascending and descending plumes which move into the core and broaden through diffusion and turbulent mixing [43].

The study of turbulent RBC is nowadays oriented towards four major direc-

tions. The one that most draws attention for technical purposes is the development of theoretical models aimed at predicting the Nusselt and the Reynolds numbers as a function of the Rayleigh and the Prandtl numbers. In this framework, Grossmann and Lohse [36] proposed a set of scaling laws that have been found to fit experimental and numerical data over a wide range of input parameters, however it is not clear if the unifying theory holds at very large Ra within the ultimate regime theorized by Kraichnan [50]. The effect of buoyancy on turbulence statistics represents another major challenge. Although it has been predicted by dimensional arguments several decades ago [4, 64], the occurrence of a Bolgiano-Obukhov scaling followed by a Kolmogorov one in RBC is a current subject of debate as conclusive experimental and numerical evidences are still missing [57]. The other two subjects of interest are the coherent structures and the boundary layers. These aspects are strictly interconnected and play a fundamental role in the transport of heat and momentum, thus much effort has been made to study these topics in order to advance phenomenological theories and refine models of RBC [37, 88].

Rotating the convective system around its vertical axis introduces a new set of phenomena that have been the focus of many fruitful investigations in the last decades, starting from the early works by Chandrasekhar [15] and Rossby [80] to modern-day experimental and numerical campaigns [87]. The research on RRBC has been catalyzed for years by the observation of a clear enhancement in the heat transport with respect to the non-rotating case occurring in a small portion of the Ra-Pr-Ro phase space. In terms of non-dimensional quantities, the Nusselt number in the rotating case may exceed the one in absence of rotation, i.e. $Nu/Nu_0 > 1$, where $Nu_0 = Nu(1/Ro = 0)$. This appealing phenomenon contradicts another typical feature of rotating flows, which is the stabilizing effect due to the suppression of vertical motion as predicted by the Taylor-Proudman theorem [89]. The latter phenomenology is responsible for the delay in the onset of convection, as Ra_c increases with $1/Ro$ according to linear stability analysis [15], and for the reduction of the heat transport at sufficiently high rotation rates with Ra and Pr kept constant.

The RBC exemplifies many of the startling aspects of thermally driven flows, however the addiction of a complexity like the background rotation reveals how much diversified turbulent thermal convection could be in real world. The high level of complexity achievable with a simple geometry encouraged the study of RBC and RRBC in the last years and still represents a topic of great interest in the scientific community. This work accepts some challenges of thermally driven turbulence by assessing the dynamics of these canonical flows and by outlining a novel approach to LES modelling, as it will be discussed in more detail in the next section.

1.2 Objectives and data sets

This thesis aims at studying the complex phenomenon of thermally driven turbulence by means of two canonical flows, the Rayleigh-Bénard convection with and without

rotation, and analyzing some modelling aspects that are relevant in LES.

Regarding the first objective, a combination of classic and novel strategies is employed to rationalize the dynamics of RBC and RRBC. A qualitative analysis of the instantaneous velocity and temperature fields provides the reader with a first overview of the flows and allows us to draw some interesting conclusions concerning the nature of the coherent structures that develop in the systems, namely the thermal plumes. Clearly, a picture based uniquely on the flow topology is not sufficient to describe the details of the complex mechanisms interwoven in thermally driven turbulence; thus, the study proceeds by considering a statistical analysis of the single-point budgets of turbulent kinetic energy and temperature variance. Although being assessed by previous works, the single-point approach leads to some novel results that complete the mechanistic description of the flow topology.

As mentioned before, turbulence is a multi-scale phenomenon, in the sense that different length and time scales are involved in it. The classic single-point analysis does not allow to capture the turbulent processes occurring at different length scales; thus, a novel approach is needed to obtain a complete description. For this purpose, a theoretical framework based on the budgets of two-point statistics is introduced. These are the equations for the second-order velocity and temperature structure functions, the so-called Kolmogorov and Yaglom equations, which have been previously employed only by a few authors and never in the case of thermally driven flows like RBC or RRBC [28, 59, 23, 90]. Here, it is worth anticipating that these equations allow us to rigorously assess the different flow mechanisms both at different scales and locations inside the fluid domain; consequently, they represent the ideal mathematical tool for the study of turbulent phenomena in general.

Beside providing detailed and novel information about the physics of RBC and RRBC, the first part of the thesis paves the way to the comprehension of the resolved and subgrid dynamics of thermally driven turbulence. This task is of primary importance in LES, where a filtering operation is employed to separate the large, energetic scales from the small, dissipative ones, and a model is needed to reproduced the effect of the residual fields. That said, the main goals of the second part are to investigate the capability of the resolved velocity and temperature fields to correctly reproduce the dynamics of RBC and to evaluate the effect of the subgrid scales on the resolved quantities. In particular, the filtered single-point and scale-by-scale budgets are analyzed for the purpose of assessing the filtered physics at different scales, locations in the fluid domain and filter lengths, and for the development of a physics-based model that better reproduces the behaviour of the subgrid scales.

The results presented in this thesis come from a set of DNS performed at the same Prandtl number, $Pr = 0.7$, at three Rayleigh numbers, $Ra = 1.7 \times 10^5$, $Ra = 1.0{\times}10^6$, $Ra = 1.0{\times}10^7$, and for non-dimensional rotation rates $1/Ro$ spanning from 0 to 3.33; see table 1.1. The governing equations (1.1)(a-c) are solved using a pseudospectral method that discretizes the space with Chebyshev polynomials in the z direction and with Fourier modes in the x and y directions. Time integration is performed with a fourth-order Runge-Kutta scheme for the nonlinear terms and

Case	Ra	$1/Ro$	$N_x \times N_y \times N_z$	$\frac{\Delta_x}{\langle\eta_k\rangle_{min}}$	$\frac{\Delta_z}{\langle\eta_k\rangle}\Big\vert_{z=0}$	$\frac{\Delta_z}{\langle\eta_k\rangle}\Big\vert_{z=0.5}$	$\Delta\tau$	T
DNS 1	1.7×10^5	0	$128 \times 128 \times 129$	3.40	0.081	0.381	20	890
DNS 2	1.0×10^6	0	$256 \times 256 \times 129$	3.13	0.015	0.704	10	500
DNS 3	1.0×10^7	0	$540 \times 540 \times 257$	3.35	0.009	0.766	5	255
DNS 4	1.0×10^7	0.17	$540 \times 540 \times 257$	3.34	0.008	0.772	2	150
DNS 5	1.0×10^7	0.33	$540 \times 540 \times 257$	3.31	0.008	0.790	2	150
DNS 6	1.0×10^7	0.4	$540 \times 540 \times 257$	3.33	0.008	0.789	2	150
DNS 7	1.0×10^7	0.5	$540 \times 540 \times 257$	3.36	0.009	0.783	2	150
DNS 8	1.0×10^7	0.67	$540 \times 540 \times 257$	3.41	0.009	0.773	2	100
DNS 9	1.0×10^7	1	$540 \times 540 \times 257$	3.48	0.009	0.758	2	100
DNS 10	1.0×10^7	1.43	$540 \times 540 \times 257$	3.58	0.009	0.745	2	100
DNS 11	1.0×10^7	2	$540 \times 540 \times 257$	3.69	0.009	0.728	2	100
DNS 12	1.0×10^7	3.33	$540 \times 540 \times 257$	3.89	0.010	0.684	2	100

Table 1.1: Parameters of the simulations.

a second-order-accurate Crank-Nicolson scheme for the linear ones. For further details on the numerical scheme the reader is referred to the technical paper by Lundbladh *et al.* [58]. The computational domain is a rectangular box of height one and lateral sizes $l_x = 8$, $l_y = 8$ along x, y respectively, where the Cartesian coordinate system is centered at the lower wall, as sketched in figure 1.1. Periodic boundary conditions are imposed at the lateral sidewalls, whereas isothermal and no-slip boundary conditions are used on the top and bottom plates.

The DNS approach requires the numbers of fully dealiased modes (N_x, N_y) and polynomials (N_z) to be sufficiently high to resolve all the degrees of freedom in the system. The smallest length scales of motion and temperature are estimated, in order, by the Kolmogorov length scale $\eta_k = (Pr/Ra)^{3/8}\epsilon^{-1/4}$ and the Batchelor length scale $\eta_b = (PrRa)^{-3/8}\epsilon^{-1/4}$, where $\epsilon = 2\sqrt{Pr/Ra}(S_{ij}S_{ij})$ is the dissipation rate of turbulent kinetic energy, $S_{ij} = 0.5\,(\partial u_i/\partial x_j + \partial u_j/\partial x_i)$ is the fluctuating strain-rate tensor and the quantities without the star superscript denote hereafter the fluctuating components. The Prandtl number considered in this work is less than one, thus the minimum resolution requirement is set by the velocity field as $\eta_k/\eta_b = Pr^{3/4} < 1$. Let us consider a mesh in physical space where the nodes are uniformly spaced along the horizontal directions with separations $\Delta_x = l_x/N_x$ and $\Delta_y = l_y/N_y$, and non-uniformly distributed along the vertical direction in correspondence of the Chebyshev collocation points with separation $\Delta_z = \Delta_z(z)$. Locally, the grid spacings Δ_x, Δ_y and Δ_z should be of the same order of the average Kolmogorov length scale $\langle\eta_k\rangle = \langle\eta_k\rangle\,(z)$. Previous DNS of RBC have been proved to give accurate results with mesh sizes up to four times $\langle\eta_k\rangle$ [44, 93], in agreement with the notion that the Kolmogorov length scale in general underestimates the actual size of dissipative motions by more than a factor of two [75].

The average Kolmogorov length scale is computed *a posteriori* from the data

Case	$\langle Nu \rangle_V$	$1+\sqrt{RaPr}\,\langle w\theta \rangle_V$	$1+\sqrt{RaPr}\,\langle \epsilon \rangle_V$	$0.5\sqrt{RaPr}\,\langle X \rangle_V$
DNS 1	5.00	4.98	5.00	5.01
DNS 2	8.16	8.18	8.16	8.17
DNS 3	15.54	15.54	15.50	15.52
DNS 4	15.67	15.67	15.69	15.69
DNS 5	16.07	16.07	16.08	16.08
DNS 6	16.10	16.10	16.11	16.12
DNS 7	16.10	16.10	16.10	16.10
DNS 8	15.98	15.98	15.98	15.98
DNS 9	15.60	15.60	15.60	15.60
DNS 10	15.02	15.02	15.02	15.03
DNS 11	14.21	14.21	14.20	14.20
DNS 12	12.31	12.32	12.33	12.33

Table 1.2: Terms of the exact relation $\langle Nu \rangle_V = 1+\sqrt{RaPr}\,\langle w\theta \rangle_V = 1+\sqrt{RaPr}\,\langle \epsilon \rangle_V = 0.5\sqrt{RaPr}\,\langle X \rangle_V$ calculated from the different data sets.

sets and compared with the employed grid spacings. As shown in table 1.1, the criterion is satisfied along the horizontal direction as $\Delta_x = \Delta_y$ is smaller than four-times the minimum average Kolmogorov length scale $\langle \eta_k \rangle_{min} = \langle \eta_k \rangle (z = 0)$ for every DNS. The vertical grid spacing Δ_z is always smaller or almost equal to $\langle \eta_k \rangle$, thus the resolution is stricter than necessary. Moreover, the number of grid points clustered within the thinnest boundary layer, that could be either the viscous or the thermal one depending on $1/Ro$, is at least 25, which is more than acceptable when considering that 6 nodes are sufficient to give accurate results [93].

Another way to assess the DNS resolution is by checking whether or not the consistency relation $\langle Nu \rangle_V = 1+\sqrt{RaPr}\,\langle w\theta \rangle_V = 1+\sqrt{RaPr}\,\langle \epsilon \rangle_V = 0.5\sqrt{RaPr}\,\langle X \rangle_V$ (which can be exactly derived from the governing equations (1.1)*a-c*) is fulfilled by the numerical data sets [93]. Here, $\langle \cdot \rangle_V$ denotes the spatial average over the whole fluid domain and over different configurations and $X = 2(PrRa)^{-1/2}\,(Q_i^\star Q_i^\star)$ is the dissipation of the temperature squared, where $Q_i^\star = \partial\theta^\star/\partial x_i$. The volume-averaged Nusselt number $\langle Nu \rangle_V$ deviates from the other terms of the equation by less than 0.5%, thus the criterion is satisfied within a good approximation and the DNS can be considered adequately resolved; see table 1.2. For the sake of statistical convergence, each DNS is run at least for a time period $T = 100$, which corresponds to fifty-times the large-eddy-turnover time $2H/U_f = 2$, and the fields are stored every $\Delta\tau \geq 2$ in order to collect samples that are likely uncorrelated. Moreover, the close correspondence between the terms of the consistency relation confirms that the averaging is performed over a long enough period of time to guarantee, at least, the statistical convergence of the second-order moments.

The main body of the thesis is organised as follows. The analyses of RBC

and RRBC in terms of flow topology, single-point and scale-by-scale budgets are presented in chapter 2 and 3 respectively. The focus of the work moves towards the modelling aspects of RBC in chapter 4, where a DNS data set is explicitly filtered and analyzed using filtered single-point and scale-by-scale budgets; the chapter concludes with the formulation of a novel and physics-based LES model for RBC, which is tested *a priori*. The main findings of the work are finally collected in chapter 5 together with some concluding remarks.

Here, it should be pointed out that some of the results presented in this thesis have been already published, whereas others have been accepted for publication. In particular, the material of chapter 2 has been reported in one journal papers ([L4]), three conference proceedings ([L2, L5, L7]) and an extended conference abstract ([L3]), while the results of chapter 4 have been published in an extended conference abstract ([L1]) and accepted for the publication in a conference proceeding [L6].

Chapter 2

Analysis of Rayleigh-Bénard convection

A novel theoretical framework for the analysis of turbulent Rayleigh-Bénard convection (RBC) in a combined physical/scale space domain is presented and discussed in this chapter. Section 2.1 is devoted to a preliminary description of the self-sustained cycle of turbulence in terms of the coherent structures that populate RBC. The flow dynamics is then analyzed in more detail in section 2.2, where the turbulent kinetic energy and temperature variance budgets are employed to statistically assess the fundamental processes involved in the aforementioned cycle. A description of turbulent RBC in both physical and scale space is finally presented in section 2.3 to complete the classical single-point analysis. The budgets employed for this purpose, namely the evolution equations for the second-order velocity and temperature structure functions, represent a generalization of the classic Kolmogorov and Yaglom equations to inhomogeneous, anisotropic flows and allow for a neat description of the turbulent processes occurring at different scales and locations in physical space. The scale-by-scale analysis seems able to capture the complex dynamics of thermally driven turbulence and, in particular, the dynamical role of the coherent structures. These results may have a strong impact on the theoretical understanding of the phenomenon and, from a practical point of view, on the modelling approaches in Large-Eddy Simulations (LES), as discussed later in chapter 4.

2.1 Flow topology

One interesting feature of turbulent RBC is the capability to organise itself in a complex but coherent fashion despite the chaotic environment. A non-stationary pattern of well-defined structures emerges from the turbulent background and forms the persistent machinery described by Kadanoff [43] that sustains the velocity and the temperature fluctuations. The above-mentioned structures are generally referred to as thermal plumes and, although several criteria have been proposed for the

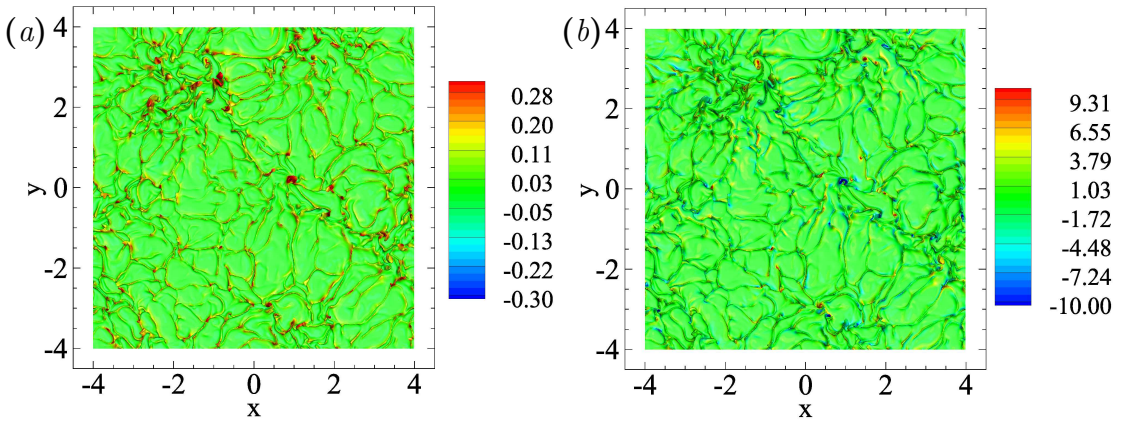

Figure 2.1: Top view of the isosurface of temperature $\theta^\star = 0.25$ (the temperatures of the lower and upper plates are, in order, 0.5 and -0.5) coloured by (a) the vertical velocity $w^\star$ and by the (b) vertical vorticity $\omega^\star$, obtained from DNS 3 ($Ra = 1.0 \times 10^7$).

identification, they can be loosely defined as portions of fluid having a temperature difference with the background [18]. Such structures are responsible for about half of the heat transport across the convection cell at moderate Rayleigh numbers ($10^6 \lesssim Ra \lesssim 10^8$ [67]), thus it would not be surprising to find several studies conducted on this subject [19, 102, 84]. At the lowest Rayleigh number considered in this study, $Ra = 1.7 \times 10^5$, the thermal plumes are found to be large, smooth and they tend to span the entire height of the cell. Moreover, ascending and descending structures lock into large-scale circulations, also referred in literature to as rolls or mean winds, which drift along the horizontal directions and persist for quite a long time [92]. As Ra increases, the average size of the plumes decreases and, qualitatively, the structures become less coherent, less distinguishable from the turbulent background but still organised into rolls.

Figure 2.1(a,d) shows a hot isosurface of temperature coloured, in order, by the vertical velocity $w^\star$ and the vertical vorticity $\omega^\star = \partial v^\star/\partial x - \partial u^\star/\partial y$ obtained from the DNS at $Ra = 1.0 \times 10^7$. Close to the horizontal walls, the thermal boundary layer protrudes creating the complex network of sheet-like roots that is clearly visible in the pictures. The crests are found to move in time along the plate, conveying fluid from different directions into the intersection points between two or more of them. In these spots, the concentration of momentum and the thermal boundary layer instability favour the ejection of fluid that presents an equally probable positive or negative vertical vorticity depending on the relative motion of the sheet-like roots [102]. Once emitted, the thermal plumes accelerate throughout the core of the flow under the action of buoyancy forces and enlarge via turbulent mixing and diffusion, assuming a characteristic mushroom-like shape; see the vertical section coloured by the temperature represented in figure 2.2.

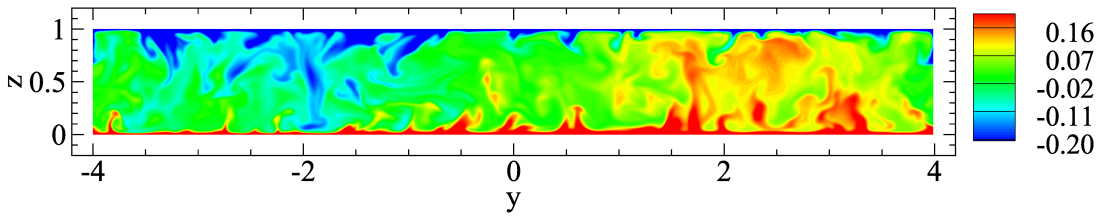

Figure 2.2: Vertical section at $x = -2$ coloured by the temperature $\theta^\star$, obtained from DNS 3 ($Ra = 1.0 \times 10^7$).

In turbulent RBC, the plumes with similar temperatures tend to be ejected near to each other, to group in the core of the flow and to impinge together on the opposite wall, where they mechanically extract new sheet-like roots from the thermal boundary layer and close their life cycle [67]. The clusterization phenomenon is quite visible in figure 2.1(a,d), as the ejection spots are concentrated around some specific points, e.g. $(x, y) = (-2, 2)$, and the emitted plumes roll around on each other creating a large ascending jet of warm fluid. Moreover, the vertical slice in figure 2.2 clearly shows a warm and a cold agglomerate of thermal plumes around $y = 2$ and $y = -2$ respectively. The impingement of the clusters onto the horizontal plates favour the extraction of sheet-like roots from the thermal boundary layer and sweep them close to each others, establishing a positive feedback that reinforces the large-scale circulation. The continuous displacement in space and the occasional reversal of the rolls guarantee the average velocity field to become negligible if the statistic is computed over a sufficiently long period [92, 7, 100].

The near-wall region represents both the departure and the arrival points of the thermal plumes and the way in which the coherent structures react back on the boundary layers has a key role in the self-sustained cycle of turbulence. Figure 2.3(a) shows the same isosurface as depicted in figure 2.1(a,d) coloured with the horizontal divergence of the velocity field, $div_\pi = \partial u^\star/\partial x + \partial v^\star/\partial y$. Two well-defined events can be identified in terms of the horizontal divergence, namely the impingement ($div_\pi > 0$) and the ejection of thermal plumes ($div_\pi < 0$). Adjacent regions of positive divergence are separated by crests of fluid having a negative divergence, thus the impinging plumes seem to interact with the thermal boundary layer by extracting new sheet-like roots; the life cycle of the coherent structure is closed in this way and new-born plumes eject from the near-wall region, sustaining the velocity and the temperature fluctuations.

Let us support the qualitative analysis of the flow topology presented up to now with some statistical results. In order to facilitate the comparison between the data sets at different Rayleigh numbers, namely DNS 1, DNS 2 and DNS 3, the statistical observables are hereafter expressed as a function of spatial variables that are non-dimensionalized with respect to H/Nu instead of H and denoted with the superscript $*$. In RBC, H/Nu is equal to two-times the thermal boundary layer

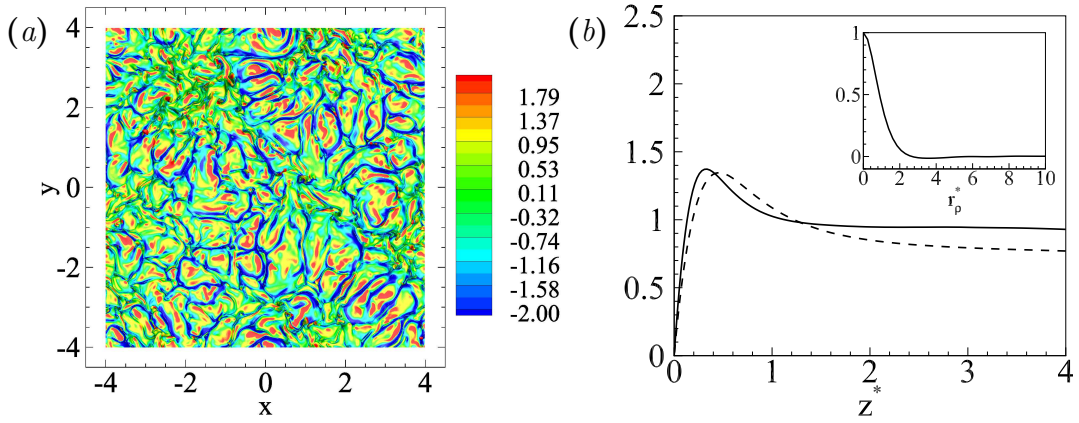

Figure 2.3: (a) Top view of the isosurface of temperature $\theta^\star = 0.25$ coloured by the planar divergence of the velocity field div_π. (b) Main plot: conditional statistics $\langle div_\pi \rangle_+$ (solid line) and $-\langle div_\pi \rangle_-$ (dashed line) as a function of z^*. Inset: autocorrelation function R as a function of r^*_ρ, evaluated at $z^* = 0.3$. The results come from DNS 3 ($Ra = 1.0 \times 10^7$).

thickness δ^{sl}_θ based on the slope of the mean temperature profile at the wall, i.e. $\delta^{sl}_\theta = (2d\Theta/dz|_{z=0})^{-1}$; therefore, it arguably represents a dominant length scale in the flow. In support of this claim we will see in §2.2 and §2.3 that, if the independent variables are non-dimensionalized with respect to H/Nu, the profile shape of the temperature statistics keeps almost unchanged for the different Rayleigh numbers considered in this study, whereas some velocity statistics exhibit just a small drift in the profile shape.

The average magnitude of the impingement and the ejection events can be quantified from the conditional statistics $\langle div_\pi \rangle_+$ and $-\langle div_\pi \rangle_-$ respectively, where $\langle div_\pi \rangle_+ = \langle div_\pi \rangle$ for $div_\pi > 0$ and $\langle div_\pi \rangle_- = \langle div_\pi \rangle$ for $div_\pi < 0$. As can be seen in the main plot of figure 2.3(b), representing $\langle div_\pi \rangle_+$ and $-\langle div_\pi \rangle_-$ as a function of z^* and for $Ra = 1.0 \times 10^7$, the impingement reaches its maximum at $z^* \approx 0.3$, while the ejection is peaked slightly further away at $z^* \approx 0.5$, in agreement with the instantaneous kinematics depicted in figure 2.3(a). We can estimate the characteristic size of the impinging plume by considering the autocorrelation function of the horizontal divergence $R = \langle div_\pi(\boldsymbol{\rho}, z) div_\pi(\boldsymbol{\rho} + \boldsymbol{r_\rho}, z) \rangle \,/\, \langle div^2_\pi(\boldsymbol{\rho}, z) \rangle$ where $\boldsymbol{\rho} = (x, y)$ and $\boldsymbol{r_\rho} = (r_x, r_y)$ are, in order, the position vector and the separation vector in the horizontal planes. By accounting for the statistical homogeneity and isotropy in the xy planes, the functional dependence of R on $(\boldsymbol{\rho}, \boldsymbol{r_\rho}, z)$ reduces to (r_ρ, z), where $r_\rho = \sqrt{r_x^2 + r_y^2}$. The uncorrelation length at $z^* = 0.3$ is around 3 (see the inset in figure 2.3b) and it does not change for the different Rayleigh numbers considered in this study. This separation can be considered a measure of the average diameter of impinging plumes, as the intensity of impingement reaches its maximum and exceeds the ejection at $z^* = 0.3$; see the main plot in figure 2.3(b). As the uncorrelation

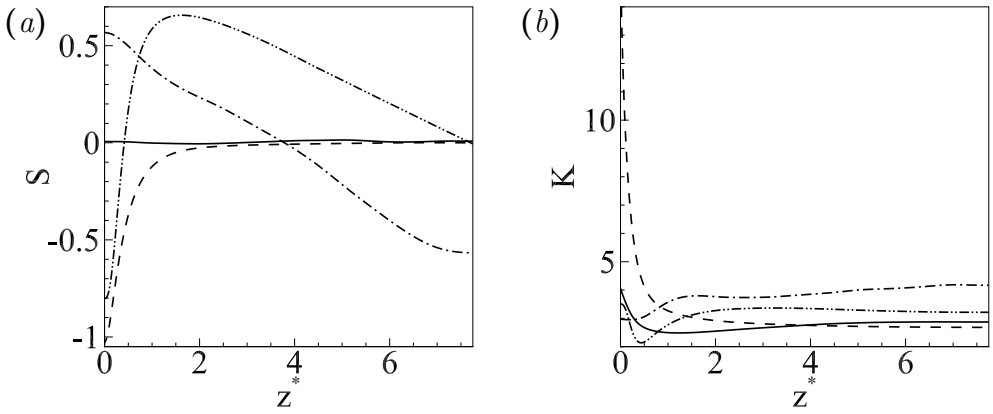

Figure 2.4: (a) Skewness and (b) kurtosis of $u^\star$ (solid line), $w^\star$ (dashed line), $p^\star$ (dot-dashed line) and $\theta^\star$ (dot-dot-dashed line) as a function of z^*.

length does not change with Ra, it can be deduced that the characteristic diameter scales with the thermal boundary layer thickness.

The flow topology can be studied in some more detail by analyzing the skewness and the kurtosis of $u^\star$, $w^\star$, $\theta^\star$ and $p^\star$, where the probability density functions (p.d.f.s) of $u^\star$ and $v^\star$ are equal for statistical isotropy. Figure 2.4(a,b) shows the skewness S and the kurtosis K of the flow variables as a function of z^* and for $Ra = 1.0 \times 10^7$. Only the bottom half of the cell is represented for symmetry reasons; in particular, the vertical velocity and temperature skewnesses, $S_{w^\star}$ and $S_{\theta^\star}$, are antisymmetric with respect to the centerline, whereas all the other statistics are symmetric. Both the velocity components and the temperature are distributed almost normally at the center of the cell, $z^* = 7.75$, as the skewness and the kurtosis are close to the correspondent moments for the normal distribution, $S_N = 0$ and $K_N = 3$. The skewness of $u^\star$ remains equal to zero throughout the cell for statistical isotropy, whereas its kurtosis increases as the wall is approached, although it does not drift excessively from the Gaussian value. By contrast, the probability density functions of the vertical velocity and temperature dramatically diverge from the normal distribution. Next to the lower wall, the p.d.f. of $w^\star$ is considerably skewed towards negative fluctuations and the kurtosis monotonically increases as the wall is approached. A possible interpretation of the vertical velocity skewness and kurtosis regards the spatial distribution of upward and downward motions in the wall-parallel planes [51]. In case the area occupied by patches of ascending fluid is larger than that occupied by descending ones, the average upward velocity has to be smaller than the average downward velocity due to incompressibility, hence $S_{w^\star}$ tends to be negative. In a similar way, a large positive skewness indicates upward events occurring in small circumscribed areas. The kurtosis measures the level of intermittency of the variable, thus high values of the vertical velocity kurtosis $K_{w^\star}$ indicate that extreme fluid displacements in vertical direction occur frequently. Ac-

cording to the results depicted in figure 2.4(a,b), downward fluid motions become even more localized and frequent as the lower wall is approached, meaning that only few intense plumes ejected from the opposite plate can pass through the layer and impinge.

The temperature skewness $S_{\theta^\star}$ changes sign near the horizontal plates and the kurtosis $K_{\theta^\star}$ reaches a minimum around the same locations. Two distinct regions can be identified based on the profile of $S_\theta^\star$ plotted in figure 2.4(a,b): one in the near-wall region ($z^* \lesssim 0.5$) and the other inside the core of the flow ($z^* \gtrsim 0.5$). The product between $S_{w^\star}$ and $S_{\theta^\star}$ is found to be non-negative for $z^* \lesssim 0.5$, supporting the observation that plume impingement represents the most extreme event occurring in this layer. As we move out from the near-wall region, the product $S_{w^\star}S_{\theta^\star}$ changes sign and $S_{w^\star}$ gradually decreases its slope. This behaviour can be reasonably explained by considering that plume impingement in not the only intermittent phenomenon leaving a statistical footprint sufficiently away from the wall, indeed also the protrusion of sheet-like roots and the emission of mushroom-like plumes should be important. At the centreline, all p.d.f.s, except for the pressure one, become even less skewed as the intermittent events related to the ascending plumes balance the events related to the descending ones. All p.d.f.s except the pressure one become even less skewed as the centerline is approached because the intermittent events associated with upward motions balance the events associated with downward motions.

Inside the core of the flow, the pressure is skewed towards negative values and the kurtosis reaches a maximum, meaning that negative and extreme pressure fluctuations are most likely to occur in this region. This observation can be attributed to hot and cold plumes that accelerate throughout the bulk under the action of buoyancy forces, thus negative pressure fluctuations are somehow expected. Close to the wall, the pressure skewness is positive and the kurtosis is minimum, denoting the sporadic occurrence of intense positive fluctuations caused by the deceleration of the impinging plumes [99].

2.2 Single-point analysis

A characteristic feature of RBC and wall-bounded flows in general is the presence of a self-sustained cycle throughout which turbulent fluctuations are generated by mechanisms embedded in the flow, are transported in space and are dissipated by diffusion [66]. Some of these processes can be described in terms of the different interactions between the coherent structures; as an example, the ascending and descending plumes in RBC are responsible for the productions and the transport of velocity fluctuations, whereas the impingement events generate the viscous boundary layers where most of the dissipation occurs. Such a mechanistic description of the self-sustained cycle of turbulence is useful to provide us a qualitative outlook of the flow dynamics, however, a quantitative evaluation of the phenomenon requires

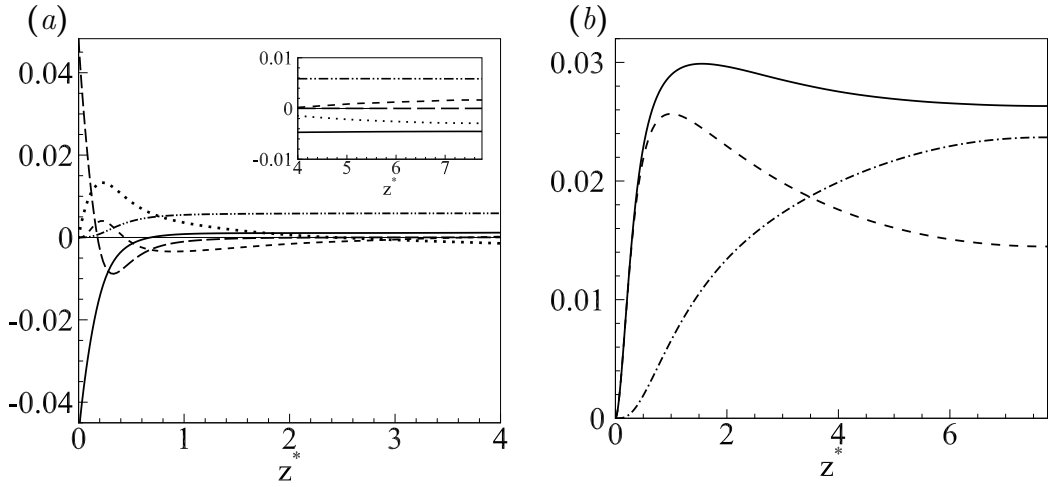

Figure 2.5: (a) Terms of the turbulent kinetic energy budget (2.1) as a function of z^* for $Ra = 1.0 \times 10^7$: inertial transport (dashed line), pressure transport (dotted line), viscous transport (long dashed line), production (dot-dot-dashed line) and dissipation (solid line). The details of the bulk are shown in the inset. (b) Profiles of $\langle k \rangle$ (solid line), $\langle u^2 \rangle$ (dashed line) and $\langle w^2 \rangle$ (dot-dashed line) as a function of z^*.

rather a different approach.

In this section, the turbulent kinetic energy and temperature variance budgets are analyzed aiming at a statistical description of the RBC dynamics. Based on these equations, some distinct regions where turbulent fluctuations are generated, transported and dissipated are identified within the domain and explained in terms of the flow topology. Let us begin by considering the budget of turbulent kinetic energy $\langle k \rangle = 0.5 \langle u_i u_i \rangle$, which reads as

$$-\frac{d\langle kw \rangle}{dz} - \frac{d\langle wp \rangle}{dz} + \sqrt{\frac{Pr}{Ra}} \frac{d^2 \langle k \rangle}{dz^2} + \langle w\theta \rangle - \langle \tilde{\epsilon} \rangle = 0, \tag{2.1}$$

where $\langle \tilde{\epsilon} \rangle$ is the average rate of pseudo-dissipation,

$$\langle \tilde{\epsilon} \rangle = \sqrt{\frac{Pr}{Ra}} \left\langle \frac{\partial u_i}{\partial x_j} \frac{\partial u_i}{\partial x_j} \right\rangle.$$

The first three terms in (2.1) are the inertial, pressure and viscous contributions to the overall transport of $\langle k \rangle$ along the vertical direction, whereas the last two terms, hereafter referred to as production and dissipation, are the source due to buoyancy and the sink due to viscosity respectively.

Figure 2.5(a) represents the different terms of the budgets as a function of z^* and for $Ra = 1.0 \times 10^7$. The domain can be separated into three well-defined sections: a bulk region localized in the core of the flow, a viscous layer beside the wall and a transitional layer between them. The bulk is defined as the region within which

velocity fluctuations are maintained by buoyant production rather than transport mechanisms and it extends from the centerline at $z^* = 7.75$ down to the crossover between production and pressure transport around $z^* = 0.8$. It is characterized by a net production of turbulent kinetic energy, $\langle w\theta \rangle - \langle \tilde{\epsilon} \rangle > 0$, which is transported away by means of inviscid processes to be dissipated inside the near-wall region, where $\langle w\theta \rangle - \langle \tilde{\epsilon} \rangle < 0$. While pressure mechanisms extract energy from an high bulk region located at $z^* \gtrsim 2.5$ ($-d \langle wp \rangle / dz < 0$) to mildly sustain the lower part of the bulk and mostly feed both transitional and viscous layers ($-d \langle wp \rangle / dz > 0$), the inertial processes transport energy from the low bulk at $0.8 \lesssim z^* \lesssim 2.5$ ($-d \langle kw \rangle / dz < 0$) towards the near-wall region and also towards the high bulk ($-d \langle kw \rangle / dz > 0$), thus acting in opposition to the pressure transport.

The transitional layer is the region where most of the energy is provided by pressure and inertial transports rather than production and it extends from $z^* \approx 0.8$ to the crossover between pressure and viscous transports, $z^* \approx 0.1$. Unlike in the bulk region, the rate of dissipation overcomes the production in the transitional layer, $\langle w\theta \rangle - \langle \tilde{\epsilon} \rangle < 0$, and the resulting energy deficit is mainly balanced by a positive pressure transport, which means that the extra energy produced in the bulk is mostly released to this layer through pressure-velocity correlations. The transitional layer, in turn, diffuses energy into the viscous layer at $z^* \lesssim 0.1$ where it is completely dissipated ($\sqrt{Pr/Ra}\, d^2 \langle k \rangle / dz^2 \approx \langle \tilde{\epsilon} \rangle$).

A further insight into the RBC dynamics can be obtained by splitting the budget (2.1) into the sum of three equations, one for each component of the turbulent kinetic energy, $\langle u^2 \rangle$, $\langle v^2 \rangle$ and $\langle w^2 \rangle$. The resulting equation set can be written as

$$-\frac{1}{2}\frac{d\langle u^2 w\rangle}{dz} + \left\langle p\frac{\partial u}{\partial x}\right\rangle + \frac{1}{2}\sqrt{\frac{Pr}{Ra}}\frac{d^2\langle u^2\rangle}{dz^2} - \langle \tilde{\epsilon}_x \rangle = 0, \tag{2.2a}$$

$$-\frac{1}{2}\frac{d\langle v^2 w\rangle}{dz} + \left\langle p\frac{\partial v}{\partial y}\right\rangle + \frac{1}{2}\sqrt{\frac{Pr}{Ra}}\frac{d^2\langle v^2\rangle}{dz^2} - \langle \tilde{\epsilon}_y \rangle = 0, \tag{2.2b}$$

$$-\frac{1}{2}\frac{d\langle w^3\rangle}{dz} + \left\langle p\frac{\partial w}{\partial z}\right\rangle - \frac{d\langle wp\rangle}{dz} + \frac{1}{2}\sqrt{\frac{Pr}{Ra}}\frac{d^2\langle w^2\rangle}{dz^2} + \langle w\theta \rangle - \langle \tilde{\epsilon}_z \rangle = 0, \tag{2.2c}$$

where $\langle \tilde{\epsilon}_x \rangle$, $\langle \tilde{\epsilon}_y \rangle$, $\langle \tilde{\epsilon}_z \rangle$ are the three components of the average rate of pseudo-dissipation, i.e.

$$\langle \tilde{\epsilon}_x \rangle = \sqrt{\frac{Pr}{Ra}} \left\langle \frac{\partial u}{\partial x_j}\frac{\partial u}{\partial x_j} \right\rangle, \langle \tilde{\epsilon}_y \rangle = \sqrt{\frac{Pr}{Ra}} \left\langle \frac{\partial v}{\partial x_j}\frac{\partial v}{\partial x_j} \right\rangle \quad \text{and} \quad \langle \tilde{\epsilon}_z \rangle = \sqrt{\frac{Pr}{Ra}} \left\langle \frac{\partial w}{\partial x_j}\frac{\partial w}{\partial x_j} \right\rangle.$$

It can be verified that the sum of equations (2.2)(a-c) corresponds to (2.1) since the sum of the pressure-strain rate terms $\langle p\partial u_i/\partial x_i \rangle$ is zero for the incompressibility constraint imposed by (1.1)(a). The buoyant production $\langle w\theta \rangle$ affects only the budget of $\langle w^2 \rangle$, thus energy enters the system through the vertical velocity components and it is redistributed to the horizontal ones by means of the pressure-stain

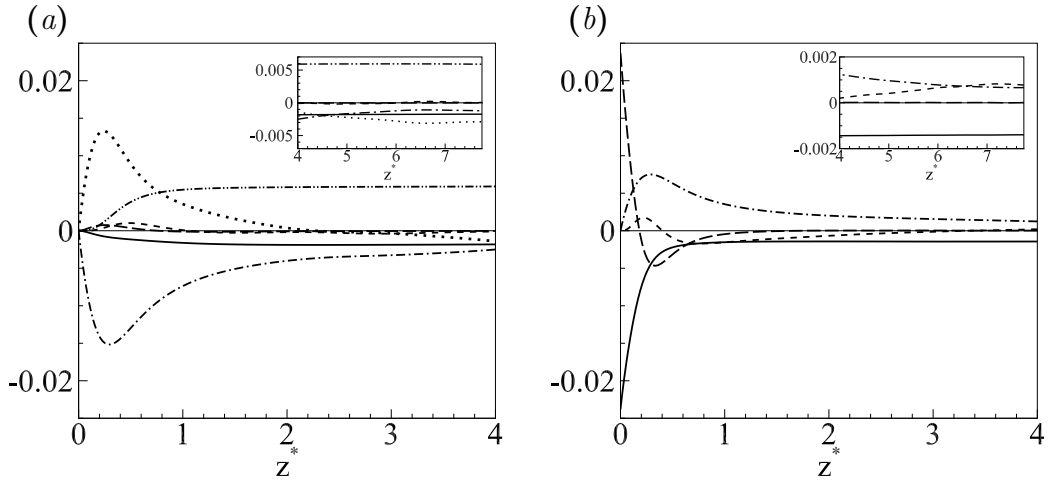

Figure 2.6: (a) Budget of $\langle w^2 \rangle$ and (b) budget of $\langle u^2 \rangle$ as a function of z^*: inertial transport (dashed line), pressure-strain rate term (dot-dashed line), pressure transport (dotted line), viscous transport (long dashed line), production (dot-dot-dashed line) and dissipation (solid line). The details of the bulk are shown in the insets.

rate correlations. Analysing in more detail the terms of equation (2.2)(c) represented in figure 2.6(a), it emerges that the vertical dissipation $\langle \tilde{\epsilon}_z \rangle$ can be neglected with respect to the production almost at every wall-distance. Moreover, the surplus of energy which is generated inside the bulk, namely $\langle w\theta \rangle - \langle \tilde{\epsilon}_z \rangle + \langle p\partial w/\partial z \rangle > 0$, is transported towards the wall essentially by pressure mechanisms, as both viscous and inertial transports are substantially negligible. Inside the transitional layer, the buoyant production decreases, whereas the positive pressure transport increases; hence, the wall-normal fluctuations are sustained by the energy generated inside the bulk and transported here by means of pressure-velocity correlations. The pressure-strain rate term, which is negative and reaches its maximum intensity in the transitional layer, is the main sink of $\langle w^2 \rangle$ since the vertical dissipation is very small even close to the wall.

The budget of $\langle u^2 \rangle$ is equal to the budget of $\langle v^2 \rangle$ for statistical isotropy, thus it is the only one reported here; see figure 2.6(b). In this case, the pressure-strain rate term acts as a source at every wall-distance and reaches a maximum inside the transitional layer, denoting an intense exchange of energy between the vertical and the horizontal velocity components. The resulting energy excess, $\langle p\partial u/\partial x \rangle - \langle \tilde{\epsilon}_x \rangle > 0$, is transported towards the bulk and towards the viscous layer via inertial and viscous processes respectively to be finally dissipated.

In summary, buoyancy force produces vertical kinetic energy $\langle w^2 \rangle$ throughout the bulk of the flow and it reasonably determines the peak of $\langle w^2 \rangle$ observed at the centerline; see figure 2.5(b). Due to the lack of vertical dissipation, the vertical kinetic energy generated in the core is almost entirely transported towards the wall by means of pressure mechanisms and it is dramatically released to the horizontal

components $\langle u^2 \rangle$ and $\langle v^2 \rangle$ via the pressure-strain rate terms, which are unsurprisingly peaked in correspondence of the maximum $\langle u^2 \rangle$. In the end, the horizontal kinetic energy is redistributed along the wall-normal direction z^* by viscous and inertial mechanisms to balance the local dissipation rates. It should be observed that the vertical kinetic energy is almost totally released to the wall-parallel components within the transitional layer. Indeed, the viscous layer is almost a two-dimensional region, as $\langle u^2 \rangle$ and $\langle v^2 \rangle$ are much smaller than $\langle w^2 \rangle$.

The fluid motion in turbulent RBC is sustained by the buoyancy force induced by the temperature, which is therefore an active scalar. Evidently the analysis of the turbulent kinetic energy equation alone is insufficient to understand how the self-sustained cycle of turbulence works in our flow; indeed, a thorough investigation requires also the analysis of the equation for the temperature variance $\langle \theta^2 \rangle$, namely

$$-\frac{d\langle \theta^2 w \rangle}{dz} + \frac{1}{\sqrt{PrRa}} \frac{d^2 \langle \theta^2 \rangle}{dz^2} - 2\langle w\theta \rangle \frac{d\Theta}{dz} - \langle \chi \rangle = 0, \tag{2.3}$$

where Θ is the average temperature and $\langle \chi \rangle$ is the average dissipation rate of temperature variance,

$$\langle \chi \rangle = \frac{2}{\sqrt{PrRa}} \left\langle \frac{\partial \theta}{\partial x_i} \frac{\partial \theta}{\partial x_i} \right\rangle.$$

The first two terms in (2.3) are the inertial and the diffusive contributions to the overall transport of $\langle \theta^2 \rangle$ along the vertical direction, whereas the last two terms, hereafter referred simply as production and dissipation, are a source and a sink of temperature variance respectively. In figure 2.7(a), the terms of (2.3) are plotted as functions of z^* and for $Ra = 1.0 \times 10^7$. Three well-defined regions can be identified according to the budget: a thermal bulk inside the core of the flow, a diffusive layer beside the wall and a thermal transitional layer between them. The thermal transitional layer is defined as the region where the temperature fluctuations are sustained by production rather than transport processes and it extends from the crossover between the production and the inertial transport around $z^* = 2.4$ down to the crossover between the production and the diffusive transport at $z^* \approx 0.16$. The production exceeds the dissipation inside this layer and the net amount of temperature variance generated per unit time, $-2\langle w\theta \rangle d\Theta/dz - \langle \chi \rangle > 0$, is carried towards the wall and towards the core to be dissipated, as $-2\langle w\theta \rangle d\Theta/dz - \langle \chi \rangle < 0$ in those regions. The thermal diffusivity transports temperature variance principally in the direction of the wall, while inertia carries out the transport in the direction of the core. Inside the thermal bulk region, which extends from the outer edge of the thermal transitional layer at $z^* \approx 2.4$ up to the centerline, the production is negligible and the fluctuations are sustained by the inertial transport and dissipated by diffusivity. On the other hand, temperature variance is transported into the diffusive layer ($z^* \lesssim 0.16$) essentially by diffusive mechanisms to balance the local dissipation rate.

Figure 2.8(a,b) reports the production and the transport terms of the turbulent kinetic energy and the temperature variance budget for $Ra = 1.7 \times 10^5$, $Ra =$

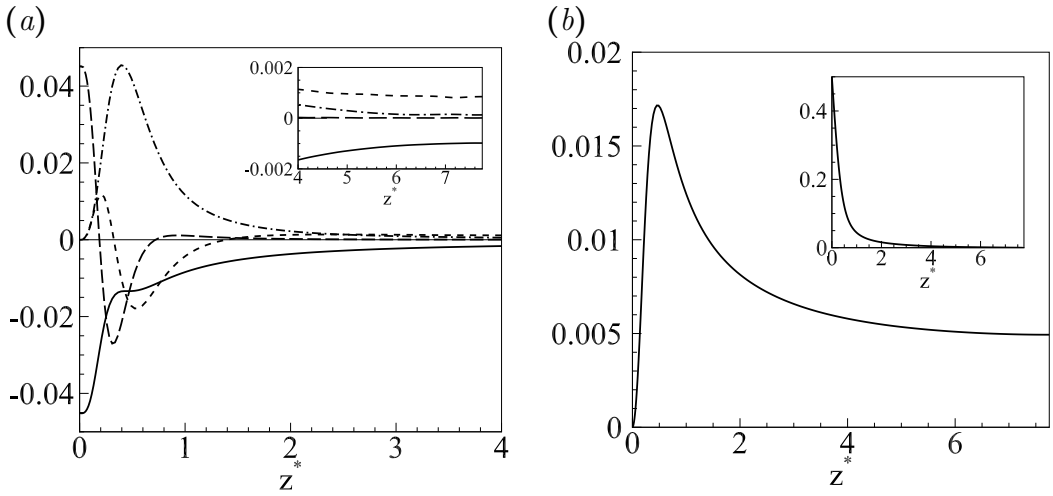

Figure 2.7: (a) Terms of the temperature variance budget (2.3) as a function of z^* for $Ra = 1.0 \times 10^7$: inertial transport (dashed line), diffusive transport (long dashed line), production (dot-dashed line) and dissipation (solid line). The details of the thermal bulk region are shown in the inset. (b) Profile of (main panel) $\langle \theta^2 \rangle$ and (inset) Θ as a function of z^*.

1.0×10^6 and $Ra = 1.0 \times 10^7$; see DNS 1, DNS 2 and DNS 3 in table 1.1. The different regions identified so far at the highest Ra can be also recognized at lower Ra, meaning that the fundamental features of the RBC dynamics remain substantially unaltered with respect to the Rayleigh number, at least in the range of parameters considered in this work. As anticipated in section 2.1, the choice of normalizing the independent variables with the length scale H/Nu allows for a more appropriate comparison of the results when different Ra are considered. Indeed, the shapes of the profiles plotted in figure 2.8(a,b) are roughly independent from the Rayleigh number, e.g. the location of the extrema is roughly the same for the different Ra. On the other hand, the intensity of the different processes occurring in the flow are clearly modulated by the Rayleigh number. The terms of the temperature variance budget increase in magnitude with Ra, while the terms of the turbulent kinetic energy budget decrease. The latter behaviour contrasts sharply with the fact that by increasing the Rayleigh number the turbulence intensity of the system increases and it is related to the adoption of the free-fall velocity U_f as the characteristic velocity. By employing other velocity scales, such as κ/H, the observed trend would be reversed, with the terms of equation (2.1) increasing their intensity with Ra.

The mechanistic description of the self-sustained cycle of turbulence stemming from the flow topology can readily be matched with the rigorous statistical analysis in terms of energetics. During their life span, thermal plumes are ejected from the plates, they accelerate under the action of buoyancy forces and finally impact on the opposite wall. The impermeability condition at the boundaries forces the impinging structures to spread along the horizontal direction ($div_\pi > 0$) with the consequent

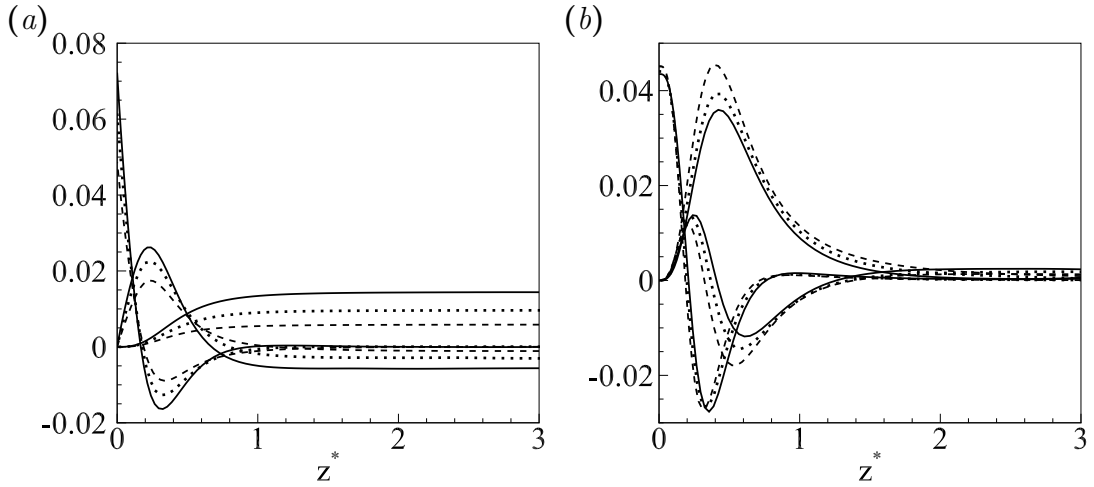

Figure 2.8: (a) Profiles of production, viscous transport and sum of pressure and inertial transport of turbulent kinetic energy as a function of z^*, for $Ra = 1.7 \times 10^5$ (solid line), $Ra = 1.0{\times}10^6$ (dotted line) and $Ra = 1.0{\times}10^6$ (dashed line). (b) Profiles of production, inertial transport and diffusive transport of temperature variance as functions of z^* for the same Rayleigh numbers.

convergence of near-wall fluid into crests ($div_\pi < 0$) and the ejection of newborn plumes from the intersection spots between different sheet-like roots. In addition to this qualitative picture, the analysis of the budgets allows us to produce a more detailed portrait of the flow. The turbulent kinetic energy of thermal plumes is generated by buoyancy throughout the bulk region ($\langle w\theta \rangle - \langle \tilde{\epsilon} \rangle > 0$), is carried away by pressure-velocity correlations and swept into the transitional layer ($\langle w\theta \rangle - \langle \tilde{\epsilon} \rangle < 0$); see figure 2.5($a$). Here, the turbulent kinetic energy is gradually transferred from the wall-normal towards the horizontal velocity components by pressure-strain rate correlations, as can be seen in figure 2.6(a,b). The energy transfer between the velocity components can be arguably related to the enlargement of thermal plumes following the impingement event. Indeed, the impinging cap of the structure induces a positive divergence of the horizontal velocity field since vertical momentum is redirected to the horizontal one.

According to this scenario, the maximum of $\langle div_\pi \rangle_+$ is located exactly at the same wall-distance as the maximum of the pressure-strain rate terms; see figure 2.3(b) and figure 2.6(a,b). Hence, the inter-component exchange of turbulent kinetic energy is a clear statistical footprint of the impingement events. Viscous mechanisms transport part of the horizontal components $\langle u^2 \rangle$ and $\langle v^2 \rangle$ into the viscous layer to be dissipated; see figure 2.6(b). The remaining energy flows from the horizontal components towards the vertical one, resulting in the network of sheet-like roots. From the perspective of the temperature field, the interaction between the average temperature gradient in the transitional layer and the mechanically extracted sheet-like roots induces temperature fluctuations that are sufficiently intense to trigger an

ejection event. As can be observed by comparing figure 2.3(b) with figure 2.7(b), the production of temperature variance is maximum where $\langle div_\pi \rangle\_$ is also peaked; hence, we can argue that the protrusion of sheet-like roots is responsible for the sustainment of temperature fluctuations (see figure 2.7b), which in turn triggers the detachment of new plumes and closes the self-sustained cycle of turbulence in RBC.

2.3 Scale-by-scale analysis

The self-sustained cycle of turbulence in RBC, analyzed so far in terms of flow topology (see § 2.1) and single-point equations (see § 2.2), is here extended to a multi-scale framework. Indeed, the processes responsible for production, transport and dissipation of velocity and temperature fluctuations highlighted so far are inherently multi-scale, since they depend not only on the geometrical location within the flow but also on the length scale considered. In light of this scenario, a compound description in the physical/scale space is required for the complete understanding of the flow dynamics and for the turbulence modelling (see chapter 4). Two budgets are employed for this purpose, namely the evolution equations for the second-order velocity and temperature structure functions. These balances represent a generalization of the classic Kolmogorov and Yaglom equations, originally derived for homogeneous and isotropic turbulence [48, 101], to inhomogeneous and anisotropic flows, allowing for a neat description of the processes occurring at different scales and locations in physical space. The budgets of the second-order structure functions are presented in section 2.3.1 first for homogeneous turbulence and then for the RBC, aiming at gradually disclosing the main features of the scale-by-scale analysis. A thorough investigation of RBC in terms of the Kolmogorov and Yaglom equations is then covered in § 2.3.2 and § 2.3.3 together with some remarks on the enhanced description of the flow. The various regions of the combined scale/physical space where the relevant physical processes take place are then identified in section 2.3.4 to summarize the complex scenario emerging from the multi-scale analysis.

2.3.1 The Kolmogorov and Yaglom equations

In case of homogeneous and isotropic turbulence transporting a passive scalar (hereafter temperature, for the sake of clarity), the classical Kolmogorov-Obukhov-Corrsin (K41-OC) theory states that a range of scales develops at sufficiently high Reynolds numbers where turbulent fluctuations are only transferred from large to small scales [49, 65, 26]. This non-trivial result stems from the exact equations for the second-order velocity and temperature structure functions, in order $\langle \delta u^2 \rangle = \langle \delta u_i \delta u_i \rangle$ and $\langle \delta \theta^2 \rangle = \langle \delta \theta \delta \theta \rangle$, where $\delta u_i = u_i(x_j + r_j/2, t) - u_i(x_j - r_j/2, t)$ and $\delta\theta = \theta(x_j + r_j/2, t) - \theta(x_j - r_j/2, t)$ are the increments of velocity and temperature fluctuations at time t between the points $x_j - r_j/2$ and $x_j + r_j/2$.

According to the heuristic interpretation given by Davidson *et al.* [29], the

second-order velocity and temperature structure functions indicate, in order, the turbulent kinetic energy and the temperature variance of eddies having sizes smaller than $r = \sqrt{r_i r_i}$. Indeed, turbulent lengths scales below r modulate velocity and temperature signals either at $x_j + r_j/2$ or $x_j - r_j/2$, but not at both points simultaneously; therefore, they actively contribute to the fluctuating increments δu_i and $\delta\theta$. Eddies of size larger than r, on the other hand, induce similar signals at both locations and so they contribute very little to these increments. That said, the increment between two points separated by a distance r can be considered equivalent to a filtering operation that suppresses the contribution from scales larger than r and retains the contribution from eddies having size smaller than r. In view of this qualitative observation, we refer hereafter to $\langle \delta u^2 \rangle$ and $\langle \delta\theta^2 \rangle$ as *scale energy* and *scale variance*, in agreement with the nomenclature introduced by Danaila *et al.* [28] and employed later in many different works [59, 20, 24].

Generally speaking, the second-order structure function depends on seven independent variables, namely the three coordinates of the mid-point x_j, the three components of the separation vector r_j and the time t. The presence of statistical symmetries in the flow reduces the degrees of freedom and, in case of homogeneous and non-decaying turbulence, $\langle \delta u^2 \rangle$ and $\langle \delta\theta^2 \rangle$ do not depend on x_j and t. The balances for the second-order structure functions in homogeneous and non-decaying turbulence transporting a passive temperature can be derived exactly from the governing equations and read as follows

$$-\frac{\partial \langle \delta u^2 \delta u_i \rangle}{\partial r_i} + 2\langle \delta f_i^u \delta u_i \rangle + 2\sqrt{\frac{Pr}{Ra}}\frac{\partial^2 \langle \delta u^2 \rangle}{\partial r_j \partial r_j} - 4\langle \epsilon \rangle = 0, \tag{2.4}$$

$$-\frac{\partial \langle \delta\theta^2 \delta u_i \rangle}{\partial r_i} + 2\left\langle \delta f_i^\theta \delta u_i \right\rangle + \frac{2}{\sqrt{PrRa}}\frac{\partial^2 \langle \delta\theta^2 \rangle}{\partial r_j \partial r_j} - 2\langle \chi \rangle = 0, \tag{2.5}$$

where $2\langle \delta f_i^u \delta u_i \rangle$ and $2\left\langle \delta f_i^\theta \delta u_i \right\rangle$ are the production terms due to the homogeneous, external forcing f_i^u and f_i^θ acting at the largest scale of the flow.

The cascade terms, namely the first ones in both (2.4) and (2.5), denote the amounts of turbulent kinetic energy and temperature variance that are transferred, per unit time, from (to) scales larger than r to (from) scales smaller than r via inertial mechanisms, while the sums of the last two terms in the budgets denote the rate at which turbulent kinetic energy and temperature variance are dissipated by eddies of size less than r through viscous and diffusive processes. Finally, the third terms can be interpreted individually as the dissipation rates attributable to scales larger than r; hence, they become negligible for sufficiently large separations as the dissipative action of viscosity is more effective at small scales.

An inertial range is generally assumed to develop for $\eta_k, \eta_b \ll r \ll \ell_0$ in case of high-turbulent flows, where the Kolmogorov scale η_k and the Batchelor scale η_b are the smallest scale of motion and temperature respectively, and ℓ_0 is the integral scale. Both production and viscous/diffusive mechanisms can be neglected inside

the inertial range; therefore, (2.4) and (2.5) simplify to

$$-\frac{\partial \langle \delta u^2 \delta u_i \rangle}{\partial r_i} = 4 \langle \epsilon \rangle , \tag{2.6}$$

$$-\frac{\partial \langle \delta \theta^2 \delta u_i \rangle}{\partial r_i} = 2 \langle \chi \rangle , \tag{2.7}$$

which state that the amounts of turbulent kinetic energy and temperature variance transferred, per unit time, from scales larger than r to scales smaller than r in a direct cascade process, i.e. $-\partial \langle \delta u^2 \delta u_i \rangle / \partial r_i > 0$ and $-\partial \langle \delta \theta^2 \delta u_i \rangle / \partial r_i > 0$, are balanced by the corresponding average dissipation rates. If turbulence is also statistically isotropic, then (2.6) and (2.7) further reduce to the Kolmogorov's four-fifths law,

$$-\left\langle {\delta u_\parallel}^3 \right\rangle = \frac{4}{5} \langle \epsilon \rangle \, r, \tag{2.8}$$

and to its scalar analogue, the two-thirds law,

$$-\left\langle \delta \theta^2 \delta u_\parallel \right\rangle = \frac{2}{3} \langle \chi \rangle \, r, \tag{2.9}$$

where the longitudinal velocity increment $\delta u_\parallel$ is the component of δu_i parallel to r_i. The relations (2.8) and (2.9) have a fundamental role in the study of turbulence since they are the simplest results that can be exactly derived from the conservation of mass, momentum and scalar by assuming the statistical stationarity, homogeneity and isotropy; from a practical point of view, they can be used as alternate means of determining experimentally $\langle \epsilon \rangle$ and $\langle \chi \rangle$ via measurements of both $\delta\theta$ and $\delta u_\parallel$ [9].

The simple dynamics highlighted in case of homogeneous and isotropic turbulence is drastically enriched by the symmetry breaking occurring in actual turbulent flows. The presence of statistical inhomogeneity, as an example, modifies the scale-by-scale budgets (2.4) and (2.5) by introducing a self-sustained production due to the interactions between mean gradients and Reynolds stresses/convective scalar flux, by introducing a transport in physical space and by spatially modulating the budgets. Fully-developed turbulent RBC is statistically stationary, statistically homogeneous and isotropic in the horizontal planes but inhomogeneous in the wall-normal direction. The symmetries of our flow can be exploited by considering a cylindrical coordinate system (ρ, ϕ, z) rather than the Cartesian system (x, y, z), where $\rho = \sqrt{x^2 + y^2}$ and $\phi = \arctan(y/x)$, as depicted in figure 1.1. The scale energy and scale variance budgets for RBC can be exactly derived from the governing equations (1.1)(a-c) following the procedure outlined by Hill [40] and reported in

appendix A. For a cylindrical coordinate system, the equations read as

$$\begin{aligned}
&-\frac{\partial\left\langle w^{\dagger}\delta u^{2}\right\rangle}{\partial z}-2\frac{\partial\left\langle \delta p\delta w\right\rangle}{\partial z}+\frac{1}{2}\sqrt{\frac{Pr}{Ra}}\frac{\partial^{2}\left\langle \delta u^{2}\right\rangle}{\partial z^{2}}-\frac{1}{r_{\rho}}\frac{\partial}{\partial r_{\rho}}\left(r_{\rho}\left\langle \delta u^{2}\delta u_{\rho}\right\rangle\right)\\
&-\frac{\partial\left\langle \delta u^{2}\delta w\right\rangle}{\partial r_{z}}+2\langle\delta\theta\delta w\rangle+\frac{2}{r_{\rho}}\sqrt{\frac{Pr}{Ra}}\frac{\partial}{\partial r_{\rho}}\left(r_{\rho}\frac{\partial\left\langle \delta u^{2}\right\rangle}{\partial r_{\rho}}\right)+2\sqrt{\frac{Pr}{Ra}}\frac{\partial^{2}\left\langle \delta u^{2}\right\rangle}{\partial r_{z}^{2}}\\
&-4\left\langle \tilde{\epsilon}^{\dagger}\right\rangle=0
\end{aligned}\tag{2.10}$$

and

$$\begin{aligned}
&-\frac{\partial\left\langle w^{\dagger}\delta\theta^{2}\right\rangle}{\partial z}+\frac{1}{2\sqrt{PrRa}}\frac{\partial^{2}\left\langle \delta\theta^{2}\right\rangle}{\partial z^{2}}-\frac{1}{r_{\rho}}\frac{\partial}{\partial r_{\rho}}\left(r_{\rho}\left\langle \delta\theta^{2}\delta u_{\rho}\right\rangle\right)-\frac{\partial\left\langle \delta\theta^{2}\delta w\right\rangle}{\partial r_{z}}\\
&-2\left\langle w^{\dagger}\delta\theta\right\rangle\frac{\partial\delta\Theta}{\partial z}-2\left\langle \delta w\delta\theta\right\rangle\left(\frac{d\Theta}{dz}\right)^{\dagger}+\frac{2}{r_{\rho}\sqrt{PrRa}}\frac{\partial}{\partial r_{\rho}}\left(r_{\rho}\frac{\partial\left\langle \delta\theta^{2}\right\rangle}{\partial r_{\rho}}\right)\\
&+\frac{2}{\sqrt{PrRa}}\frac{\partial^{2}\left\langle \delta\theta^{2}\right\rangle}{\partial r_{z}^{2}}-2\left\langle \chi^{\dagger}\right\rangle=0,
\end{aligned}\tag{2.11}$$

where † denotes the mid-point average $\beta^{\dagger}=(\beta(x_j-r_j/2)+\beta(x_j+r_j/2))/2$ for the generic variable β. The radial, the circumferential and the vertical components of the separation vector are, in order, r_ρ, r_ϕ and r_z, whereas the corresponding components of the velocity increment are δu_ρ, δu_ϕ and δw respectively. Let us point out that all the ϕ-derivative terms arising from the formulation in cylindrical coordinates are equal to zero for statistical isotropy.

The vertical inhomogeneity introduces an additional class of terms with respect to (2.4) and (2.5), namely the z-derivative terms, denoting the amount of scale energy and scale variance received (released) from (to) other wall-distances. The productions via the external forcing are replaced by the autonomous productions $2\left\langle \delta\theta\delta w\right\rangle$ and $-2\left\langle w^{\dagger}\delta\theta\right\rangle(\partial\delta\Theta/\partial z)-2\left\langle \delta w\delta\theta\right\rangle(d\Theta/dz)^{\dagger}$, which clearly arise from the spatial inhomogeneity. It should pointed out that, at sufficiently high Rayleigh numbers and far away from the boundaries, an inertial range is assumed to develop amid the separations; here, turbulence can be considered locally homogeneous and isotropic, the viscous and diffusive effects are rather negligible and the temperature acts like a passive scalar [57]. In this case, it is easy to demonstrate that (2.10) and (2.11) reduce to (2.8) and (2.9) after a few manipulations of the budgets.

Equations (2.10) and (2.11), hereafter referred to as Kolmogorov and Yaglom equations for RBC, are written in the complete physical/scale space domain (r_ρ, r_z, z). In order to make the scale-by-scale analysis more treatable, i.e. with less degrees of freedom, we lower the dimensionality of the budgets by considering a reduced (r_ρ, z)-space for $r_z = 0$, thus limiting the present investigation to the dynamics occurring at one-dimensional separations $(r_\rho; r_z = 0)$ and at different wall-distances z. The resulting *reduced* Kolmogorov and Yaglom equations can be expressed in the following

compact forms,

$$T_c^u + I_r^u + \Pi^u + E_e^u = 0, \tag{2.12}$$

$$T_c^\theta + I_r^\theta + \Pi^\theta + E_e^\theta = 0, \tag{2.13}$$

where $T_c^u = I_c^u + P + D_c^u$, $T_c^\theta = I_c^\theta + D_c^\theta$ are the overall transports in physical space and $E_e^u = D_r^u + E^u$, $E_e^\theta = D_r^\theta + E^\theta$ are the effective dissipations. The different contributions to the overall transports and effective dissipations are, in order,

$$I_c^u = -\frac{\partial \left\langle w^\dagger \delta u^2 \right\rangle}{\partial z},\ P = -2\frac{\partial \left\langle \delta p \delta w \right\rangle}{\partial z},\ D_c^u = \frac{1}{2}\sqrt{\frac{Pr}{Ra}}\frac{\partial^2 \left\langle \delta u^2 \right\rangle}{\partial z^2},$$
$$I_c^\theta = -\frac{\partial \left\langle w^\dagger \delta \theta^2 \right\rangle}{\partial z},\ D_c^\theta = \frac{1}{2\sqrt{PrRa}}\frac{\partial^2 \left\langle \delta \theta^2 \right\rangle}{\partial z^2},$$

and

$$D_r^u = 2\sqrt{\frac{Pr}{Ra}}\frac{1}{r_\rho}\frac{\partial}{\partial r_\rho}\left(r_\rho \frac{\partial \left\langle \delta u^2 \right\rangle}{\partial r_\rho}\right) + 2\sqrt{\frac{Pr}{Ra}}\frac{\partial^2 \left\langle \delta u^2 \right\rangle}{\partial r_z^2}\Big|_{r_z=0},\ E^u = -4\left\langle \tilde{\epsilon} \right\rangle,$$
$$D_r^\theta = \frac{2}{\sqrt{PrRa}}\frac{1}{r_\rho}\frac{\partial}{\partial r_\rho}\left(r_\rho \frac{\partial \left\langle \delta \theta^2 \right\rangle}{\partial r_\rho}\right) + \frac{2}{\sqrt{PrRa}}\frac{\partial^2 \left\langle \delta \theta^2 \right\rangle}{\partial r_z^2}\Big|_{r_z=0},\ E^\theta = -2\left\langle \chi \right\rangle,$$

whereas the transfers in the space of scales and the production terms are

$$I_r^u = -\frac{1}{r_\rho}\frac{\partial}{\partial r_\rho}\left(r_\rho \left\langle \delta u^2 \delta u_\rho \right\rangle\right) - \frac{\partial \left\langle \delta u^2 \delta w \right\rangle}{\partial r_z}\Big|_{r_z=0},\ \Pi^u = 2\left\langle \delta\theta \delta w \right\rangle,$$
$$I_r^\theta = -\frac{1}{r_\rho}\frac{\partial}{\partial r_\rho}\left(r_\rho \left\langle \delta \theta^2 \delta u_\rho \right\rangle\right) - \frac{\partial \left\langle \delta \theta^2 \delta w \right\rangle}{\partial r_z}\Big|_{r_z=0},\ \Pi^\theta = -2\left\langle \delta w \delta \theta \right\rangle \frac{d\Theta}{dz},$$

where $\beta^\dagger = \beta$ and the contribution of $-2\left\langle w^\dagger \delta\theta \right\rangle \partial\delta\Theta/\partial z$ to the overall production of scale variance is equal to zero as $\delta\Theta = 0$ for $r_z = 0$.

Equations (2.12) and (2.13) manifest a well-defined asymptotic behaviour as larger separations are considered. For $r_\rho \gg \ell_0$, where $\ell_0 = \ell_0(z)$ is the local integral scale, the variables evaluated at $(\rho + r_\rho/2, \phi, z)$ and $(\rho - r_\rho/2, \phi, z)$ are uncorrelated; thus (2.12) and (2.13) reduce, within a factor of four and two respectively, to the budgets of turbulent kinetic energy (2.1) and temperature variance (2.3); see appendix A for further details. In light of this result, the reduced Kolmogorov and Yaglom equations can be interpreted as a multi-scale extension of the classic single-point budgets. While the latter equations can only describe the cumulative dynamics associated to the entire range of scales, the former ones allow focusing on singular processes occurring at specific ranges of scales. It is worth stressing, once again, that the additional degree of freedom provided by (2.12) and (2.13) with respect to (2.1) and (2.3) have a crucial relevance in the study of turbulence due to the multi-scale nature of the phenomenon, as it will be discussed in what follows.

2.3.2 Analysis of the reduced Kolmogorov equation

In this section, the reduced Kolmogorov equation (2.12) is analyzed at some relevant wall-distances and mainly for $Ra = 1.0 \times 10^7$. The maximum separation considered, $r_\rho^* = 60 \approx 4Nu$, is imposed by the periodicity along x and y. The main panel in each figure displays the terms T_c^u, I_r^u, Π^u, D_r^u, E^u and their sum, $T_c^u + I_r^u + \Pi^u + D_r^u + E^u$, as a function of r_ρ^*, whereas the inset shows the different contributions to the overall transport in physical space T_c^u.

We start by considering the scale-by-scale budget inside the bulk region at $z^* = 6$. According to the single-point analysis discussed in section 2.2, this is the region where velocity fluctuations are produced and transported towards the wall essentially via pressure mechanisms. The examination of the reduced Kolmogorov equation in figure 2.9(a) enriches this picture by revealing a circumscribed range of separations where the production Π^u and the overall transport in physical space T_c^u are concentrated ($3 \lesssim r_\rho^* \lesssim 60$). We can argue that eddies of size larger than 3, besides producing most of the turbulent kinetic energy, extract energy from the bulk, being $T_c^u < 0$, to feed a spatial flux directed towards the wall. As shown in the inset of figure 2.9(a), the transport essentially occurs via pressure mechanisms, as the viscous component D_c^u is zero and the inertial contribution is rather lower in magnitude, i.e. $|P| \gg |I_c^u|$. The production/overall transport-dominated range is followed by an inertial-like range for $0.8 \lesssim r_\rho^* \lesssim 3$ that is characterized by the predominance of a positive inertial transfer, $I_r^u > 0$, with respect to the inhomogeneous terms, Π^u and T_c^u, and the viscous term D_r^u. Hence, the main role of turbulent scales between 0.8 and 3 is to receive energy from larger ones and to transfer it down through a direct cascade, which arguably would balance the dissipation in the limit of very high Rayleigh numbers, i.e. $I_r^u \approx E^u$. At even smaller separations ($r_\rho^* \lesssim 0.8$), the viscous term D_r^u increases steeply up to the dissipation E^u, suggesting that scales less than r_ρ^* start to be affected by viscosity and to dissipate the energy that comes from larger scales.

It is worth noting that production Π^u, inertial transport I_c^u and pressure transport P all reach a well-defined maximum around $r_\rho^* = 40$ meaning that turbulent kinetic energy is essentially produced and transported by eddies smaller than this characteristic length. Such an intriguing behaviour can be further investigated by expanding the production term as follows

$$\Pi^u(r_\rho, z) = \Pi_{\mathrm{I}}^u(z) - \Pi_{\mathrm{II}}^u(r_\rho, z),$$

where

$$\Pi_{\mathrm{I}}^u = 4\,\langle \theta w \rangle \;\text{ and }\; \Pi_{\mathrm{II}}^u = 4\,\langle \theta(\rho + r_\rho/2, \phi, z) w(\rho - r_\rho/2, \phi, z) \rangle$$

are, in order, four-times the production of turbulent kinetic energy and four-times the two-point cross-correlation between vertical velocity and temperature fluctuation. It is evident that, for every wall-distance, the maximum of Π^u occurs at the separation which maximizes $-\Pi_{\mathrm{II}}^u$ or, in other words, at the distance where w and

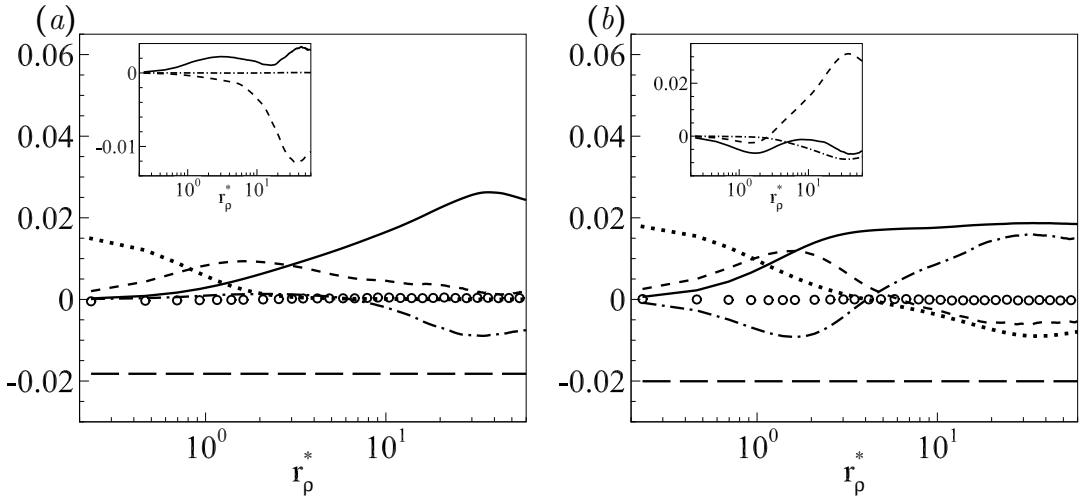

Figure 2.9: Terms of the reduced Kolmogorov equation (2.12) as a function of r_ρ^* inside (a) the bulk region at $z^* = 6$ and inside (b) the high transitional layer at $z^* = 0.6$ for $Ra = 1.0 \times 10^7$. Main panel: production Π^u (solid line), overall transport in physical space T_c^u (dot-dashed line), transfer in the space of scales I_r^u (dashed line), components of the effective dissipation, D_r^u (dotted line) and E^u (long-dashed line), and their sum $\Pi^u + T_c^u + I_r^u + D_r^u + E^u$ (circles). Inset: components of T_c^u, i.e. inertial transport I_c^u (solid line), pressure transport P (dashed line) and viscous transport D_c^u (dot-dashed line).

θ are maximally anti-correlated. Hence, the characteristic length $r_\rho^* = 40$ seems to be strictly connected with the flow topology, as it represents a measure of the average distance between warm fluid moving upwards and cold fluid moving downwards. A closer examination of figure 2.1(a,b) and 2.2 reveals that the warm and the cold clusters of plumes are separated by a distance $\ell_c \approx 2 \div 4$ or, in wall units, $\ell_c^* \approx 30 \div 60$. Therefore, we can argue from the correspondence between ℓ_c^* and $r_\rho^* = 40$ that most of the inhomogeneous mechanisms of production and transport are carried out by these coherent groups of thermal plumes, the so-called large-scale circulations or rolls.

The distinction between the scale-by-scale dynamics observed in the bulk for $r_\rho^* \gtrsim 3$ and for $r_\rho^* \lesssim 3$ corroborates the fundamental concept that, away from the boundaries and at sufficiently high Rayleigh numbers, only the large scales of the flow are affected by the spatial inhomogeneity while the small ones tend to recover a local homogeneous and isotropic state [49]. A completely different scenario can be observed closer to the wall, inside the outer part of the transitional layer at $z^* = 0.6$; see figure 2.9(b). The analysis of the reduced Kolmogorov equation in this location reveals that an inhomogeneity-dominated range, followed by an inertial direct cascade, is no more identifiable. Indeed, both the production and the overall transport in physical space are important throughout the entire range of separations,

while viscous dissipation is not limited to only small scales but substantially affects also the large ones, as can be observed from the negative peak of D_r^u around $r_\rho^* \approx 40$. For $r_\rho^* \gtrsim 5$, the net amount of turbulent kinetic energy produced and transported at scales less than r_ρ^* cannot be entirely dissipated at this wall-distance, i.e. $\Pi^u + T_c^u > |E_e^u|$; hence, velocity fluctuations start to flow towards larger scales in a so-called *reverse cascade* process ($I_r^u < 0$) to be eventually dissipated at other wall-distances. Indeed, as the integral scale ℓ_0 is approached, the inertial transfer I_r^u converges asymptotically to two-times the inertial transport of $\langle k \rangle$, i.e. $-2d \langle kw \rangle / dz$, meaning that energy cannot be transferred beyond ℓ_0 in the space of scales but only redirected to the physical space.

Beside the coexistence of direct and reverse cascades, it is worth noting the double feature of the overall transport in the high transitional layer, namely the positive value of T_c^u for $r_\rho^* \gtrsim 4$ and its negative value for $r_\rho^* \lesssim 4$. The eddies of length scale larger than 4 receive energy from the bulk region ($T_c^u > 0$) and this process involves only pressure mechanisms ($P > 0$) whereas inertia and viscosity act in opposition by draining energy from the transitional layer to feed the viscous layer ($I_c^u < 0$), albeit with less intensity ($|D_c^u| \ll |P|$ and $|I_c^u| \ll |P|$); see the inset of figure 2.9(b). On the other hand, turbulent scales less than 4 pump energy towards the wall region ($T_c^u < 0$) and this process occurs almost through inviscid mechanisms, since $T_c^u \approx I_c^u + P$. The double feature of the spatial flux can be explained as a compound effect of both the overall transport in physical space and the cascades in the space of scales. In more detail, inside the high part of the bulk (i.e. $z^* = 6$), the energy at large scales is transported towards the wall by means of pressure-velocity correlations ($P < 0$) and, simultaneously, is transferred to smaller scales in a direct cascade process ($I_r^u > 0$); see figure 2.9(a). As we move further down into the bulk region (i.e. $z^* = 5$), pressure mechanisms keep on draining energy at every scale to feed the transitional layer below ($P < 0$); however, it is possible to observe a reversal in the energy cascade at large scales ($I_r^u < 0$) though small eddies keep transferring energy to even smaller ones ($I_r^u > 0$). Following the concurrent effect of negative pressure transport and reverse cascade at large scales in the bulk of the flow, the first scales that gain energy from the inviscid transport inside the transitional layer are the larger ones. The small scales, on the other hand, remain somehow insulated and keep on feeding the spatial flux directed towards the wall.

The double feature of the overall transport can also be explained in terms of the flow topology. It has been remarked that large-scale circulations are responsible for producing much energy inside the bulk and for transporting it towards the transitional layer via pressure-velocity correlations. As the wall is approached, the largest coherent structures arguably feel the impermeability constraint imposed by the plate before the smaller ones, namely the individual thermal plumes, thus they are the first ones to enlarge and to release momentum to the horizontal planes. In support of this argument, we see in the inset of figure 2.9(b) that the positive pressure transport at large scales is peaked around $r_\rho^* = 40$, which corresponds to the characteristic length scale of the rolls observed in the bulk; see the maximum

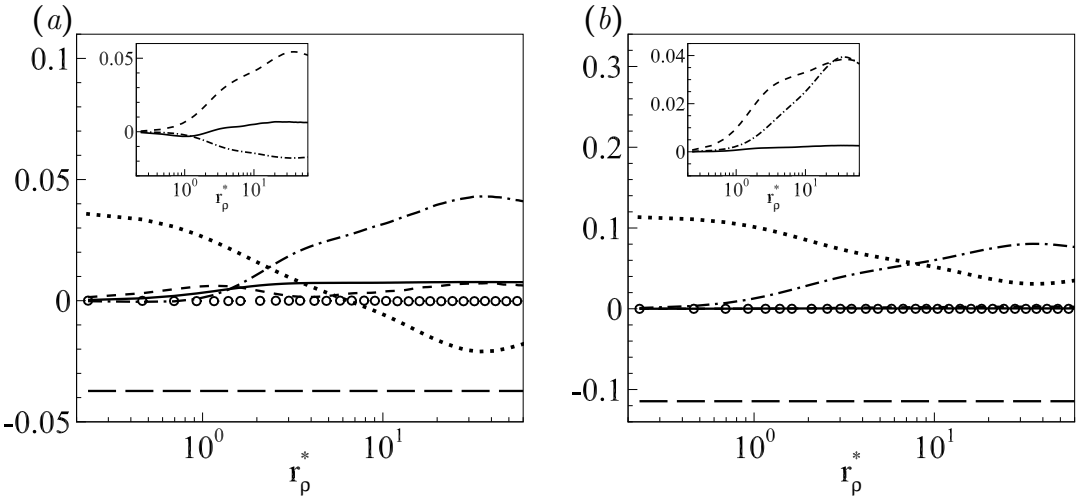

Figure 2.10: As figure 2.9 but inside (a) the low transitional layer at $z^* = 0.3$ and inside (b) the the viscous layer at $z^* = 0.1$.

of Π^u in figure 2.9(a). By contrast, few energetic plumes can penetrate further into the transitional layer without being affected by the vertical constraint; hence, they keep on transporting energy in the direction of the wall, which seems to justify the negative peak of T_c^u observed at small separations.

The scale-by-scale budget in the inner part of the transitional layer, precisely at $z^* = 0.2$, is represented in figure 2.10(a). Here, energy is almost entirely provided by transport mechanisms ($T_c^u > 0$) being the buoyant production rather negligible at large scales. As in the high transitional layer, the pressure contribution P is positive while the viscous one D_c^u is negative, meaning that energy is transported here by pressure-velocity correlations and drained further towards the wall by viscosity. The important difference that can been observed with respect to the scale-by-scale budget at $z^* = 0.6$ is the presence, albeit rather weak, of a pure direct cascade of energy ($I_r^u > 0$). The sharp transition from an compound direct/reverse cascade inside the high transitional layer to the direct cascade alone inside the low transitional layer seems worth of a deeper investigation and, with this purpose, we represent in figure 2.11(a) the isocontours of I_r^u in the $\left(r_\rho^*, z^*\right)$-space.

As anticipated in the previous paragraphs, energy starts to be transferred towards larger scales inside the bulk region around $z^* = 5$. However, as the wall is approached, the range of scales involved in the reverse cascade increases dramatically, reaching a maximum around $z^* = 0.4$, where $I_r^u < 0$ for $r_\rho^* \gtrsim 5$; see also the magnified plot in figure 2.11(b). Closer to the wall, for $z^* < 0.4$, a direct cascade is recovered at all separations and a reverse cascade cannot be found in the low transitional and viscous layers. The observed transition can be related to the behaviour of the coherent structures in the near-wall region. Indeed, it has been seen in figure 2.3(b) that the peak of $\langle div_\pi \rangle_+$, which quantifies the maximum impingement

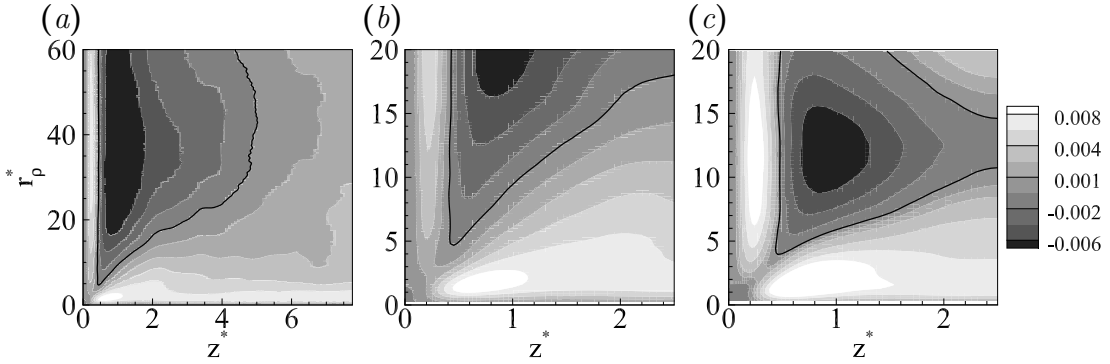

Figure 2.11: Isocontours of I_r^u in the $\left(r_\rho^*, z^*\right)$-space for (a) $Ra = 1.0 \times 10^7$ and (c) $Ra = 1.7 \times 10^5$. Figure (b) is a magnification of figure (a). The solid line indicates the level $I_r^u = 0$, namely the boundary between the direct and the reverse cascades.

of thermal plumes, occurs around $z^* = 0.3$, i.e. very close to the boundary between mixed and pure direct cascades. Furthermore, the minimum separation at which the reverse cascade occurs for $z^* = 0.4$, namely $r_\rho^* \approx 5$, is rather similar to the characteristic length of the plume spreading observed at $z^* \approx 0.3$, namely $r_\rho^* \approx 3$; see the inset in figure 2.3(b). According to these observations, the impingement of thermal plumes seems to delimit the range of scales and locations in physical space where the reverse cascade can occurs in RBC. This particular behaviour can be explained as follows. The enlargement of fluid patches along the horizontal directions can be reasonably associated with a transfer of energy towards larger scales. That said, since the thermal plume represents the smallest coherent structure that systematically spreads out on the wall, it is not surprising to find only a pure direct cascade below the impingement scale and/or inside the viscous layer where the impingement is negligible.

We conclude the multi-scale analysis by considering the reduced Kolmogorov equation in the viscous layer at $z^* = 0.1$; see figure 2.10(b). What emerges from the turbulent kinetic energy budget is that, inside this region, the dissipation balances the energy received from the transitional layer through viscous mechanisms. According to this result, the correspondent scale-by-scale budget highlights that production is negligible at all scales and that space transport sustains turbulent fluctuations balancing the effective dissipation. As can be seen in the inset of figure 2.10(b), energy is transported into the viscous layer essentially by viscous and pressure mechanisms, i.e. $T_c^u \approx P + D_c^u$. The very low intensity of inertial forces is underlined by the negligible magnitude of I_c^u and I_r^u. This result agrees with the common understanding that RBC can be fully-turbulent inside the bulk whereas it keeps a laminar state in the near-wall region, at least for Rayleigh numbers below the ultimate regime predicted by Kraichnan ($Ra \sim 10^{11}$ [17]) for which the viscous layers are argued to also become turbulent [50].

In the same way as the turbulent kinetic energy budget, the Rayleigh number

does not change the physical understanding of the multi-scale features highlighted up to now for the RBC, at least within the range of Ra considered in this study. Quantitatively speaking, the Rayleigh number is found to alter the magnitude of the terms in the scale-by-scale budget, however their qualitative behaviour in the (r_ρ^*, z^*)-space keeps almost unaltered. For example, it can be seen by comparing the isocontours of I_r^u for $Ra = 1.0 \times 10^7$ and for $Ra = 1.7 \times 10^5$ that the concurrent presence of direct and reverse cascades does not change with Ra; see figure 2.11(b,c). Indeed, the reverse cascade process is observed at both Ra, it takes place at the large scales in the bulk region and reaches its maximum closer to the wall around $z^* = 1$, whereas the direct cascade process characterizes the intermediate/small scales inside the bulk and transitional layer and all the scales inside the viscous layer, independently from the Rayleigh number.

Let us now discuss how the multi-scale description of RBC presented in terms of the reduced Kolmogorov equation could possibly extend our comprehension of the flow topology. As thoroughly described in section 2.1, thermal plumes are characterized by a well-defined life cycle. They detach from the thermal boundary layer and accelerate under the action of buoyancy forces throughout the bulk, thus accumulating turbulent kinetic energy due to the increasing vertical velocity, as confirmed by the profile of $\langle w^2 \rangle$ in figure 2.5(b). During their travel across the fluid layer, thermal plumes tend to pack together to form rolls having sizes comparable to the lateral extent of the computational domain. When eventually the clusters and the singular plumes approach the transitional layer and start feeling the impermeability constraint due to the opposite plate, the energy gained from the vertical acceleration is transferred from the wall-normal component to the wall-parallel ones by means of pressure-strain rate correlations. Sufficiently close to the wall, the turbulent kinetic energy is entirely associated to the horizontal motion (see the profile of $\langle u^2 \rangle$ in figure 2.5b) and from there is transported further towards the plate by viscous mechanisms where it is finally dissipated.

According to this sketch of the flow topology, the multi-scale analysis reveals that most of the turbulent kinetic energy is produced inside the bulk and transported closer to the wall by large-scale circulations. Furthermore, the reverse cascade observed in the high part of the bulk, from $3 \lesssim z^* \lesssim 5$, can be arguably associated with the grouping of thermal plumes into coherent packs. Indeed, we can imagine the clusterization process as energy migrating from small scales of the order of the plume diameter to larger ones of the order of the domain size. To support this argument, we see that the separation r_ρ^* for which $I_r^u < 0$ ranges from 30 to 60 in the high bulk, thus it is comparable with the typical size of the rolls, $\ell_c^* \approx 40$. The spreading of plume clusters due to the vertical constraint can reasonably explain the presence of a neat peak of reverse cascade at the edge between the bulk region and the transitional layer ($z^* \approx 1$) for $r_\rho^* \approx 40$. Finally, the enlargement of individual thermal plumes following the impingement represents the other mechanism responsible for the reverse cascade. Indeed, as the wall is approached, even smaller scales become interested by a reverse cascade and this trend is sharply interrupted in cor-

respondence of the maximum impingement. Furthermore, the smallest separation for which $I_r^u = 0$, $r_\rho^* \approx 5$, has been proved to match very well with the characteristic size of the plume spreading.

2.3.3 Analysis of the reduced Yaglom equation

We proceed by analyzing the reduced Yaglom equation (2.13) at some relevant wall-distances. The results are shown for $Ra = 1.0 \times 10^7$, unless otherwise stated. The terms T_c^θ, I_r^θ, D_r^θ, E^θ and their sum, $T_c^\theta + I_r^\theta + D_r^\theta + E^\theta$, are represented as a function of r_ρ^* in the main panel of each figure, whereas the inset shows the components of the overall transport, I_c^θ and D_c^θ.

Let us begin by considering the location $z^* = 6$ inside the thermal bulk. As shown by the single-point analysis, the core of the flow is a perfect sink for the thermal fluctuations, in the sense that it receives temperature variance from the near-wall region, without producing any of it, in order to sustain the local dissipation. Furthermore, the transport is carried out only by inertial mechanisms, since the diffusive effects are rather negligible away from the solid boundaries. The analysis of the scale-by-scale budget represented in figure 2.12(a) agrees with this picture, as the production Π^θ is nearly zero at all scales, whereas the overall transport T_c^θ is important in a wide range of separations and its major component is the inertial transport I_c^θ; see the inset in figure 2.12(a). As also shown by the reduced Kolmogorov equation, the reduced Yaglom equation reveals a neat distinction between scales inside the core of the flow. An inhomogeneous term, in this case T_c^θ rather than Π^θ, is dominant at large separations ($4 \lesssim r_\rho^* \lesssim 60$), whereas a direct cascade of temperature variance, $I_r^\theta > 0$, is the most relevant process at intermediate separations ($0.6 \lesssim r_\rho^* \lesssim 4$), where dissipation and transport mechanisms are subdominant, i.e. $|D_r^\theta| \lesssim |I_r^\theta|$ and $|T_c^\theta| \lesssim |I_r^\theta|$. At even smaller separations ($r_\rho \lesssim 0.6$), the diffusive term D_r^θ increases and approaches E^θ; hence, diffusivity becomes effective at scales smaller than 0.6 and temperature variance cascading from larger scales is gradually dissipated. Here, it is worth noting that the inertial transport in physical space does not exhibit an evident peak like in the reduced Kolmogorov equation; thus, a characteristic length of the inhomogeneous processes cannot be equally identified.

The scenario observed so far inside the thermal bulk changes significatively closer to the wall. Figure 2.12(b) represents the scale-by-scale budget (2.13) inside the high thermal transitional layer at $z^* = 0.75$. Here, the separation between large, inhomogeneous scales and small, dissipative ones is reduced with respect to the thermal bulk and an inertial-like range cannot be identified anymore. The analysis of the single-point budget of temperature variance plotted in figure 2.7(a) shows that the production steeply increases inside the thermal transitional layer, it overcomes dissipation and the resulting excess of temperature variance generated per unit time is transported towards the core and the wall by means of inertial mechanisms. The multi-scale description provided by the reduced Yaglom equation agrees with the single-point one; indeed, buoyant processes sustain a wide range of scales whereas

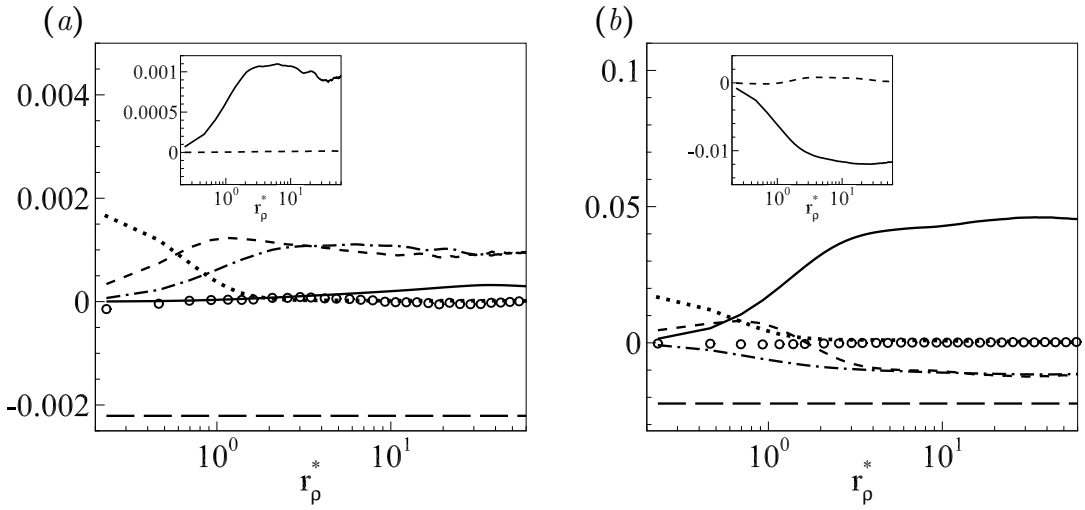

Figure 2.12: Terms of the reduced Yaglom equation (2.13) as a function of r_ρ^* inside (a) the thermal bulk at $z^* = 6$ and inside (b) the hight thermal transitional layer at $z^* = 0.75$ for $Ra = 1.0 \times 10^7$. Main panel: production Π^θ (solid line), overall transport in physical space T_c^θ (dot-dashed line), transfer in the space of scales I_r^θ (dashed line), components of the effective dissipations, D_r^θ (dotted line) and E^θ (long-dashed line), and their sum $\Pi^\theta + T_c^\theta + I_r^\theta + D_r^\theta + E^\theta$ (circles). Inset: components of T_c^θ, i.e. inertial transport I_c^θ (solid line) and diffusive transport D_c^θ (dashed line).

inertial mechanisms extract temperature variance to feed other wall-distances, as $T_c^\theta \approx I_c^\theta < 0$. The emerging picture can be further enriched by analyzing the inertial transfer in the space of scales I_r^θ. For $r_\rho^* \gtrsim 1.5$, the net amount of temperature variance produced and transported away at scales less than r_ρ^* cannot be entirely dissipated at this wall-distance, i.e. $\Pi^\theta + T_c^\theta > |E_e^\theta|$; hence, thermal fluctuations cannot cascade down to smaller scales but can only move towards larger ones in a reverse cascade process ($I_r^\theta < 0$) until they reach the integral scale the flow ℓ_0. From there, temperature variance is redirected to the physical space as I_r^θ becomes equal to the inertial transport of $\langle\theta^2\rangle$, namely $-d\langle\theta^2 w\rangle/dz$. Indeed, it should be recalled that the reduced Yaglom equation converges asymptotically to two-times the temperature variance budgets as r_ρ^* tends to ℓ_0.

In the lower part of the thermal transitional layer, precisely at $z^* = 0.4$, the single-point production reaches a maximum and the thermal diffusivity begins to play an important role in transporting temperature variance into the diffusive layer. Regarding the scale-by-scale budget plotted in figure 2.13(a), we can see that production, transport and diffusive effects are important all along the range of separations and superimpose on each other to create more complex dynamics. Both inertial and diffusive mechanisms contribute to the overall transport T_c^θ; however, the components D_c^θ and I_c^θ are comparable at small scales whereas D_r^θ is substantially larger than D_r^θ at larger scales; see the inset in figure 2.13(a). We conclude the inspec-

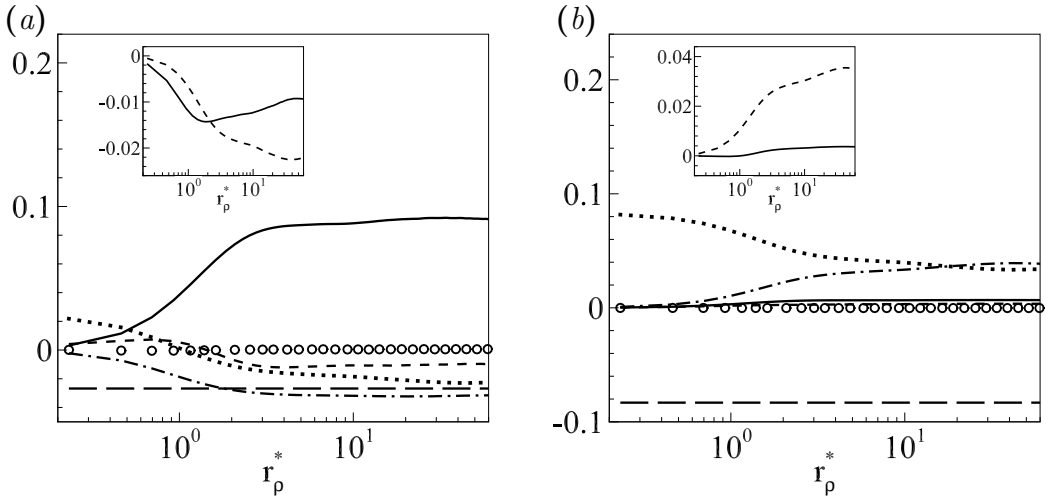

Figure 2.13: As figure 2.12 but inside (a) the low thermal transitional layer at $z^* = 0.4$ and (b) the diffusive layer at $z^* = 0.1$.

tion at different wall-distances by considering the scale-by-scale budget within the diffusive layer, at $z^* \approx 0.1$; see figure 2.13(b). The comparison of this picture with the one referring to the thermal bulk region at $z^* = 6$ (see figure 2.12a) reveals a reasonable similarity since both regions lack in production and receive scale energy from the thermal transitional layer, $T_c^\theta > 0$. The fundamental contribution to the overall transport term is the diffusive component D_c^θ. Furthermore, the temperature variance received at every scale is locally dissipated (in the scale space) as $T_c^\theta \approx -E_e^\theta$. The fact that both the inertial transport I_c^θ and the inertial transfer I_r^θ are negligible supports the presence of a laminar regime in the near-wall region.

The cascade of temperature variance shows some similarities with the cascade of energy, as can be seen by comparing the isocountour plots in figure 2.14(a) and 2.11(a). In particular, the inertial transfer in the space of scales I_r^θ manifests a sharp transition from a compound direct/reverse cascades to a pure direct cascade around $z^* = 0.3$; see also the magnified plot in figure 2.14(b). Once again, the observed behaviour can be associated with the plume dynamics; indeed, the location of maximum impingement ($z^* \approx 0.3$) corresponds perfectly to wall-distance at which the transition occurs, while the characteristic diameter of the impinging plume ($r_\rho^* \approx 3$) is rather similar to the minimum separation which divides direct from reverse cascades, namely $r_\rho^* \approx 1.5$. Finally, the peak of reverse cascade observed at large separations and for $z^* \approx 0.5$ can be reasonably seen as a statistical footprint of the enlargement of plume clusters, in accordance with the interpretation given to the analogous behaviour observed in figure 2.11(a) for the energy cascade.

We conclude this section by remarking that the multi-scale analysis of the temperature field does not change qualitatively with respect to the Rayleigh number. This behaviour clearly emerges from the comparison of the inertial transfer I_r^θ for

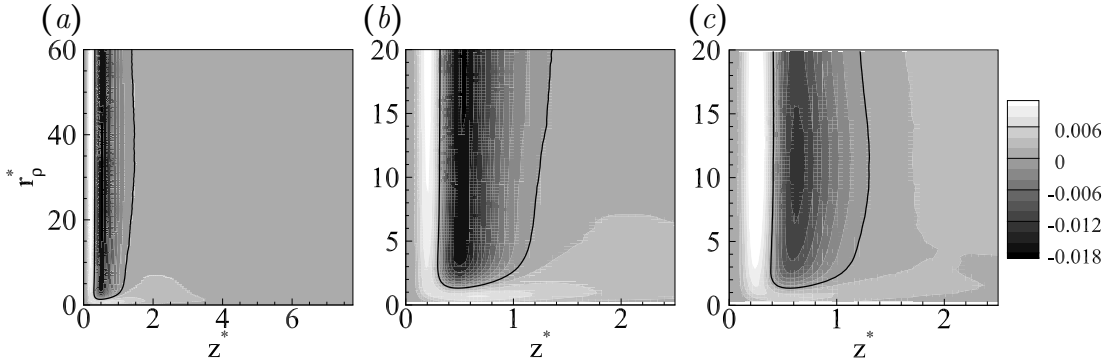

Figure 2.14: Isocontours of I_r^θ in the $\left(r_\rho^*, z^*\right)$-space for (a) $Ra = 1.0 \times 10^7$ and (c) $Ra = 1.7 \times 10^5$. Figure (b) is a magnification of figure (a). The solid line indicates the level $I_r^\theta = 0$, namely the boundary between the direct and the reverse cascades.

$Ra = 1.0 \times 10^7$ with the correspondent one at $Ra = 1.7 \times 10^5$, which are plotted in figure 2.14(b,c) respectively. Though the intensity of the term changes with Ra, the behaviour in the $\left(r_\rho^*, z^*\right)$-space keeps essentially unaltered and this feature also characterizes the other terms of the budget. These results suggest that the same dynamics of the coherent structures affect the flows at the different Ra considered, even though the qualitative details of the plumes and the rolls change dramatically from $Ra = 1.7 \times 10^5$ to $Ra = 1.0 \times 10^7$, since the structures become less smooth and more chaotic due to turbulent mixing.

2.3.4 Characteristic scales of the flow

In this section, we attempt to rationalize the complex scenario emerging from the analysis of the scale-by-scale budgets by identifying some fundamental regions in the reduced (r_ρ^*, z^*)-space. According to the remarks made in § 2.3.2 and § 2.3.3, it seems reasonable to split the range of separations into an inhomogeneity-dominated range at large r_ρ^* and a quasi-homogeneous range at small r_ρ^*, where the velocity and temperature crossover scales, named ℓ_c^{u*} and $\ell_c^{\theta*}$ respectively, satisfy the following relations

$$\begin{aligned} \Pi^u(\ell_c^{u*}, z^*) + T_c^u(\ell_c^{u*}, z^*) &= I_r^u(\ell_c^{u*}, z^*) + D_r^u(\ell_c^{u*}, z^*), \\ \Pi^\theta(\ell_c^{\theta*}, z^*) + T_c^\theta(\ell_c^{\theta*}, z^*) &= I_r^\theta(\ell_c^{\theta*}, z^*) + D_r^\theta(\ell_c^{\theta*}, z^*). \end{aligned} \tag{2.14}$$

Generally speaking, the fundamental mechanisms that characterize eddies of size smaller than ℓ_c^{u*} and $\ell_c^{\theta*}$ are the energy/temperature variance transfers towards smaller scales and the relative dissipations, whereas eddies of size larger than ℓ_c^{u*} and $\ell_c^{\theta*}$ contribute to the inhomogeneous processes of production and transports in physical space. Inside the inhomogeneous range, the combined action of production and transports significantly modulates the transfer in the space of scales and may entail a reversal of energy/temperature variance transfers. Regarding the latter behavior, it is worthwhile to introduce also the boundary scales ℓ_b^{u*} and $\ell_b^{\theta*}$, such

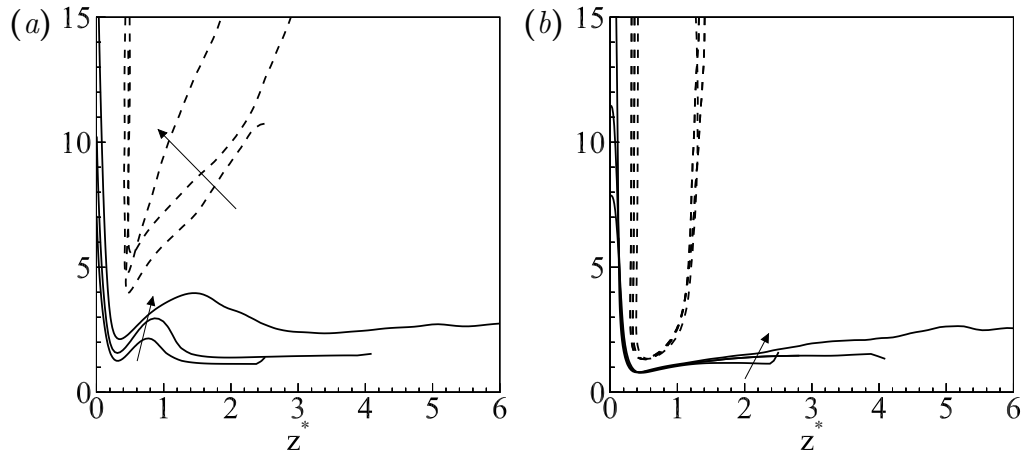

Figure 2.15: (a) Velocity crossover scale ℓ_c^{u*} (solid lines) and boundary scale ℓ_b^{u*} (dashed lines), (b) temperature crossover scale $\ell_c^{\theta*}$ (solid lines) and boundary scale $\ell_b^{\theta*}$ (dashed lines) for $Ra = 1.7 \times 10^5$, $Ra = 1.0 \times 10^6$ and $Ra = 1.0 \times 10^7$, where the Rayleigh number increases in the direction of the arrows.

that

$$I_r^u(\ell_b^{u*}, z^*) = 0, \;\; I_r^\theta(\ell_b^{\theta*}, z^*) = 0, \tag{2.15}$$

in order to separate the direct cascades from the reverse cascades, completing a brief portrait of the flow that accounts for the most relevant turbulent processes in the physical and scale space.

The characteristic scales of the velocity and temperature field are represented as a function of the wall-distance in figure 2.15(a,b) for $Ra = 1.7 \times 10^5$, $Ra = 1.0 \times 10^6$ and $Ra = 1.0 \times 10^7$. As can be seen, the boundary scales between direct and reverse cascades, ℓ_b^{u*} and $\ell_b^{\theta*}$, exceed the corresponding crossovers between small, quasi-homogeneous scales and large, inhomogeneous scales, ℓ_c^{u*} and $\ell_c^{\theta*}$, at every distance from the wall. All the characteristic scales of the flow reach a minimum value close to the boundaries, around $z^* \approx 0.2 \div 0.6$; however, while ℓ_c^{u*} and $\ell_c^{\theta*}$ can be defined along the entire domain height, ℓ_b^{u*} and $\ell_b^{\theta*}$ exist only sufficiently close to the wall where direct and reverse cascades coexist at different ranges of scales; see figures 2.11(a-c) and 2.14(a-c).

It is interesting to note that the characteristic scales of the temperature field are essentially independent from the Rayleigh number, whereas the characteristic scales of the velocity field increase rather monotonically with the Rayleigh number. What we observe is related to the fact that the balanced terms of the Yaglom equation do not change in shape along r_ρ^* and z^*; hence, the crossover scale $\ell_c^{\theta*}$ and the boundary scale $\ell_b^{\theta*}$ are unaltered by the Rayleigh number according to their definitions (2.14) and (2.15). On the other hand, the terms of the Kolmogorov equation are slightly modulated in shape, thus ℓ_c^{u*} and ℓ_b^{u*} depend on Ra. In light of these observations, the smallest characteristic scale of the flow is fixed by the temperature field and

corresponds to $l^{\theta*}_{c,min} \approx 0.8$ independently from the Rayleigh number. Furthermore, the temperature field is supposed to set the minimum characteristic scale also for $Pr > 0.7$, as the diffusive scales decrease in size with respect to the viscous ones.

As will be discussed in chapter 4, the crossover scales have a strong repercussion on the modelling approach of thermally driven turbulence, especially in a LES context. Indeed, the relative position of the filter length with respect to the crossover scales determines what mechanisms can be directly solved and what others can only be accounted for by the turbulence model.

2.4 Summarizing remarks

Despite the simple configuration, turbulent RBC exhibits very rich and complex behaviours due to the presence of a forcing, namely the buoyancy, that is naturally embedded in the flow rather that being provided from the outside. A view of the flow topology reveals that the system organises itself into a fascinating hierarchy of coherent structures that seem responsible for the sustainment of turbulent fluctuations. Indeed, thermal plumes follow a precise life cycle along which they gain, transport and dissipate energy and temperature variance. Portions of warm and cold fluid detach from the thermal boundary layers and grow into mushroom-like plumes as they are pulled up by the buoyancy force. Meanwhile, thermal plumes group together into ascending and descending clusters separated by a distance that is comparable to the lateral size of the computational domain. The kinetic energy collected by the coherent structures across the fluid layer is partially dissipated during the impingement onto the opposite wall and partially used to mechanically extract sheet-like structures from the viscous region, which intersect each other and give birth to new thermal plumes, closing the life cycle.

The autonomous cycle of turbulence outlined by the flow topology has been examined in more detail by means of the turbulent kinetic energy and the temperature variance budgets. The single-point analysis allows us to define some specific regions along z where the turbulent processes of production, transport in physical space and dissipation take place. With regard to the energetics of the flow, a bulk region is identified in the core, where velocity fluctuations are produced and transported by pressure mechanisms into a transitional layer closer to the wall. There, the energy received from the bulk exceeds the local production and the net excess with respect to dissipation diffuses further towards the wall into a viscous layer, where it is completely dissipated. Regarding the evolution of temperature variance, a thermal bulk region, a thermal transitional layer and a diffusive layer are identified analogously to the regions based on the flow energetics. In this case, however, the thermal transitional layer is the actual source region, where the production of temperature variance is stronger and abundantly exceeds the dissipation. The net amount of temperature variance that is generated inside the thermal transitional layer is transferred to the thermal bulk and the diffusive layer by inertial and dif-

fusive mechanisms respectively, and then dissipated.

The autonomous cycle of turbulence is multi-scale by nature, in the sense that its fundamental processes depend not only on the location in physical space but also on the length scale considered. That said, the single-point analysis cannot describe the phenomenon in its full complexity as it addresses only the behaviour in physical space and not in the space of scales. To overcome this limitation, a theoretical framework based on the analysis of the Kolmogorov and Yaglom equations is employed for the first time to study the turbulent RBC. An important information that can be obtained following this approach is how the spatial inhomogeneity modulates the dynamics of the flow at different scales. Inside the bulk, the space of scales can be partitioned into three ranges: an inhomogeneity-dominated range at large scales, an inertial-like range at intermediate scales and a dissipative range at small scales. This scenario, which is typical of homogeneous and isotropic turbulence, breaks close enough to the wall. Indeed, inhomogeneous mechanisms, namely production and transport in physical space, and viscous/diffusive processes are important all along the range of scales and superimpose on each other to create more complex dynamics, which is characterised, for example, by the reversal of the energy and temperature variance cascades. Some relevant features of the scale-by-scale analysis have been explained in terms of the coherent structures of the flow. It has been reasonably proved that the large-scale circulations carry out most of the production and transport of energy. Furthermore, the cascade reversal has been attributed to three distinct phenomena, namely the plumes clusterization inside the bulk, the spreading of the groups of plumes in the lower part of the bulk region and the impinging of individual plumes inside the transitional layer.

The multi-scale description of RBC may have a relevant impact on some theoretical studies of thermally driven turbulence. For example, a subject of intense debate nowadays is the existence of the so-called Bolgiano-Obukhov regime in unstably stratified flows and several studies have been conducted in the simplified framework of RBC, as nicely summarized in the review article by Lohse and Xia [57]. The Bolgiano-Obukhov regime is assumed to occur at scales that are sufficiently small for the hypothesis of local homogeneity and isotropy to be valid, but large enough such that the buoyant production exceeds the viscous dissipation, i.e. $I_r^u \approx -\Pi^u$. Although this work supports the existence of a Kolmogorov regime in the core of RBC and for sufficiently high Rayleigh numbers ($I_r^u \approx -E^u$), there is nothing to suggest that a Bolgiano-Obukhov regime would ever develop, since the condition $I_r^u \approx -\Pi^u$ seems to be much more difficult to fulfill due to the dynamics of the flow.

The multi-scale analysis is also of primary importance in LES modelling. Indeed, the study of the Kolmogorov and Yaglom equations allows to evaluate the leading physical processes governing the turbulent velocity and temperature fields in thermally driven flows. In particular, the assessment of these processes in the compound physical/scale space domain actually matters for the filtering operation in LES, as it will be discussed in depth in chapter 4.

Chapter 3

Analysis of rotating Rayleigh-Bénard convection

In this chapter, the Rayleigh-Bénard convection (RBC) is studied with an additional complexity, i.e. the rotation around the vertical axis. The physics of rotating Rayleigh-Bénard convection (RRBC) appears to be very rich and to drift away from the behaviour of RBC highlighted in chapter 2. Particular attention is given to the observed transition from a weakly rotating ($1/Ro \lesssim 0.67$) to a rapidly rotating regime ($1/Ro \gtrsim 0.67$), which has been reported in past studies (see, e.g., the review by Stevens *et al.* [87]) and is still a subject of discussion [96]. The former regime is characterised by a heat transport enhancement ($Nu/Nu_0 > 1$), as the extra suction by Ekman pumping exceeds the suppression of vertical motion induced by rotation, whereas the latter regime exhibits a depletion of the heat flux ($Nu/Nu_0 < 1$) and a substantial damping of the turbulent motion. In what follows, the dynamical evolution of RRBC is addressed by a qualitative view of the instantaneous fields and by a quantitative statistical analysis. This approach, which mostly retrace the one presented in chapter 2 for RBC, allows us to depict a clearer picture of the flow and, in particular, to disclose the nature of the aforementioned transition.

3.1 Flow topology

The flow topology of turbulent RBC changes in many respects under rotation. It can be seen by comparing figure 3.1(a,d) in absence of rotation ($1/Ro = 0$) with figures 3.1(b,e) at $1/Ro = 0.5$ and 3.1(c,f) at $1/Ro = 2$ that the network of sheet-like roots becomes denser and the number of ejected structures per unit area increases sensibly with the angular frequency. It has been argued that rotation tends to suppress the clusterization phenomenon and to favour the merging of thermal plumes [70]. In agreement with this idea, the pattern of sheet-like roots observed for $1/Ro > 0$ seems to be more homogeneous with respect to the non-rotating case, as mushroom-like plumes tend to merge with their neighbours rather than converge into few spots

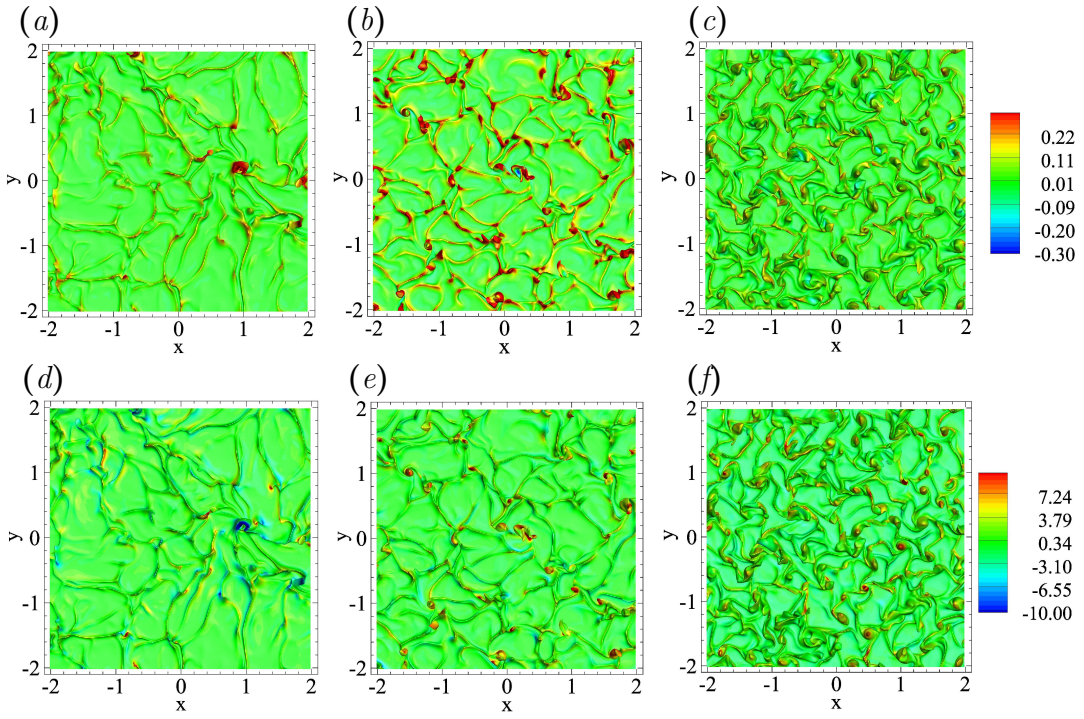

Figure 3.1: Top view of the isosurface of temperature $\theta^\star = 0.25$ for (a,d) $1/Ro = 0$, (b,e) $1/Ro = 0.5$, (c,f) $1/Ro = 2$ coloured by $(a\text{-}c)$ the vertical velocity $w^\star$ and by $(d\text{-}f)$ the vertical vorticity $\omega^\star$. Note that only a portion of the entire computational domain is represented for clarity.

to establish a large-scale circulation; see also the vertical sections coloured by the temperature in figure 3.2(a,b). The suppression of the mean wind ensures that the average distance between ascending and descending plumes becomes the largest scale of the flow when rotation is strong enough. Since the ejected plumes move closer to each other as $1/Ro$ increases, the integral scale decreases and so does the minimum aspect-ratio of the domain that is required to capture the largest scale that would arise naturally in the flow. In this work, the same domain of aspect-ratio 8 is employed for all the simulations, although smaller ones could have been used for the rotating cases [52]. It should be remarked, however, that an oversize domain guarantees all the scales to be solved without the need for *a posteriori* evidences and ensures a fast convergence of the statistical quantities, that is to say, it reduces the time T required for each simulation; see table 1.1 for further details.

One striking effect of rotation on the flow topology is the impression of a positive-signed (or cyclonic) vertical vorticity on the ejected plumes; see figure 3.1$(d\text{-}f)$. The observed phenomenon can be readily explained as follows. The fluid in the thermal boundary layer, which initially rotates together with the walls, is forced to converge into the sheet-like roots by the mechanical action of the impinging plumes. This mechanism causes a large concentration of cyclonic wall-normal vorticity in

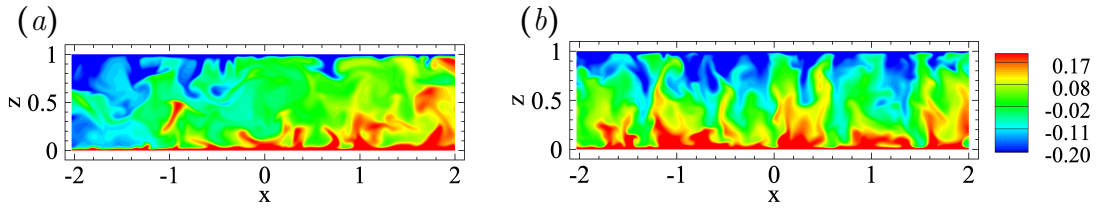

Figure 3.2: Vertical section at $y = 0$ coloured by the temperature $\theta^\star$ for (a) $1/Ro = 0$ and (b) $1/Ro = 2$. For clarity, only a portion of the domain is represented.

the intersection spots between different crests, and thus to the ejection of vertical rotating plumes from the thermal boundary layer. As can be seen by comparing figure 3.1(d) with 3.1(e) and 3.1(f), the structures in absence of rotation can be either cyclonic or anti-cyclonic, whereas rotation favours cyclonic plumes. As the average of the wall-normal vorticity on the horizontal planes must be zero due to the lateral periodicity, the thermal plumes characterized by an intense cyclonic vorticity are separated by the weak, anti-cyclonic vorticity of the turbulent background.

In presence of a mild rotation rate (see figure 3.1b) the vertical momentum of the sheet-like roots and the mushroom-like plumes is stronger with respect to both the non-rotating and the rapidly rotating case; see, in order, figure 3.1(a,c). Furthermore, the shape of the structures changes drastically from thin and slender at $1/Ro = 0$ and $1/Ro = 0.5$ to short and thick at $1/Ro = 2$. The competition between two opposite effects of rotation, namely the Ekman pumping and the flow bi-dimensionalization in the horizontal planes, seems to drive this particular evolution of the flow topology. The first mechanisms is an extra suction of mass from the near-wall region due to the interaction of fluid patches having an intense cyclonic vertical vorticity, namely the rotating thermal plumes, with the no-slip horizontal plates [42]. The Ekman pumping favours the extraction of sheet-like roots from the thermal boundary layers and the ejection of slender plumes characterized by an intense vertical motion. The second effect is a consequence of the Taylor-Proudman theorem, which states that the velocity components does not depend on the vertical position in the geostrophic regime, i.e. when the Coriolis force can be considered large compared with inertial, viscous and buoyancy forces or, in terms of non-dimensional numbers, $1/Ro \gg 1$ and $\sqrt{Ra/Pr} \gg 1$ [89]. In RRBC, the presence of a solid boundary perpendicular to the rotation axis implies that $w^\star \approx 0$ at the interface between the geostrophic region localized in the bulk and the non-geostrophic viscous layer; hence, the vertical velocity is nearly zero throughout the entire fluid layer whereas $u^\star$ and $v^\star$ are almost independent from the vertical position and, generally speaking, different from zero. According to this scenario, rotation tends to suppress the vertical motion and to generate bidimensional structures having a column-like shape and extending parallel to the rotating axis [46]. The pattern of these so-called convective Taylor columns is visible for $1/Ro = 2$ (see figure 3.1f and 3.2b), whereas lower rotation rates bring to more energetic and less organised structures.

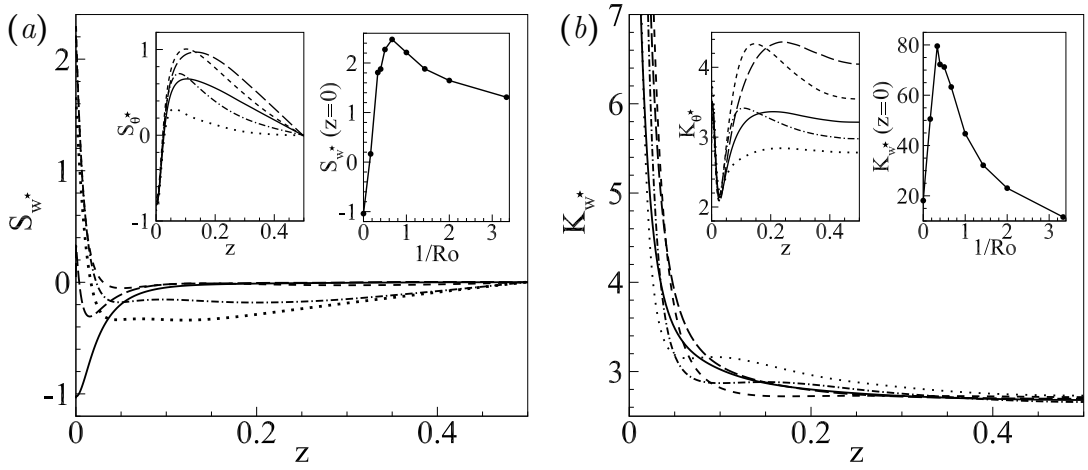

Figure 3.3: Main figures: (a) skewness and (b) kurtosis of $w^\star$. Left insets: (a) skewness and (b) kurtosis of $\theta^\star$. The different lines correspond to $1/Ro = 0$ (solid line), $1/Ro = 0.17$ (long-dashed line), $1/Ro = 0.5$ (dashed line), $1/Ro = 1$ (dot-dashed line) and $1/Ro = 2$ (dotted line). Right insets: (a) skewness and (b) kurtosis of $w^\star$ evaluated at the wall ($z = 0$) as a function of $1/Ro$.

The evolution of the flow topology with respect to the rotation rate can be studied in some more detail by analyzing the skewness and the kurtosis of $w^\star$ and $\theta^\star$ for different $1/Ro$; see figure 3.3(a,b). Contrary to the statistical analysis of RBC where the independent variables are normalized with H/Nu to compare results at different Ra, in this case we do not find an analogous characteristic scale to compare results at different Ro; thus, statistical observables are hereafter expressed as a function of spatial variables that are simply normalized by H. In absence of rotation, $S_{w^\star}$ presents a negative peak at the wall, meaning that strong and intermittent downward fluid motions are favoured by the proximity to the lower boundary. This scenario changes completely in presence of rotation, as the vertical velocity skewness at the wall becomes positive at very little angular frequencies ($1/Ro < 0.17$) and increases sensibly with $1/Ro$. At sufficiently high rotation rates ($1/Ro \geq 0.5$), the strong upward fluid motion becomes the preferential event for $z \lesssim 0.03$ and this behaviour reaches a well-defined maximum for $1/Ro = 0.67$; see the right inset in figure 3.3(a). In the same near-wall region, $K_{w^\star}$ assumes the largest values for $1/Ro = 0.33$, which means that the frequency of extreme events is maximally enhanced by fairly small angular frequencies; see the right inset in figure 3.3(b). Regarding the high-order statistical moments of temperature, the analysis of $S_{\theta^\star}$ and $K_{\theta^\star}$ reveals that inside the near-wall region ($z \lesssim 0.03$) $\theta^\star$ is more likely to assume large negative values by intermittent events that become even more frequent as the wall is approached; furthermore this behaviour seems not to be affected by the rotation rate as the profiles at different $1/Ro$ almost collapse onto a single curve.

In view of the flow topology, the positive value of the vertical velocity skewness observed for $z \lesssim 0.03$ is reasonably attributable to the enhancement of fluid ejection due to the Ekman pumping, whereas the negative value of the temperature skewness in the same region is indicative of cold thermal plumes reaching the lower wall and impinging onto the hot thermal boundary layer. It is interesting to observe that, in presence of rotation, the most intermittent kinetic and thermal events in the near-wall region are, in order, the ejections and the impingements of plumes, whereas for $1/Ro = 0$ the impingements are responsible alone for the large negative values of $w^\star$ and, at the same time, the large positive values of $\theta^\star$ observed for $z \lesssim 0.03$.

Inside the core of the flow ($z \gtrsim 0.03$), $S_{w^\star}$ is negative or equal to zero at every rotation rate and $K_{w^\star}$ do not exhibit noteworthy variations with respect to $1/Ro$. In more detail, the magnitude of the vertical velocity skewness increases with $1/Ro$ throughout the bulk, meaning that localized downwards motions of fluid are favoured by rotation. In the same region, $S_{\theta^\star}$ is positive and reaches a maximum for $1/Ro = 0.33$. Here, it is worth noting that a similar trend is observed also for the $K_{\theta^\star}$. The interpretation of $S_{\theta^\star}$ and $K_{\theta^\star}$ in the core agrees with the picture highlighted up to now from the kinematic point of view. Indeed, the ejection events driven by the Ekman pumping, which seem to reach their maximum intensity between $1/Ro = 0.33$ (in correspondence with the peak of $K_{w^\star}$ at the wall) and $1/Ro = 0.67$ (in correspondence of the peak of $S_{w^\star}$ at the wall) are responsible for transporting warm fluid portions from the lower plate to the core that is, on average, colder; hence, it is not surprising to find that positive-temperature events are maximally intense and frequent around $1/Ro = 0.33$. This scenario agrees with the qualitative analysis of the flow topology and, in particular, with the observation that thermal plumes are ejected more vigorously at mild rotation rates.

3.2 Single-point analysis

The influence of rotation on the different mechanisms of thermal convection can be further characterized in terms of single-point equations. Let us begin by considering the turbulent kinetic energy budget,

$$-\frac{d\langle kw\rangle}{dz} - \frac{d\langle wp\rangle}{dz} + \sqrt{\frac{Pr}{Ra}}\frac{d^2\langle k\rangle}{dz^2} + \langle w\theta\rangle - \langle\tilde{\epsilon}\rangle = 0. \tag{3.1}$$

This balance is formally identical to the one in absence of rotation (see equation (2.1)), as the Coriolis force acts orthogonal to the instantaneous motion and therefore can do no work. However, the shape and the magnitude of the different terms are actively modulated by $1/Ro$ through the change of the velocity field, thus highlighting the rotational effects on the flow dynamics.

In figure 3.4(a,b), the terms of the turbulent kinetic energy budget (2.1) are plotted as a function of z for $1/Ro = 0$ and $1/Ro = 2$ respectively. Independently from the rotation rate, the flow can still be separated into a bulk region, a

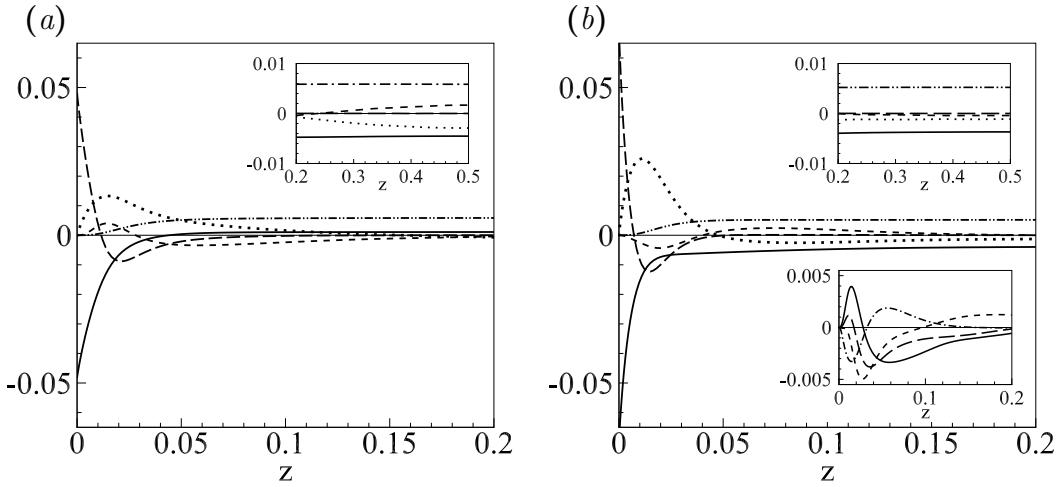

Figure 3.4: (a) Terms of the turbulent kinetic energy budget (2.1) as a function of z, for $Ra = 1.0 \times 10^7$ and $1/Ro = 0$: inertial transport (dashed line), pressure transport (dotted line), viscous transport (long-dashed line), production (dot-dot-dashed line) and dissipation (solid line); the details of the bulk are shown in the inset. The main plot and the top inset of figure (b) are the same of figure (a) but for $1/Ro = 2$. The lower inset represents the inertial transport for $1/Ro = 0$ (solid line), 0.33 (long-dashed line), 0.67 (dashed line) and 3.33 (dot-dashed line).

transitional layer and a viscous layer. Turbulent fluctuations are produced inside the bulk, namely the core of the flow, and then transported essentially via pressure mechanisms towards the transitional layer, from where they diffuse into the viscous layer to be mostly dissipated; see § 2.2 for a thorough description of the flow regions and the processes that characterize them. By comparing the budgets for $1/Ro = 0$ and the ones for $1/Ro > 0$, we observe no substantial qualitative differences except for the inertial transport, $-d\langle kw\rangle/dz$. In absence of rotation, turbulent kinetic energy is drained by inertial mechanisms inside the high transitional layer and the low bulk region ($0.025 \lesssim z \lesssim 0.2$), where $-d\langle kw\rangle/dz < 0$, to feed the remaining areas next to wall ($z \lesssim 0.025$) and to the centerline ($z \gtrsim 0.25$), where $-d\langle kw\rangle/dz > 0$. The inertial mechanisms behave exactly in the opposite way if we consider a sufficiently high rotation rate. Indeed, they deplete the viscous and transitional layer, from one side, and the high part of the bulk, from the other, to feed the region amid them. This behaviour has been observed for $1/Ro$ down to 0.67 since, for lower angular frequencies, the inertial transport becomes positive at the border between the viscous and the transitional layers and tends to take the shape seen in absence of rotation; see the lower inset in figure 3.4(b)

A further insight into the RRBC dynamics can be obtained by considering the budgets of the distinct components of turbulent kinetic energy, namely $\langle u^2\rangle$, $\langle v^2\rangle$ and $\langle w^2\rangle$, as done previously for the RBC in section 2.2. Hereafter, we consider only the budgets of $\langle u^2\rangle$ and $\langle w^2\rangle$ (see equations (2.2)a,c), since the budgets of

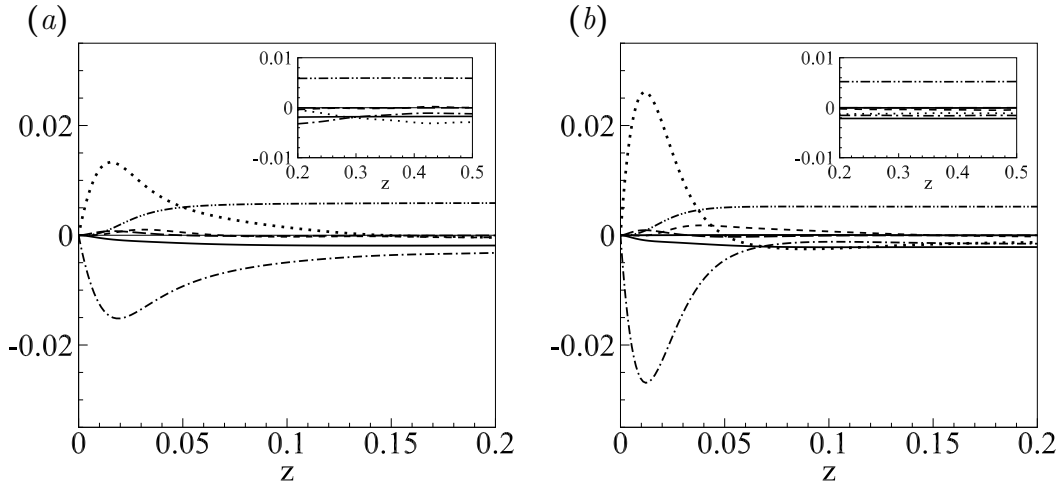

Figure 3.5: Terms of the budget of $\langle w^2 \rangle$, (2.2)(c), for (a) $1/Ro = 0$ and (b) $1/Ro = 2$: inertial transport (dashed line), pressure-strain rate term (dot-dashed line), pressure transport (dotted line), viscous transport (long-dashed line), production (dot-dot-dashed line) and dissipation (solid line); the details of the bulk region are shown in the inset.

$\langle u^2 \rangle$ and $\langle v^2 \rangle$ are identical due to statistical symmetries. The main features of the component-by-component analysis of the turbulent kinetic energy budget have been already discussed in § 2.2; hence, the focus of this part is mainly concerned with the differences arising in presence of rotation. Figure 3.5(a,b) represents the budgets of the vertical turbulent kinetic energy $\langle w^2 \rangle$ for $1/Ro = 0$ and $1/Ro = 2$. The pressure transport, $-d \langle wp \rangle / dz$, and the pressure-strain rate term, $\langle p \partial w / \partial z \rangle$, are mostly affected by the rotation rate, whereas the other balanced terms remain almost unaltered. In more detail, these terms are modulated in magnitude rather than in shape and both are found to increase with $1/Ro$. By comparing the budgets of $\langle u^2 \rangle$ in the non-rotating case and for a sufficiently high rotation rate (see figure 3.6a,b), it can be seen that, apart from the different magnitudes of the balanced terms, the budget changes relatively to the inertial transport, $-0.5d \langle u^2 w \rangle / dz$. Indeed, it presents the same opposite behaviour shown by the inertial transport in the full budget of turbulent kinetic energy, meaning that horizontal velocity fluctuations are swept away from the transitional layer, where $-0.5d \langle u^2 w \rangle / dz < 0$, and transported into the bulk region, where $-0.5d \langle u^2 w \rangle / dz > 0$. Moreover, at lower rotation rates, the inertial transport of $\langle u^2 \rangle$ is found to become positive close to the wall, in the same way as the inertial transport of $\langle k \rangle$ does. In light of these results, we can claim that the characteristic inversion of the inertial transport observed in the full budget of turbulent kinetic energy is due exclusively to a change in the dynamics of the horizontal velocity components due to a sufficiently strong rotation rate.

In order to shed more lights on the mechanisms behind the reverse of the inertial transport, we subtract the budgets of $\langle w^2 \rangle$ and $\langle u^2 \rangle$ at $1/Ro = 0$ from the

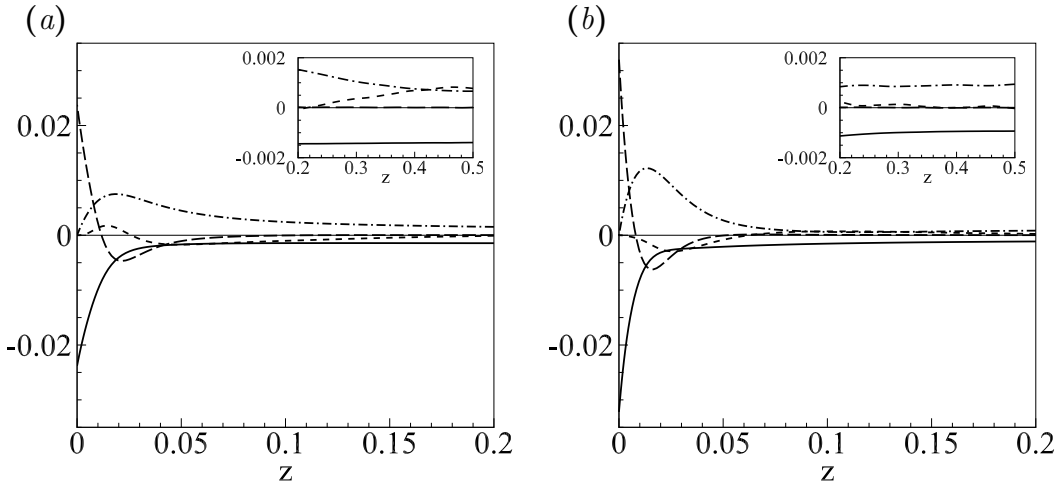

Figure 3.6: Terms of the budget of $\langle u^2 \rangle$, (2.2)(a), for (a) $1/Ro = 0$ and (b) $1/Ro = 2$: inertial transport (dashed line), pressure-strain rate term (dot-dashed line), viscous transport (long dashed line) and dissipation (solid line); the details of the bulk region are shown in the inset.

corresponding ones evaluated for $1/Ro > 0$. The resulting equations, written in a compact form, read as

$$\Delta i_c^w + \Delta p_{sr}^w + \Delta p + \Delta d_c^w + \Delta \pi + \Delta e^w = 0, \tag{3.2}$$

$$\Delta i_c^u + \Delta p_{sr}^u + \Delta d_c^u + \Delta e^u = 0, \tag{3.3}$$

where

$$\Delta i_c^w = -\frac{1}{2}\frac{d\,\langle w^3 \rangle}{dz}\,(1/Ro > 0) + \frac{1}{2}\frac{d\,\langle w^3 \rangle}{dz}\,(1/Ro = 0)\,,$$
$$\Delta i_c^u = -\frac{1}{2}\frac{d\,\langle u^2 w \rangle}{dz}\,(1/Ro > 0) + \frac{1}{2}\frac{d\,\langle u^2 w \rangle}{dz}\,(1/Ro = 0)$$

are the differences between the inertial transports,

$$\Delta p_{sr}^w = \left\langle p\frac{\partial w}{\partial z} \right\rangle (1/Ro > 0) - \left\langle p\frac{\partial w}{\partial z} \right\rangle (1/Ro = 0)\,,$$
$$\Delta p_{sr}^u = \left\langle p\frac{\partial u}{\partial x} \right\rangle (1/Ro > 0) - \left\langle p\frac{\partial u}{\partial x} \right\rangle (1/Ro = 0)$$

are the differences between the pressure-strain rate terms,

$$\Delta d_c^w = \frac{1}{2}\sqrt{\frac{Pr}{Ra}}\frac{d^2\,\langle w^2 \rangle}{dz^2}\,(1/Ro > 0) - \frac{1}{2}\sqrt{\frac{Pr}{Ra}}\frac{d^2\,\langle w^2 \rangle}{dz^2}\,(1/Ro = 0)\,,$$
$$\Delta d_c^w = \frac{1}{2}\sqrt{\frac{Pr}{Ra}}\frac{d^2\,\langle u^2 \rangle}{dz^2}\,(1/Ro > 0) - \frac{1}{2}\sqrt{\frac{Pr}{Ra}}\frac{d^2\,\langle u^2 \rangle}{dz^2}\,(1/Ro = 0)$$

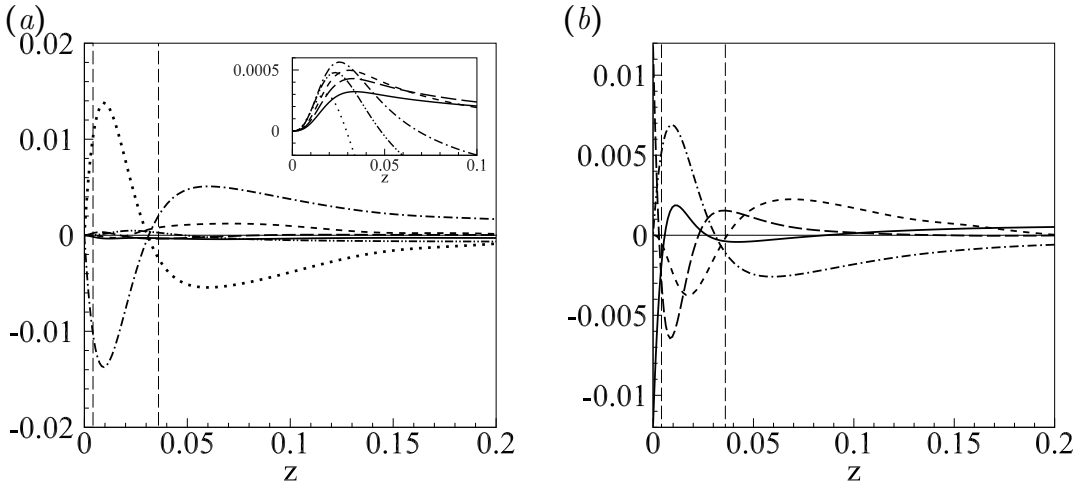

Figure 3.7: (a) Terms of the budget (3.2) and (b) (3.3) for $1/Ro = 2$: Δi_c^w and Δi_c^u (dashed line), Δp_{sr}^w and Δp_{sr}^u (dot-dashed line), Δp (dotted line), $\Delta\pi$ (dot-dot-dashed line), Δd_c^w and Δd_c^u (long-dashed), Δe^w and Δe^u (solid line). The vertical dashed lines denote the limits between the viscous layer, the transitional layer and the bulk. Inset: profile of $\Delta\pi$ for $1/Ro = 0.33$ (solid line), 0.5 (long dashed line), 0.67 (dashed line), 1.43 (dot-dashed line), 2 (dot-dot-dashed line), 3.33 (dotted line).

are the differences between the viscous transports,

$$\Delta e^w = -\langle\tilde{\epsilon}_z\rangle\,(1/Ro > 0) + \langle\tilde{\epsilon}_z\rangle\,(1/Ro = 0)\,,$$
$$\Delta e^u = -\langle\tilde{\epsilon}_x\rangle\,(1/Ro > 0) + \langle\tilde{\epsilon}_x\rangle\,(1/Ro = 0)$$

are the differences between the dissipations,

$$\Delta p = -\frac{d\,\langle wp\rangle}{dz}\,(1/Ro > 0) + \frac{d\,\langle wp\rangle}{dz}\,(1/Ro = 0)\,,$$
$$\Delta\pi = \langle w\theta\rangle\,(1/Ro > 0) - \langle w\theta\rangle\,(1/Ro = 0)$$

are the differences between the pressure transports and productions respectively.

Figure 3.7(a,b) shows the budgets (3.2) and (3.3) as a function of z and for $1/Ro = 2$. For $z \lesssim 0.1$, the main difference between the rotating and the non-rotating vertical dynamics concerns the pressure transport and the pressure-strain rate term, as Δp and Δp_{sr}^w are larger in magnitude with respect to the other terms of the budget (3.2). The presence of rotation seems to favour the extraction of turbulent kinetic energy by means of pressure mechanisms throughout the bulk region ($\Delta p < 0$) to feed the transitional layer ($\Delta p > 0$). In parallel to this process, Coriolis forces tend to impede the inter-component exchange of turbulent kinetic energy inside the core of the flow ($\Delta p_{sr}^w > 0$) whereas a sudden release of energy from the vertical component to the horizontal ones eventually occurs inside the transitional layer ($\Delta p_{sr}^w < 0$) due to the presence of the wall. The buoyant production

shows an increased value inside the transitional layer ($\Delta\pi > 0$) for every $1/Ro$ considered in this study, while the difference in the bulk is very small or negative; see the inset in figure 3.7(a). As the production term $\langle w\theta \rangle$ corresponds to the convective heat flux, the observed behaviour is a clear indication of an added vertical heat transfer caused by rotation. Furthermore, the heat flux enhancement $\Delta\pi > 0$ increases monotonically from $1/Ro = 0$ to $1/Ro = 1.43$, where it reaches a maximum around $z = 0.25$, and then it decreases for higher rotation rates.

The effect of rotation on the horizontal dynamics is possibly even more rich. The inspection of figure 3.7(b) reveals that the horizontal dissipation is significantly reduced by rotation inside the inner part of the transitional layer and in the high bulk ($\Delta e^u > 0$) whereas it is enhanced in the viscous layer and in the lower part of the bulk ($\Delta e^u < 0$). Here, it should be pointed out that the sum of horizontal dissipations corresponds almost to the entire dissipation, i.e. $\langle \tilde{\epsilon}_x \rangle + \langle \tilde{\epsilon}_y \rangle \approx \langle \tilde{\epsilon} \rangle$, since the vertical contribution is rather negligible, i.e. $\langle \tilde{\epsilon}_z \rangle \approx 0$, as can be seen in figure 3.5(a,b). The compound effect of rotation on the inter-component exchange of energy Δp^u_{sr} (which corresponds to $-\Delta p^w_{sr}/2$ since the sum of the pressure-strain rate terms is zero for incompressibility) and on the horizontal dissipation $\langle \tilde{\epsilon}_x \rangle$ modulate the balance (3.3) in such a way that an excess of turbulent kinetic energy is provided to the transitional and viscous layer with respect to the non-rotating case, i.e. $\Delta p^u_{sr} + \Delta e^u > 0$ for $0.003 \lesssim z \lesssim 0.03$. This increment is partially drained by a rotation-induced enhancement of the viscous transport directed towards the wall ($\Delta d^u_c < 0$) and partially by a reversed inertial transport ($\Delta i^u_c < 0$) that extracts energy from the transitional layer to sustain the bulk.

As regards the analysis of the temperature variance budget (2.3), the rotation rate does not alter the shape of the balanced terms but rather modulates their magnitude; see figure 3.8(a,b) for $1/Ro = 0$ and $1/Ro = 2$. While the budget keeps almost unaltered close to the wall, the effect of rotation is more evident inside the thermal transitional layer and inside the thermal bulk, especially as regards the inertial transport, $-d\langle \theta^2 w \rangle / dz$, and the production, $-2\langle w\theta \rangle d\Theta/dz$. Here, it should be pointed out that the production of temperature variance is positive and nearly constant inside the thermal bulk for $1/Ro = 2$. Indeed, rotation introduces a mean negative temperature gradient in the core of the flow that is not present in RBC and that monotonically increases with $1/Ro$; compare the inset in figure 2.7(b) with the lower inset in figure 3.8(b).

The study of the single-point budgets allows us to greatly enrich the picture of RRBC outlined in section 3.1 in terms of the flow topology. According to the Taylor-Proudman theorem, rotation tends to bidimensionalize the flow in the horizontal planes; hence, thermal plumes in RRBC are prevented from enlarging too much inside the bulk region ($\Delta p^u_{sr} < 0$), but they eventually do it when they impinge onto the solid walls, thus releasing a large amount of energy to the horizontal motion inside the transitional layer ($\Delta p^u_{sr} > 0$). The excess of energy in the near-wall region is partially drained by inertial mechanisms and transported towards the bulk, as indicated by the negative value of the inertial transport inside the transitional

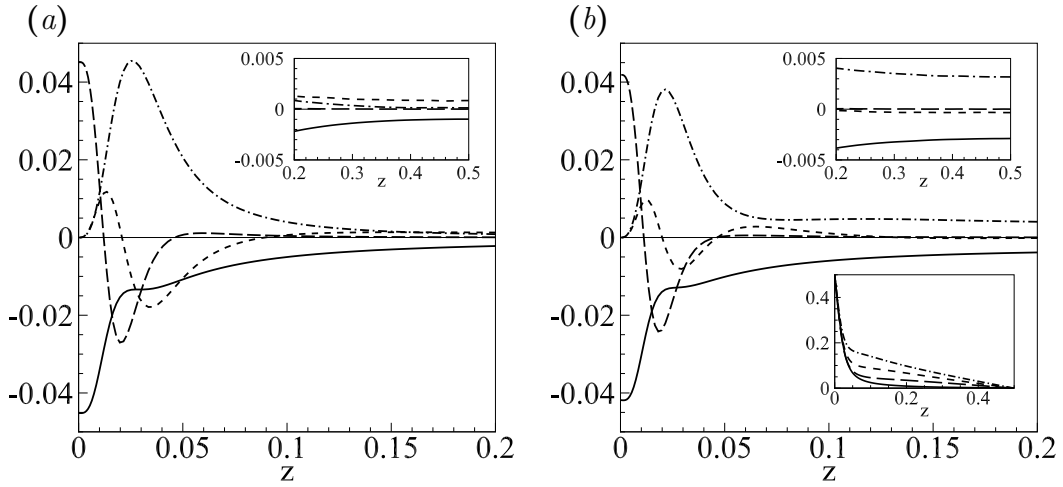

Figure 3.8: (a) Terms of the temperature variance budget (2.3) as a function of z, for $Ra = 1.0 \times 10^7$ and $1/Ro = 0$: inertial transport (dashed line), diffusive transport (long-dashed line), production (dot-dashed line) and dissipation (solid line); the details of the bulk region are shown in the inset. The main plot and the top inset of figure (b) are the same of figure (a) but for $1/Ro = 2$. The lower inset represents the average temperature profile for $1/Ro = 0$ (solid line), 0.5 (long-dashed line), 1 (dashed line) and 2 (dot-dashed line).

layer. This is arguably the statistical footprint of the sucking action attributable to rotating plumes, which is commonly referred to as Ekman pumping. In support of this argument, we see that the inertial transport reaches a negative peak around $1/Ro = 0.67$ (see the lower inset in figure 3.4b), which means that the fluid extraction is maximum for a mild rotation rate in agreement with the analysis of the flow topology. Furthermore, it has been observed that rotation enhances the convective heat flux inside the transitional layer ($\Delta\pi > 0$); see the inset in figure 3.7(a). This second behaviour is not surprising since a greater suction of warm and cold fluid from the viscous layers should entail a larger heat transport across the layer.

We conclude this section by pointing out that the mean temperature gradient observed in presence of rotation is attributable to the efficient lateral mixing via the stirring actions and merging of rotating plumes. Indeed, if a warm fluid portion mixes with the surrounding at a given wall-distance, it loses its temperature contrast with respect to that level. In turn, the surrounding becomes warmer than if the lateral mixing had not occurred and the thermal stratification occurs [42].

3.3 Effect of rotation on the boundary layers

The main result emerging from the analysis of the turbulent kinetic energy budget is that, in presence of sufficiently high rotation rates, velocity fluctuations are trans-

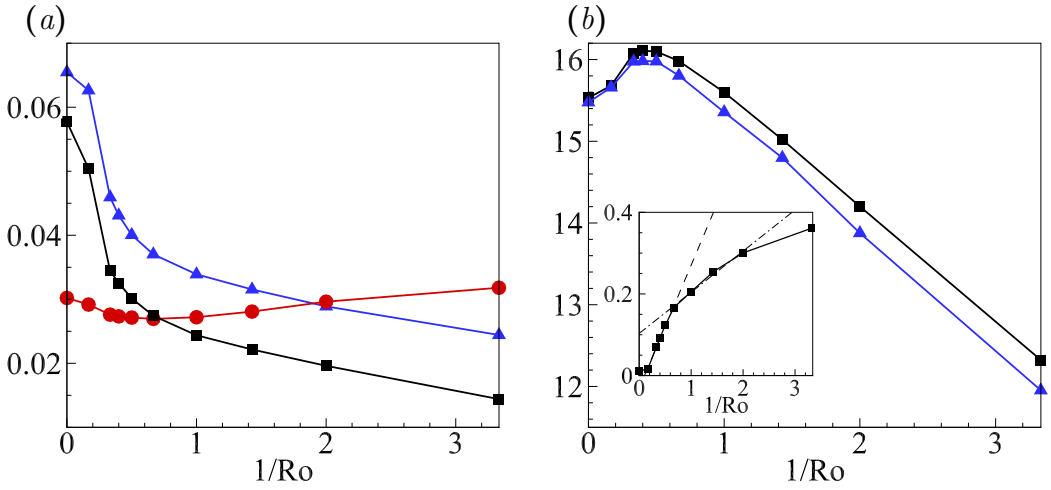

Figure 3.9: (a) Main figure: thermal boundary layer thickness δ_θ (red circles), viscous boundary layer thickness δ_u (blue triangles) and location of the maximum Ekman pumping z_{max} (black squares) as a function of $1/Ro$. (b) Profile of the volume-averaged Nusselt number $\langle Nu \rangle_V$ (black squares) and the convective component Nu_{cv} at the centerline (blue triangles). Inset: profile of the conductive component Nu_{cd} at the centerline (black squares). The dashed and dot-dashed lines show $Nu_{cd} = (0.3/Ro) - 0.03$ and $Nu_{cd} = (0.1/Ro) + 0.1$ respectively.

ported away from the viscous and transitional layers towards the core of the flow by means of inertial mechanisms. The gradual reverse of the inertial transport reflects the evolution of the flow topology. Indeed, the pattern observed in absence of rotation, characterized by few thermal plumes grouping into clusters, evolves into a denser pattern of rotating vortices having a strong upward velocity when $1/Ro$ is not too large. In the previous section, the location where the reverse transport of turbulent kinetic energy is peaked has been associated with the maximum fluid extraction via the Ekman pumping; thus, we hereafter denote with z_{max} this particular wall-distance, i.e.

$$z_{max} = \underset{z\in[0,0.5]}{\arg\max} \frac{d\,\langle kw \rangle}{dz}.$$

Figure 3.9(a) represents the thermal and viscous boundary layer thickness, respectively δ_θ and δ_u, together with z_{max} as a function of $1/Ro$. Here, δ_θ and δ_u are defined by looking at the wall-distances where the maximum temperature and horizontal velocity variances occur, i.e.

$$\delta_\theta = \underset{z\in[0,0.5]}{\arg\max} \left\langle \theta^2 \right\rangle \quad \text{and} \quad \delta_u = \underset{z\in[0,0.5]}{\arg\max} \left\langle u^2 \right\rangle.$$

It can be observed that z_{max} and δ_u have similar profiles, which seems to be quite reasonable if we consider that fluid ejections give shape to the viscous boundary

layer. Starting from $1/Ro = 0$ and increasing the rotation rate, z_{max} becomes smaller and approaches δ_θ. The thermal boundary layer thickness, on the other hand, depletes and reaches a minimum around $1/Ro = 0.67$ where $\delta_\theta \approx z_{max}$. The gradual depletion of δ_θ seems to be caused by two concurrent mechanisms: the movement of the maximum Ekman pumping towards the edge of the thermal boundary layer and the increasing intensity of the suction process. Regarding the latter, we can argue that the fluid extraction becomes even more effective as z_{max} decreases down to δ_θ because it favours the natural ejection of thermal plumes developing out of buoyant instability at the edge of the thermal boundary layer. Here, it should be noticed that the negative peak of the inertial transport observed for $1/Ro = 0.67$ (see the lower inset in figure 3.4b) clearly supports this phenomenological interpretation. For non-dimensional rotation rates larger than $1/Ro = 0.67$, the maximum Ekman pumping occurs within the thermal boundary layer. As z_{max} crosses δ_θ, the thermal boundary layer begins to thicken arguably for two reasons. Firstly, because some fluid is pulled out from under the edge of the thermal boundary layer and, secondly, because rotation has a stabilizing effect on the thermal boundary layer and allows it to thicken further with respect to the non-rotating case [15].

The relative position of the maximum Ekman pumping and the thermal boundary layer determines how much rotation can affect the heat transport in RRBC. As can be seen from figure 3.9(b), the volume-averaged Nusselt number $\langle Nu \rangle_V$ increases inititally with the rotation rate, it reaches a plateau for $0.33 \lesssim 1/Ro \lesssim 0.5$ and then it decreases steeply, falling below the non-rotating value around $1/Ro = 1$. The heat flux enhancement observed at some angular frequencies is a feature of rotating convection that is well-known since the early experiment conducted by Rossby [80]. The most common explanation given to this phenomenon is that the Ekman pumping exceeds the suppression of vertical motion at low angular frequencies, thus the convective heat flux is enhanced by rotation rather than being depleted. On the other hand, the kinematic constraint resulting from the Taylor-Proudman theorem overcomes the beneficial effect of the Ekman pumping at sufficiently high rotation rates, with a consequent reduction of the Nusselt number. The unbalance between the two mechanisms has been ascribed by King *et al.* [47] to the relative thicknesses of the viscous and thermal boundary layers. According to this theory, a weakly rotating regime can be identified when $\delta_u > \delta_\theta$. In this case, the Coriolis forces are argued to have a small effect on the flow dynamics, as the uppermost part of the viscous boundary layer is mixed with the bulk and thus the influence of rotation on the boundary dynamics is truncated. The opposite occurs when $\delta_u < \delta_\theta$, in the rapidly rotating regime, as the Coriolis forces shape the thermal boundary layer and regulate the ejection of thermal plumes.

The analysis of the present data suggests that a transition from a weakly rotating to a rapidly rotating regime occurs when the thermal boundary layer thickness δ_θ exceeds the location of maximum Ekman pumping z_{max} rather than the viscous boundary layer thickness δ_u, as the plateau of $\langle Nu \rangle_V$ occurs very close to the crossover between δ_θ and z_{max}. This result seems to be reasonable if we consider that

the Ekman suction is maximally efficient at the edge of the thermal boundary layer and that the fluid extracted from there has a sharp temperature contrast with the surrounding, thus contributing in a substantial way to the convective heat flux. To better support this argument, we split the Nusselt number in two distinct contributions, namely the conductive component $Nu_{cd} = -d\Theta/dz$ and the convective component $Nu_{cv} = \sqrt{PrRa}\,\langle w\theta \rangle$. The two contributions to the Nusselt number evaluated at the centerline ($z = 0.5$) are represented in the main figure and in the inset of figure 3.9(b). As can be seen, the profiles of Nu_{cv} and $\langle Nu \rangle_V$ have similar shapes and they are both peaked around the same rotation rate; therefore, the enhancement of the total heat flux originates from the enhancement of the convective heat flux that, in turn, can be associated with the stronger upward and downward motions induced by the Ekman pumping. It should be remarked that the conductive contribution Nu_{cd} is different from zero in presence of rotation, although it is rather small. An evident change in the slope of Nu_{cd} passing from $0.17 < 1/Ro < 0.67$ to $0.67 < 1/Ro < 2$ represents a further evidence of the transition from a weakly rotating to a rapidly rotating regime.

3.4 Analysis of the reduced Kolmogorov equation

The assessment of rotating convection via single-point budgets allows us to depict a clear picture of the flow dynamics and, in addition, to explain one of the most intriguing features of RRBC, namely the heat flux enhancement occurring at some rotation rates. Nonetheless, the description provided up to now is still incomplete since it lacks of focus on the scale-by-scale dynamics. This aspect seems worth a deeper investigation for two distinct reasons. Firstly, the remarkable evolution of the flow topology from the non-rotating case to the rotating one suggests also a noteworthy change in the multi-scale physics. As an example, it has been shown in figures 3.1(a-d) and 3.2(a,b) that the Coriolis forces inhibit the formation of large-scale circulations, which are the coherent structures that mostly produces and transport energy in non-rotating convection; see § 2.3.2. Secondly, we may be interested in identifying the length scale at which the Ekman pumping occurs; indeed, this knowledge could be helpful for modelling purposes or for the development of control techniques to maximize the heat exchange.

In this section we address to the multi-scale dynamics of RRBC by analyzing the reduced Kolmogorov equation (2.12). This budget has been introduced in section 2.3.1 and thoroughly analyzed in section 2.3.2 for the RBC case. Since the Coriolis forces can do no work on the system, the reduced Kolmogorov equation derived in absence of rotation is formally identical to the one in presence of rotation. However, the terms of the budget are effectively modulated by $1/Ro$ through the change of the velocity field. A pedantic description of the balance at several wall-distances and rotation rates is beyond the purpose of this section; hence, we highlight just the relevant changes in the multi-scale dynamics by comparing the results in absence of

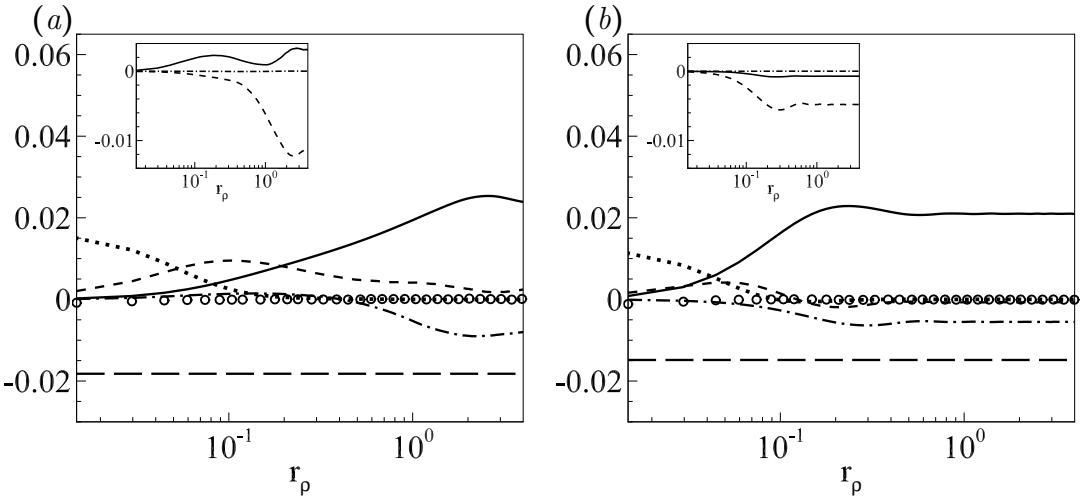

Figure 3.10: Terms of the reduced Kolmogorov equation as a function of r_ρ inside the bulk at $z = 0.4$ for (a) $1/Ro = 0$ and for (b) $1/Ro = 1$. Main panel: production Π^u (solid line), overall transport in physical space T_c^u (dot-dashed line), transfer in the space of scales I_r^u (dashed line), components of the effective dissipation, D_r^u (dotted line) and E^u (long-dashed line), and their sum $\Pi^u + T_c^u + I_r^u + D_r^u + E^u$ (circles). Inset: components of T_c^u, i.e. inertial transport I_c^u (solid line), pressure transport P (dashed line) and viscous transport D_c^u (dot-dashed line).

rotation with the ones for an intermediate rotation rate ($1/Ro = 1$) at two locations in physical space, namely inside the bulk ($z = 0.4$) and inside the transitional layer ($z = 0.025$). Here, it should be anticipated that a similar multi-scale analysis will not involve the reduced Yaglom equation, as the budget has been proved to exhibit a weak dependence on the rotation rate, similarly to the temperature variance budget, and therefore it does not add significative information to the study already presented in section 2.3.3 for the RBC case.

Figure 3.10(a,b) represents the reduced Kolmogorov equation at $z = 0.4$, for $1/Ro = 0$ and $1/Ro = 1$. Analogously to the scale-by-scale budgets represented in section 2.3.2, the main panel in each figure displays the overall transport in physical space T_c^u, the inertial transfer in the space of scales I_r^u, the production Π^u, the viscous term D_r^u and the two components of the effective dissipation, D_r^u and E^u, as a function of the radial separation r_ρ. The inset shows the different contributions to the overall transport in physical space, namely the inertial transport I_c^u, the pressure transport P and the viscous transport D_c. The first thing that can be noticed by comparing 3.10(a) and 3.10(b) is that, in presence of rotation, the balanced terms become r_ρ-invariant after the rather small separations $r_\rho \approx 10$, implying that the reduced Kolmogorov equation becomes almost equal to four-times the turbulent kinetic energy budget for $r_\rho \gtrsim 10$. The convergence of the scale-by-scale budget to the single-point one occurs for separations sufficiently larger than the local integral

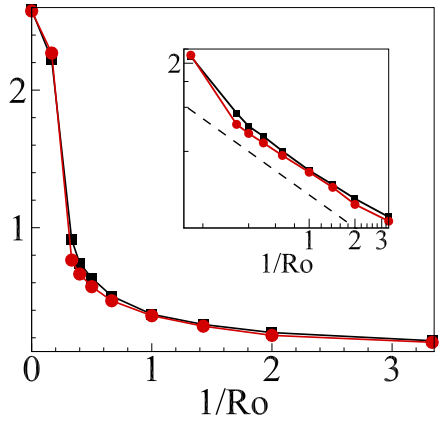

Figure 3.11: Profile of $\tilde{r}_\rho$ as a function of $1/Ro$ at $z = 0.4$ (black squares) and $z = 0.1$ (red circles); the dashed line in the inset denotes the scaling $(1/Ro)^{-3/4}$.

scale, $\ell_0 = \ell_0(z; 1/Ro)$, such that the quantities evaluated at $(\rho + r_\rho/2, \phi, z)$ and $(\rho - r_\rho/2, \phi, z)$ are likely uncorrelated; see also appendix A for further details. In light of this, we can argue that the Coriolis forces may influence the system by reducing the largest length scale at which motion can develop. This behaviour has been somehow anticipated by the qualitative analysis of the flow topology in section 3.1, where the rotation seems to suppress the large-scale circulations that typically emerge in RBC and to reduce the distance between the plumes.

The production Π^u and the relevant transports in physical space, P and I_c^u, reach a well-defined maximum at relatively large separations, namely $r_\rho \approx 2.5$ for $1/Ro = 0$ and $r_\rho \approx 0.3$ for $1/Ro = 1$. According to the interpretation given in section 2.3.2, the coherent structures of size comparable to this characteristic separation are the most responsible for the inhomogeneous mechanisms of production and transport in physical space. In absence of rotation, $r_\rho \approx 2.5$ is roughly the distance between ascending and descending clusters of plumes that lock into large-scale circulations. Such rolls disappear under sufficiently strong rotations and this arguably explains why the characteristic separation observed for $1/Ro = 1$, namely $r_\rho \approx 0.3$, is much smaller than in the non-rotating case and comparable to the distance between individual ascending and descending plumes. The separation that maximizes Π^u,

$$\tilde{r}_\rho = \underset{r_\rho \in [0,4]}{\arg\max}\, \Pi^u,$$

is represented in figure 3.11 as a function of $1/Ro$ and for two distinct locations inside the bulk, namely $z = 0.4$ and $z = 0.1$. As can be seen, $\tilde{r}_\rho$ monotonically decreases as $1/Ro$ increases and this profile does not change across the bulk. Furthermore, the sudden drop observed for $1/Ro > 0.17$ suggests an abrupt cessation of the large-scale circulation and the transition to a column-like pattern of plumes. The plot in logarithmic scale represented in the inset reveals that $\tilde{r}_\rho$ scales as $(1/Ro)^{-3/4}$ for

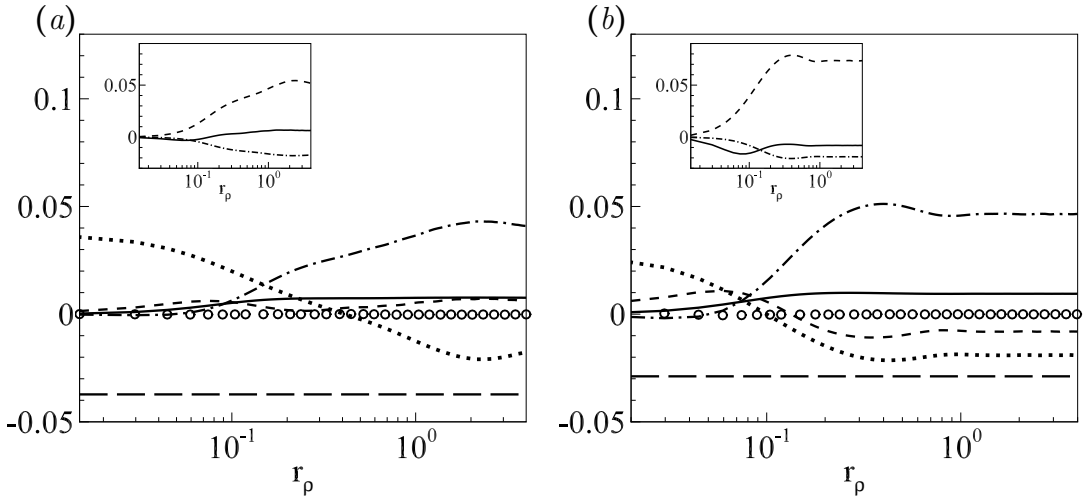

Figure 3.12: As figure 3.10 but inside the transitional layer at $z = 0.02$.

$1/Ro > 0.17$, which corresponds to the theoretical estimation of the average distance between convective structures obtained by Sakai [81], even though this prediction assumes RRBC to be in geostrophic regime. To conclude the analysis inside the bulk, it is worth remarking that the drift of production and transport mechanisms towards smaller dissipative eddies hinders the recovery of an inertial-like range at intermediate scales. Indeed, the inertial transport I_r^u becomes smaller or comparable in magnitude with respect to Π^u and T_c^u at every separation r_ρ when the system spins sufficiently fast.

We proceed by analyzing the reduced Kolmogorov equation inside the transitional layer at $z = 0.02$. Here, the range of turbulent scales is drastically reduced by rotation and the peak of the overall transport in physical space T_c^u moves towards smaller r_ρ, as it occurs with the scale-by-scale dynamics in the bulk region. Although not shown here, the separation that maximizes T_c^u as a function of $1/Ro$ exhibits the same profile of $\tilde{r}_\rho$ in the bulk region. This behaviour can be reasonably explained as follows. The coherent structures that are responsible for producing most of the energy in the core of the flow, namely the rolls for $0 \lesssim 1/Ro \lesssim 0.17$ and the column-like plumes for $1/Ro \gtrsim 0.17$, also carry out the transport of velocity fluctuations towards the wall and release energy into the transitional layer ($T_c^u > 0$) essentially via pressure-velocity correlations ($T_c^u \approx P$). In agreement with the single-point analysis discussed in section 3.2, the energy released into the transitional layer by transport mechanisms increases under rotation. Inside the range $r_\rho \gtrsim 0.15$ and for $1/Ro = 1$, the combined increase of overall transport in physical space and decrease of viscous dissipation results into a reverse energy cascade ($I_r^u < 0$) that cannot be found so close to the wall in absence of rotation. The reverse cascade can be reasonably associated with the splashing of rotating plumes onto the thermal boundary layer, which in turns is responsible for the enhanced extraction of

fluid from the near-wall region. The second aspect that we would like to highlight in the transitional layer is the profile of the inertial transport I_c^u. As can be seen in the inset of figure 3.12(b), I_c^u presents a negative peaked around $r_\rho = 0.08$ which cannot be identified in absence of rotation. Since the maximum Ekman pumping for $1/Ro = 1$ occurs around $z = 0.025$, i.e. very close to the wall-distance considered for the scale-by-scale analysis, we can argue that $r_\rho \approx 0.08$ corresponds to length scale at which most of the fluid extraction occurs. This scale is about one order of magnitude smaller with respect to $\tilde{r}_\rho$, thus it cannot be associated with the diameter of imping plumes but rather with the size of the ejected structures, like the sheet-like roots or the stems of new-born plumes at the intersection spots; see the details of the flow topology in figure 3.1(a-f).

3.5 Summarizing remarks

One of the most relevant aspects that emerges from the study of rotating convection is the presence of two distinct regimes depending on the angular frequency. The gradual change in the flow behavior is evident from both a qualitative and a quantitative point of view. As an example, the weakly rotating regime ($1/Ro \lesssim 0.67$) is characterized by a dense population of slender plumes that rapidly eject from the thermal boundary layer. This flow topology leaves some evident footprints on the statistics and the heat flux enhancement is probably the most fascinating one for the repercussion that may have in technological applications. On the other hand, the rapidly rotating regime ($1/Ro \gtrsim 0.67$) exhibits more but less energetic structures and, in terms of statistics, this behavior brings to a depletion of the heat flux with respect to non-rotating case.

According to the evidences presented in this chapter, the transition from a weakly rotating to a rapidly rotating regime is caused by the crossover between the thermal boundary layer and the location where the maximum Ekman pumping occurs. In case the suction due to spinning plumes takes place outside the thermal boundary layer, the rotation favours the fluid ejection together with the heat transport. However, when the rotation rate surpasses the critical value $1/Ro = 0.67$, the maximum Ekman pumping moves inside the thermal boundary layer and the fluid ejection becomes reasonably less efficient. In this case, the damping of vertical motion that follows the flow bi-dimensionalization overcomes the weak effect of the Ekman pumping and the heat flux steeply decreases towards zero. The novel explanation based on the relative position of thermal boundary layer and maximum Ekman pumping represents, to some extent, a refinement of the theory advanced some years ago by King *et al.* [47], although further studies at different Ra and Pr are certainly required to corroborate our description in a general context.

The structural evolution of the flow is analyzed in more detail in the last part of the chapter, where the reduced Kolmogorov equation is employed to shed light on the scale-by-scale dynamics. Once again, this theoretical approach allows us

to identify some relevant features that elude the classic statistical analysis. These include, for example, the abrupt cessation of the large-scale circulations in presence of rotation and the identification of the characteristic scale of the Ekman pumping. We are confident that these findings may be used in several applications, which range from parametric modelling and LES to flow control techniques.

Chapter 4

Resolved and subgrid dynamics of Rayleigh-Bénard convection

Following the physical understanding gained from chapter 2, this part of the thesis aims at discussing the resolved and the subgrid dynamics of turbulent Rayleigh-Bénard convection (RBC) and presenting a novel approach to model the subgrid dynamics. This study is of particular importance in Large-Eddy Simulation (LES), where a filtering operation is employed to separate the large, energetic scales from the small, dissipative ones, and a model is demanded to reproduce the effect of the residual fields. Within the more general framework of wall-bounded turbulence, the resolved dynamics and the energy transfer between resolved and subgrid scales have been classically addressed in terms of the filtered turbulent kinetic energy budget [38] and energy spectra [31]. Recently, a description using a filtered version of the Kolmogorov equation has been proposed to study the turbulent channel flow [20]. This approach allows to assess the resolved turbulent processes and the subgrid effects at various scales, locations in physical space and for different filter lengths. In this chapter, we extend the filtered multi-scale analysis to thermally driven turbulence by including, for the first time, a filtered version of the Yaglom equation. The results highlight the prominent role of the filter length in comparison with the crossover scales between the inhomogeneous and quasi-homogeneous ranges. From a practical point of view, an appropriate filter length for a LES of RBC is identified together with some guidelines for the subgrid modelling. In the last part, two classic eddy-viscosity/diffusivity models are assessed using *a priori* tests and a new physics-based closure for the subgrid heat flux is derived from the Yaglom equation to overcome the limitations of the existing models.

4.1 Introduction

Thermally driven flows that are relevant in geophysics and technology are still out of reach of DNS due to the huge number of degrees of freedom that need to be solved.

Nonetheless, the steady increase of computational resources during the last decades gave boost to a different approach, the LES, which represents a good compromise between the DNS and the solution of the Reynolds-averaged Navier-Stokes (RANS) equations in terms of accuracy and cost. The basic concept of LES is to solve numerically the large, energy-carrying scales and to model the effect of the small and, arguably, more universal ones. To this end, a low-pass filtering operation is introduced to decompose the velocity and temperature fields into the sum of the filtered (or resolved) components $\bar{u}_i^\star$, $\bar{\theta}^\star$ and the residual (or subgrid) components $u_i^{\star\prime}$, $\theta^{\star\prime}$; see figure 4.1(a,b). The generic filtered and residual variables, $\bar{\beta}$ and β', are formally defined as

$$\bar{\beta}\left(x_i\right) = \int_D \beta\left(\tilde{x}_i\right) G(x_i, \tilde{x}_i; \ell_F) d\tilde{x}_i \quad \text{and} \quad \beta'\left(x_i\right) = \beta\left(x_i\right) - \bar{\beta}\left(x_i\right),$$

where D is the fluid domain, G is the filter function and ℓ_F is the filter width, namely the smallest length scale retained by the filtering operation. The evolution equations for the filtered fields can be obtained by applying the filtering operation to the governing equations. In case of a Boussinesq fluid, which is ruled by (1.1)(a-c), the filtered mass, momentum and temperature balances read as

$$\frac{\partial \bar{u}_i^\star}{\partial x_i} = 0, \tag{4.1a}$$

$$\frac{\partial \bar{u}_i^\star}{\partial t} + \frac{\partial \bar{u}_i^\star \bar{u}_j^\star}{\partial x_j} + \frac{1}{Ro}\epsilon_{i3k}\bar{u}_k^\star = -\frac{\partial \bar{p}^\star}{\partial x_i} + \sqrt{\frac{Pr}{Ra}}\frac{\partial^2 \bar{u}_i^\star}{\partial x_j \partial x_j} + \bar{\theta}^\star \delta_{i3} - \frac{\partial \tau_{ij}^\star}{\partial x_j}, \tag{4.1b}$$

$$\frac{\partial \bar{\theta}^\star}{\partial t} + \frac{\partial \bar{\theta}^\star \bar{u}_i^\star}{\partial x_i} = \frac{1}{\sqrt{PrRa}}\frac{\partial^2 \bar{\theta}^\star}{\partial x_i \partial x_i} - \frac{\partial h_i^\star}{\partial x_i}, \tag{4.1c}$$

where the subgrid-scale (SGS) stress tensor $\tau_{ij}^\star = \overline{u_i^\star u_j^\star} - \bar{u}_i^\star \bar{u}_j^\star$ and the SGS heat flux $h_i^\star = \overline{u_i^\star \theta^\star} - \bar{u}_i^\star \bar{\theta}^\star$ arise from the nonlinear terms in the equations and account for the effect of the subgrid scales on the resolved ones, namely the spatial redistributions of resolved momentum and resolved temperature.

The classical approach followed in LES consists of parameterizing the SGS stresses and heat flux in terms of known quantities, i.e. the filtered variables, and to accurately solve the resulting equations on a relatively coarse mesh, since the the grid spacing can be of the order of the filter length. In this methodology, called *explicit* LES, the filtering and the modelling are disentangled from the numerical method. Indeed, the employed scheme is supposed only to provide an accurate solution of the filtered equations independently from the other conceptual steps [75].

It is generally assumed that LES should satisfy two main requirements in order to accurately reproduce the physics of the flow [71]. First of all, the resolved scales should contain most of the turbulent kinetic energy and temperature variance, generally 80 or 90 per cent of the unfiltered counterparts, whereas subgrid scales should account essentially for dissipation mechanisms [75]. Hence, the filter width needs

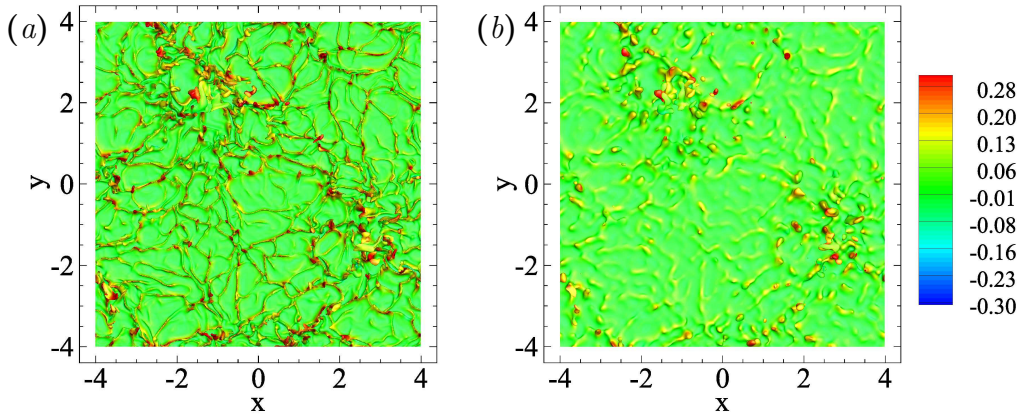

Figure 4.1: Top view of the instantaneous isosurface of temperature (a) $\theta^\star = 0.2$ and (b) $\bar{\theta}^\star = 0.2$ colored by (a) the unfiltered vertical velocity $w^\star$ and by (b) the filtered vertical velocity $\bar{w}^\star$. The data set obtained from DNS 3 ($Ra = 1.0 \times 10^7$) is explicitly filtered using a spectral cutoff along x and y with filter length $\ell_F = 0.13$ or, in wall units, $\ell_F^* = 2.1$.

to be smaller than the local integral scale of the flow, $\ell_0 = \ell_0(x_i)$, in every point of the fluid domain; indeed, the eddies of size about ℓ_0 contribute significatively to the energy and temperature variance as they carry out most of the inhomogeneous productions and transports in physical space. Ideally, the filter width should fall inside a wide inertial range, thus separating the large, energy-containing scales from the small, dissipative ones. The failure to meet this first requirement would arguably provide an inaccurate solutions due to the combined effect of a poorly resolved physics and a larger dependence on the SGS models and their relative imperfections.

In the second instance, the LES models should reproduce correctly the exchange of energy and temperature variance between filtered and residual scales, as it arguably represents the most important effect that needs to be accounted [79, 82]. In this context, most of the LES models assume that the main role of the subgrid scales is to drain energy and temperature variance from the large, resolved ones to dissipate them. This assumption is based on the idea of an inertial range in the spectrum of scales. Indeed, as stated by the 4/5 (2.8) and 4/3 laws (2.9) the fluxes are independent of the scale under consideration throughout the inertial range, are directed from large to small scales in direct cascade processes and they are proportional to the dissipation rates. This picture is claimed to be universal, in the sense that it is independent from the large scales processes that sustain the turbulence.

Historically, the first LES model to be developed for thermally driven turbulence draws inspiration from the scenario above and aims to mimic the direct cascades by means of an eddy-viscosity/diffusivity formulation [53, 86]. In this case, the eddy-viscosity and eddy-diffusivity are simply obtained by invoking an equilibrium assumption (namely, that the small, unresolved scales dissipate entirely and in-

stantaneously all the energy and temperature variance they receive from the large resolved ones) and the model coefficients can be calculated from the Kolmogorov-Obukhov-Corssin spectra by assuming a filter length that falls inside the inertial range [54]. In case of homogeneous and isotropic turbulence transporting a passive temperature, the eddy-viscosity/diffusivity model predicts very well the transfers between resolved and subgrid scales in case the filter width falls inside the inertial range, since it as been designed for this specific case [3]. Furthermore, the first requirement mentioned before is abundantly satisfied, as the energy and temperature spectra are peaked at wavelengths far above the filter width, whereas dissipations mostly occur at the unresolved scales.

The situation changes drastically in case of wall flows, where the classic eddy-viscosity/diffusivity closure does not work properly close to the solid boundaries and empirical tuning of the model coefficients are needed to obtain physically consistent results [30, 62]. Perhaps the most notable example is the product between the Smagorinsky constant, i.e. the classic coefficient of the eddy-viscosity model, and a damping factor depending on the wall-distance, namely the Van Driest damping function [91]. As shown in the previous chapters, the inhomogeneous production and spatial transport affect most of the eddies sufficiently close to the wall and thus hinder the recovery of homogeneous and isotropic turbulence at small scales; see also [2, 41, 25] for a similar behaviour found in other wall-bounded flows. Hence, the equilibrium assumption is openly violated close to the boundaries and the model finds difficult to account for the subgrid dynamics without the aid of specific corrections which, however, deprive the closure of most of its universality.

The correct resolution of the near-wall region represents another important issue in LES of wall-bounded flows since the production and spatial transport mechanisms due to inhomogeneity involve even smaller scales as the boundaries are approached [76]; hence, the local integral scale ℓ_0 steeply decreases from the core towards the wall and such a drop can be of several orders of magnitude in industrial and geophysical flows [72]. Although a proper LES needs to compute all the scales down to the local integral scale in order to resolve most of the turbulent kinetic energy and temperature variance everywhere, this requirement becomes unfeasible for convection at high Rayleigh numbers. If, on the one hand, we should accept to under-resolve the flow boundaries and employ near-wall corrections in most calculations of practical interest, on the other, it is important to understand which turbulent mechanisms are solved and which ones are filtered out by the LES. There are two main reasons for this. Firstly, an overview of the resolved dynamics may lead to the identification of a minimum resolution requirement, i.e. the smallest length scale that we aim to solve explicitly in order to capture the most energetic eddies of the flow [8]. Secondly, the analysis of the subgrid dynamics may give some hints for the development of physics-based SGS models capable to mimic the actual exchange of turbulent fluctuations between resolved and subgrid scales.

Following this line of research, the main purpose of this chapter is to shed some light on the resolved and subgrid dynamics of thermally driven flows via the analysis

of a filtered DNS data set. This approach, called *a priori* in LES studies, can serve as an efficient tool for checking up to what extent the resolved physics reproduces the real one and how the LES model copes with the interplay between resolved and subgrid scales. Due to the inherent complexity of natural and technological flows, we focus our investigation on a simple, canonical system, namely the RBC. Some studies have been devoted to the model assessment of RBC [11, 45, 83, 27], however literature lacks a detailed *a priori* analysis of this system, unlike other paradigms such as the round jet [56], the transitional [73] and the stationary channel flows [38].

A novel theoretical framework for the *a priori* analysis of thermal convection is presented hereafter. An appropriate generalization of the Kolmogorov and Yaglom equations to a filtered case is employed to address the dynamics of resolved and subgrid scales simultaneously in the physical and scale space. The resulting approach allows to evaluate the contributions due to the subgrid terms, at different values of the filter width, for different scales and wall-distances. While the filtered Kolmogorov equation has already been assessed by Cimarelli *et al.* [20] in the case of turbulent channel flow, the filtered Yaglom equation is presented here for the first time. The proposed analysis enables us to appreciate when the SGS stresses and heat flux become relevant for the evolution of resolved velocity and temperature fields. If this is the case, the filtered scale-by-scale budgets reveal the physical nature of these interactions, which should be considered for the correct development of LES models. In this context, the possibility of using the multi-scale description for the development of a new, physics-based closure will be outlined.

The data set used for the analysis comes from the DNS of RBC at $Ra = 1.0 \times 10^7$; see DNS 3 in table 1.1 for further details. The velocity and temperature fields are split into resolved and subgrid components by applying a sharp curoff filter in wavenumber space in each of the wall-parallel directions, x and y, but not in the vertical one, z. Indeed, the wall-normal resolution cannot be reduced such as in the homogeneous directions in near-wall resolved LES; therefore, we expect a prominent role of the horizontal filter length. Let us notice that such a procedure is quite established for the *a priori* analysis of wall-bounded flows [73, 38]. In the present work, we employ a filter length $\ell_F^* = (\pi H) \,/\, (\kappa_c Nu)$ which ranges from 0.7 to 3.1, where κ_c is the cutoff wavenumber. In terms of relative dimensions, the smallest filter length is comparable with the thickness of the thermal boundary layer, whereas the larger one is slightly less than one fourth the height of the fluid layer.

4.2 The filtered Kolmogorov and Yaglom equations

Following the same procedure as in obtaining the Kolmogorov and Yaglom equations for the RBC (see appendix A), two equations for the filtered second-order structure functions $\langle \delta\bar{u}^2 \rangle = \delta\bar{u}_i \delta\bar{u}_i$ and $\left\langle \delta\bar{\theta}^2 \right\rangle = \delta\bar{\theta}\delta\bar{\theta}$ can be derived exactly from the filtered

Boussinesq equations (4.1)(a-c). The filtered Kolmogorov and Yaglom equations, for a generic filtering operation, read as

$$\begin{aligned}
&-\frac{\partial\left\langle\bar{w}^{\dagger}\delta\bar{u}^{2}\right\rangle}{\partial z}-2\frac{\partial\left\langle\delta\bar{p}\delta\bar{w}\right\rangle}{\partial z}+\frac{1}{2}\sqrt{\frac{Pr}{Ra}}\frac{\partial^{2}\left\langle\delta\bar{u}^{2}\right\rangle}{\partial z^{2}}-\frac{1}{r_{\rho}}\frac{\partial}{\partial r_{\rho}}\left(r_{\rho}\left\langle\delta\bar{u}^{2}\delta\bar{u}_{\rho}\right\rangle\right)\\
&-\frac{\partial\left\langle\delta\bar{u}^{2}\delta\bar{w}\right\rangle}{\partial r_{z}}+2\left\langle\delta\bar{\theta}\delta\bar{w}\right\rangle+\frac{2}{r_{\rho}}\sqrt{\frac{Pr}{Ra}}\frac{\partial}{\partial r_{\rho}}\left(r_{\rho}\frac{\partial\left\langle\delta\bar{u}^{2}\right\rangle}{\partial r_{\rho}}\right)+2\sqrt{\frac{Pr}{Ra}}\frac{\partial^{2}\left\langle\delta\bar{u}^{2}\right\rangle}{\partial r_{z}^{2}}\\
&-4\left\langle\bar{\tilde{\epsilon}}^{\dagger}\right\rangle-\frac{\partial\left\langle\delta\tau_{i3}\delta\bar{u}_{i}\right\rangle}{\partial z}-\frac{4}{r_{\rho}}\frac{\partial}{\partial r_{\rho}}\left(r_{\rho}\left\langle\tau_{ij}^{\dagger}\delta\bar{u}_{i}\hat{\rho}_{j}\right\rangle\right)-4\frac{\partial\left\langle\tau_{i3}^{\dagger}\delta\bar{u}_{i}\right\rangle}{\partial r_{z}}\\
&-4\left\langle\epsilon_{sgs}^{\dagger}\right\rangle=0
\end{aligned}\tag{4.2}$$

and

$$\begin{aligned}
&-\frac{\partial\left\langle\bar{w}^{\dagger}\delta\bar{\theta}^{2}\right\rangle}{\partial z}+\frac{1}{2\sqrt{PrRa}}\frac{\partial^{2}\left\langle\delta\bar{\theta}^{2}\right\rangle}{\partial z^{2}}-\frac{1}{r_{\rho}}\frac{\partial}{\partial r_{\rho}}\left(r_{\rho}\left\langle\delta\bar{\theta}^{2}\delta\bar{u}_{\rho}\right\rangle\right)-\frac{\partial\left\langle\delta\bar{\theta}^{2}\delta\bar{w}\right\rangle}{\partial r_{z}}\\
&-2\left\langle\bar{w}^{\dagger}\delta\bar{\theta}\right\rangle\frac{\partial\delta\bar{\Theta}}{\partial z}-2\left\langle\delta\bar{w}\delta\bar{\theta}\right\rangle\left(\frac{d\bar{\Theta}}{dz}\right)^{\dagger}+\frac{2}{r_{\rho}\sqrt{PrRa}}\frac{\partial}{\partial r_{\rho}}\left(r_{\rho}\frac{\partial\left\langle\delta\bar{\theta}^{2}\right\rangle}{\partial r_{\rho}}\right)\\
&+\frac{2}{\sqrt{PrRa}}\frac{\partial^{2}\left\langle\delta\bar{\theta}^{2}\right\rangle}{\partial r_{z}^{2}}-2\left\langle\bar{\chi}^{\dagger}\right\rangle-\frac{\partial\left\langle\delta h_{z}\delta\bar{\theta}\right\rangle}{\partial z}-\frac{4}{r_{\rho}}\frac{\partial}{\partial r_{\rho}}\left(r_{\rho}\left\langle h_{\rho}^{\dagger}\delta\bar{\theta}\right\rangle\right)\\
&-4\frac{\partial\left\langle h_{z}^{\dagger}\delta\bar{\theta}\right\rangle}{\partial r_{z}}-2\left\langle\chi_{sgs}^{\dagger}\right\rangle=0,
\end{aligned}\tag{4.3}$$

where $\bar{u}_i$, $\bar{\theta}$ and $\bar{p}$ are the filtered fluctuating velocity, temperature and pressure fields, τ_{ij} and h_i are the fluctuating SGS stress tensor and heat flux, h_ρ and h_z are the radial and vertical component of the fluctuating SGS heat flux, $\hat{\rho}_j$ is the radial unit vector, $\bar{\tilde{\epsilon}} = \sqrt{Pr/Ra}\,(\partial\bar{u}_i/\partial x_j)\,(\partial\bar{u}_i/\partial x_j)$ is the pseudo-dissipation of resolved turbulent kinetic energy and $\bar{\chi} = 2\,(PrRa)^{-1/2}\left(\partial\bar{\theta}/\partial x_j\right)\left(\partial\bar{\theta}/\partial x_j\right)$ is the dissipation of resolved temperature variance. The rates of turbulent kinetic energy and temperature variance transfers between resolved and subgrid scales, in order $\epsilon_{sgs} = -\tau_{ij}\bar{S}_{ij}$ and $\chi_{sgs} = -2h_i\bar{Q}_i$, are called *subgrid dissipations*, where $\bar{S}_{ij} = 0.5\,(\partial\bar{u}_i/\partial x_j + \partial\bar{u}_j/\partial x_i)$ is the resolved fluctuating strain-rate tensor and $\bar{Q}_i = \partial\bar{\theta}/\partial x_i$ is the resolved fluctuating temperature gradient. Let us point out that, in case of a spectral cutoff filter, the mean profiles remain unaltered, i.e. $\bar{\Theta} = \Theta$.

The analysis of equations (4.2) and (4.3) allow us to evaluate the change in the resolved processes, at different scales and wall-distances, as a function of the filter length and the effect of the SGS stress tensor and the SGS heat flux in the compound physical/scale space domain. The filtering operation introduces three new terms with respect to the unfiltered equations (2.10) and (2.11), namely the

transports in physical space of resolved scale energy and resolved scale variance due to the subgrid scales or, more concisely, the SGS transports in physical space,

$$-\frac{\partial \left\langle \delta\tau_{i3}\delta\bar{u}_i\right\rangle}{\partial z} \quad \text{and} \quad -\frac{\partial \left\langle \delta h_z \delta\bar{\theta}\right\rangle}{\partial z},$$

the SGS transfers in the space of scales,

$$-\frac{4}{r_\rho}\frac{\partial}{\partial r_\rho}\left(r_\rho\left\langle \tau_{ij}^\dagger \delta\bar{u}_i\hat{\rho}_j\right\rangle\right) - 4\frac{\partial\left\langle \tau_{i3}^\dagger\delta\bar{u}_i\right\rangle}{\partial r_z} \quad \text{and} \quad -\frac{4}{r_\rho}\frac{\partial}{\partial r_\rho}\left(r_\rho\left\langle h_\rho^\dagger\delta\bar{\theta}\right\rangle\right) - 4\frac{\partial\left\langle h_z^\dagger\delta\bar{\theta}\right\rangle}{\partial r_z},$$

and the net exchanges between resolved and subgrid scales,

$$-4\left\langle\epsilon_{sgs}^\dagger\right\rangle \quad \text{and} \quad -2\left\langle\chi_{sgs}^\dagger\right\rangle.$$

Equations (4.2) and (4.3) are written in the complete physical/scale space domain (r_ρ, r_z, z) and parameterized by the filter length ℓ_F. To simplify the analysis, we lower the dimensionality of the filtered budgets by considering a reduced (r_ρ, z)-space for $r_z = 0$. The resulting *reduced* filtered Kolmogorov and Yaglom equations read as

$$\bar{T}_c^u + \bar{I}_r^u + \bar{\Pi}^u + \bar{E}_e^u + T_{c,sgs}^u + T_{r,sgs}^u + E_{sgs}^u = 0, \tag{4.4}$$

$$\bar{T}_c^\theta + \bar{I}_r^\theta + \bar{\Pi}^\theta + \bar{E}_e^\theta + T_{c,sgs}^\theta + T_{r,sgs}^\theta + E_{sgs}^\theta = 0, \tag{4.5}$$

where $\bar{T}_c^u = \bar{I}_c^u + \bar{P} + \bar{D}_c^u$, $\bar{T}_c^\theta = \bar{I}_c^\theta + \bar{D}_c^\theta$ are the overall resolved transports in physical space and $\bar{E}_e^u = \bar{D}_r^u + \bar{E}^u$, $\bar{E}_e^\theta = \bar{D}_r^\theta + \bar{E}^\theta$ are the effective resolved dissipations. The different contributions to the overall resolved transports and effective resolved dissipations are, in order,

$$\bar{I}_c^u = -\frac{\partial\left\langle\bar{w}^\dagger\delta\bar{u}^2\right\rangle}{\partial z},\ \bar{P} = -2\frac{\partial\left\langle\delta\bar{p}\delta\bar{w}\right\rangle}{\partial z},\ \bar{D}_c^u = \frac{1}{2}\sqrt{\frac{Pr}{Ra}}\frac{\partial^2\left\langle\delta\bar{u}^2\right\rangle}{\partial z^2},$$

$$\bar{I}_c^\theta = -\frac{\partial\left\langle\bar{w}^\dagger\delta\bar{\theta}^2\right\rangle}{\partial z},\ \bar{D}_c^\theta = \frac{1}{2\sqrt{PrRa}}\frac{\partial^2\left\langle\delta\bar{\theta}^2\right\rangle}{\partial z^2},$$

and

$$\bar{D}_r^u = \frac{2}{r_\rho}\sqrt{\frac{Pr}{Ra}}\frac{\partial}{\partial r_\rho}\left(r_\rho\frac{\partial\left\langle\delta\bar{u}^2\right\rangle}{\partial r_\rho}\right) + 2\sqrt{\frac{Pr}{Ra}}\frac{\partial^2\left\langle\delta\bar{u}^2\right\rangle}{\partial r_z^2}\Big|_{r_z=0},\ \bar{E}^u = -4\left\langle\bar{\tilde{\epsilon}}\right\rangle,$$

$$\bar{D}_r^\theta = \frac{2}{r_\rho\sqrt{PrRa}}\frac{\partial}{\partial r_\rho}\left(r_\rho\frac{\partial\left\langle\delta\bar{\theta}^2\right\rangle}{\partial r_\rho}\right) + \frac{2}{\sqrt{PrRa}}\frac{\partial^2\left\langle\delta\bar{\theta}^2\right\rangle}{\partial r_z^2}\Big|_{r_z=0},\ \bar{E}^\theta = -2\left\langle\bar{\chi}\right\rangle,$$

whereas the resolved transfers in the space of scales and the resolved productions are

$$\bar{I}_r^u = -\frac{1}{r_\rho}\frac{\partial}{\partial r_\rho}\left(r_\rho\left\langle\delta\bar{u}^2\delta\bar{u}_\rho\right\rangle\right) - \frac{\partial\left\langle\delta\bar{u}^2\delta\bar{w}\right\rangle}{\partial r_z}\Big|_{r_z=0},\ \bar{\Pi}^u = 2\left\langle\delta\bar{\theta}\delta\bar{w}\right\rangle,$$

$$\bar{I}_r^\theta = -\frac{1}{r_\rho}\frac{\partial}{\partial r_\rho}\left(r_\rho\left\langle\delta\bar{\theta}^2\delta\bar{u}_\rho\right\rangle\right) - \frac{\partial\left\langle\delta\bar{\theta}^2\delta\bar{w}\right\rangle}{\partial r_z}\Big|_{r_z=0} \quad \text{and} \quad \bar{\Pi}^\theta = -2\left\langle\delta\bar{w}\delta\bar{\theta}\right\rangle\frac{d\bar{\Theta}}{dz},$$

where $\beta^\dagger = \beta$ and the contribution of $-2\left\langle \bar{w}^\dagger \delta\bar{\theta}\right\rangle \partial\delta\bar{\Theta}/\partial z$ to the resolved production is equal to zero, as $\delta\bar{\Theta} = 0$ for $r_z = 0$. Finally, the SGS transports in physical space, the SGS transfers in the space of scales and the subgrid dissipation terms are, in order,

$$T^u_{c,sgs} = -\frac{\partial\left\langle \delta\tau_{i3}\delta\bar{u}_i\right\rangle}{\partial z},\ T^\theta_{c,sgs} = -\frac{\partial\left\langle \delta h_z \delta\bar{\theta}\right\rangle}{\partial z},$$

$$T^u_{r,sgs} = -\frac{4}{r_\rho}\frac{\partial}{\partial r_\rho}\left(r_\rho\left\langle \tau_{ij}\delta\bar{u}_i\hat{\rho}_j\right\rangle\right) - 4\frac{\partial\left\langle \tau_{i3}\delta\bar{u}_i\right\rangle}{\partial r_z}\Big|_{r_z=0},$$

$$T^\theta_{r,sgs} = -\frac{4}{r_\rho}\frac{\partial}{\partial r_\rho}\left(r_\rho\left\langle h_\rho\delta\bar{\theta}\right\rangle\right) - 4\frac{\partial\left\langle h_z\delta\bar{\theta}\right\rangle}{\partial r_z}\Big|_{r_z=0},$$

and

$$E^u_{sgs} = -4\left\langle \epsilon_{sgs}\right\rangle,\ E^\theta_{sgs} = -2\left\langle \chi_{sgs}\right\rangle.$$

Analogously to the reduced Kolmogorov and Yaglom equations, (4.4) and (4.5) manifest a well-defined asymptotic behaviour as larger separations are approached. For $r_\rho \gg \ell_0$, where $\ell_0 = \ell_0(z)$ is the local integral scale, quantities evaluated at $(\rho + r_\rho/2, \phi, z)$ and $(\rho - r_\rho/2, \phi, z)$ are uncorrelated; thus (4.4) and (4.5) converge, respectively, to four-times the budget of resolved turbulent kinetic energy and two-times the budget of resolved temperature variance,

$$4(\bar{t}^u_c + \bar{\pi}^u - \langle\bar{\tilde{\epsilon}}\rangle + t^u_{c,sgs} - \langle\epsilon_{sgs}\rangle) = 0, \tag{4.6}$$

$$2(\bar{t}^\theta_c + \bar{\pi}^\theta - \langle\bar{\chi}\rangle + t^\theta_{c,sgs} - \langle\chi_{sgs}\rangle) = 0, \tag{4.7}$$

where

$$\bar{t}^u_c = -\frac{d\left\langle \bar{k}\bar{w}\right\rangle}{dz} - \frac{d\left\langle \bar{w}\bar{p}\right\rangle}{dz} + \sqrt{\frac{Pr}{Ra}}\frac{d^2\left\langle \bar{k}\right\rangle}{dz^2},\ \bar{\pi}^u = \left\langle \bar{w}\bar{\theta}\right\rangle,$$

$$\bar{t}^\theta_c = -\frac{d\left\langle \bar{\theta}^2\bar{w}\right\rangle}{dz} + \frac{1}{\sqrt{PrRa}}\frac{d^2\left\langle \bar{\theta}^2\right\rangle}{dz^2},\ \bar{\pi}^\theta = -2\left\langle \bar{w}\bar{\theta}\right\rangle\frac{d\bar{\Theta}}{dz},$$

are the overall transports along z and productions of $\left\langle \bar{k}\right\rangle = \langle 0.5\bar{u}_i\bar{u}_i\rangle$ and $\left\langle \bar{\theta}^2\right\rangle$. The SGS transports read as

$$t^u_{c,sgs} = -\frac{d\left\langle \tau_{i3}\bar{u}_i\right\rangle}{dz} \quad \text{and} \quad t^\theta_{c,sgs} = -2\frac{d\left\langle h_z\bar{\theta}\right\rangle}{dz},$$

where the terms of the scale-by-scale budgets $T^u_{c,sgs}$ ($T^\theta_{c,sgs}$) and $T^u_{r,sgs}$ ($T^\theta_{r,sgs}$) approach the same value for $r_\rho \gg \ell_0$, i.e. half of $t^u_{c,sgs}$ ($t^\theta_{c,sgs}$).

By considering a spectral cutoff filter, it is possible to decompose the scale energy and the scale variance into a resolved component and a subgrid component, namely $\langle\delta u^2\rangle = \langle\delta\bar{u}_i\delta\bar{u}_i\rangle + \langle\delta u'_i\delta u'_i\rangle$ and $\langle\delta\theta^2\rangle = \left\langle\delta\bar{\theta}\delta\bar{\theta}\right\rangle + \langle\delta\theta'\delta\theta'\rangle$, where u' and θ' are the residual fluctuating velocity and temperature fields. The budgets of subgrid scale energy and subgrid scale variance can be written in the compact forms

$$T^{u\prime}_c + I^{u\prime}_r + \Pi^{u\prime} + E^{u\prime}_e - T^u_{c,sgs} - T^u_{r,sgs} - E^u_{sgs} = 0, \tag{4.8}$$

$$T_c^{\theta\prime} + I_r^{\theta\prime} + \Pi^{\theta\prime} + E_e^{\theta\prime} - T_{c,sgs}^{\theta} - T_{r,sgs}^{\theta} - E_{sgs}^{\theta} = 0. \tag{4.9}$$

It has been proved that for r_ρ slightly larger than ℓ_F, the subgrid velocity and temperature evaluated at $(\rho + r_\rho/2, \phi, z)$ are fairly uncorrelated with the corresponding ones at $(\rho - r_\rho/2, \phi, z)$, thus the scale-by-scale budgets (4.8) and (4.9) converge, in order, to four-times the single-point budget of subgrid turbulent kinetic energy $\langle k' \rangle = 0.5 \langle u_i' u_i' \rangle$ and two-times the single-point budget of subgrid temperature variance $\langle \theta'^2 \rangle$

$$4(t_c^{u\prime} + \pi^{u\prime} - \langle \tilde{\epsilon}' \rangle - t_{c,sgs}^{u} + \langle \epsilon_{sgs} \rangle) = 0, \tag{4.10}$$

$$2(t_c^{\theta\prime} + \pi^{\theta\prime} - \langle \chi' \rangle - t_{c,sgs}^{\theta} + \langle \chi_{sgs} \rangle) = 0, \tag{4.11}$$

where the terms denoted with the prime symbol and the corresponding ones with the overbar symbol in (4.6) and (4.7) are identical except for the replacement of the filtered velocity, temperature and pressure fields with the residual counterparts.

We conclude this section by remarking that the filtered (reduced) Kolmogorov and Yaglom equations converge to the unfiltered (reduced) Kolmogorov and Yaglom equations when $\ell_F \to 0$, and so do the filtered single-point budgets, which approach the unfiltered counterparts.

4.3 Study of the filtered data set

In this section, we present a detailed analysis of the filtered dynamics of RBC using the filtered single-point budgets, (4.6) and (4.7), and their multi-scale generalization, namely the filtered reduced Kolmogorov and Yaglom equations, (4.4) and (4.5). The resolved processes will be thoroughly discussed and emphasis will be put on the effect of τ_{ij} and h_i both in physical and scale space. The filter lengths employed for this study are compared with the characteristic scales of RBC identified in §2.3.4 and reported in figure 4.2(a,b) for $Ra = 1.0 \times 10^7$. These are the crossovers ℓ_c^{u*} and $\ell_c^{\theta*}$, which divide the large, inhomogeneous scales from the small, quasi-homogeneous ones, and the boundaries ℓ_b^{u*} and $\ell_b^{\theta*}$, which separate direct and reverse cascades.

The value of the filter length with respect to the crossover scales specifies which turbulent mechanisms can be solved directly by LES and which processes are filtered out and thus can only be modelled. A near-wall resolved LES has to capture most of the inhomogeneous, energy-containing scales everywhere in the domain; therefore, a filter length should be employed that is smaller than the minimum crossover scale of our flow, namely $\ell_{c,min}^{\theta*}$. Here, it should be remarked that such a resolution constraint does not depend on the Rayleigh number, since the profile of $\ell_c^{\theta*}$ has been proved to be Ra-invariant and $\ell_c^{\theta*} < \ell_c^{u*}$ at every wall-distance, at least for $Pr = 0.7$ and possibly also for larger Pr. The minimum resolution requirement can be estimated *a priori* for different Rayleigh numbers and for a fixed Prandtl, as long as an estimation of the Nusselt number is available. Indeed, $\ell_{c,min}^{\theta*} = \ell_{c,min}^{\theta} Nu = const$, thus the adequate grid spacing $\Delta \approx \ell_F$ employed by the LES should not be larger than $\ell_{c,min}^{\theta} = const/Nu$.

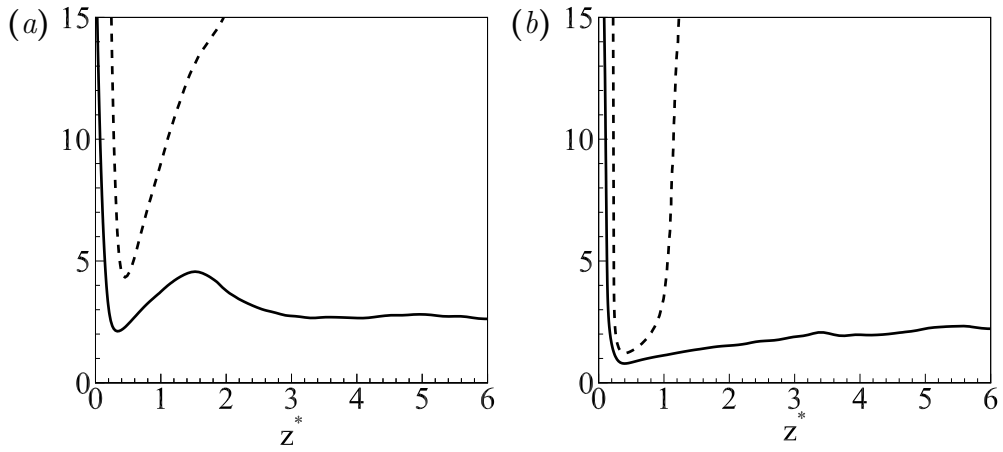

Figure 4.2: (a) Velocity crossover scale ℓ_c^{u*} (solid lines) and boundary scale ℓ_b^{u*} (dashed lines), (b) temperature crossover scale $\ell_c^{\theta*}$ (solid lines) and boundary scale $\ell_b^{\theta*}$ (dashed lines) for $Ra = 1.0 \times 10^7$.

The mechanisms that are not resolved for $\ell_F^* < \ell_{c,min}^\theta$ are essentially the dissipations of turbulent kinetic energy and temperature variance; therefore, classic eddy-viscosity/diffusivity may provide a good estimation of the transfers between resolved and subgrid scales. In case $\ell_F^* > \ell_{c,min}^\theta$, also the inhomogeneous mechanisms are poorly resolved and the SGS fields include highly dynamic eddies that contribute a significant portion of the production and transport besides dissipation, which may bring to some modelling issues. Indeed, eddy-viscosity/diffusivity models cannot account for the inhomogeneous mechanisms occurring at subgrid level, thus the exchanges between resolved and subgrid scales can hardly be copied. Furthermore, an increase of the filter length beyond the boundary scale ℓ_b^{u*} ($\ell_b^{\theta*}$) may bring to a net flux of energy (temperature variance) from the subgrid scales to the resolved ones, i.e. to a negative value of the average subgrid dissipation $\langle \epsilon_{sgs} \rangle$ ($\langle \chi_{sgs} \rangle$). This phenomenon has been observed in the early stages of transitional channel flow [74] and, in some cases, in fully-developed turbulent channel flow [38, 20], but no evidences exists for turbulent RBC. Since the eddy-viscosity/diffusivity models are designed to be purely dissipative to avoid numerical instabilities, i.e. the modeled subgrid dissipations are always positive, they cannot account for an average reverse transfers and thus different formulations should be considered (e.g. the mixed model formulation, see Vreman *et al.*[95] for a detailed overview).

4.3.1 Analysis of the filtered single-point budgets

In this section, we discuss the single-point analysis of the filtered turbulent kinetic energy and temperature variance budgets, in order (4.6) and (4.7). These equations, to the authors knowledge, have never been completely analyzed for the RBC case,

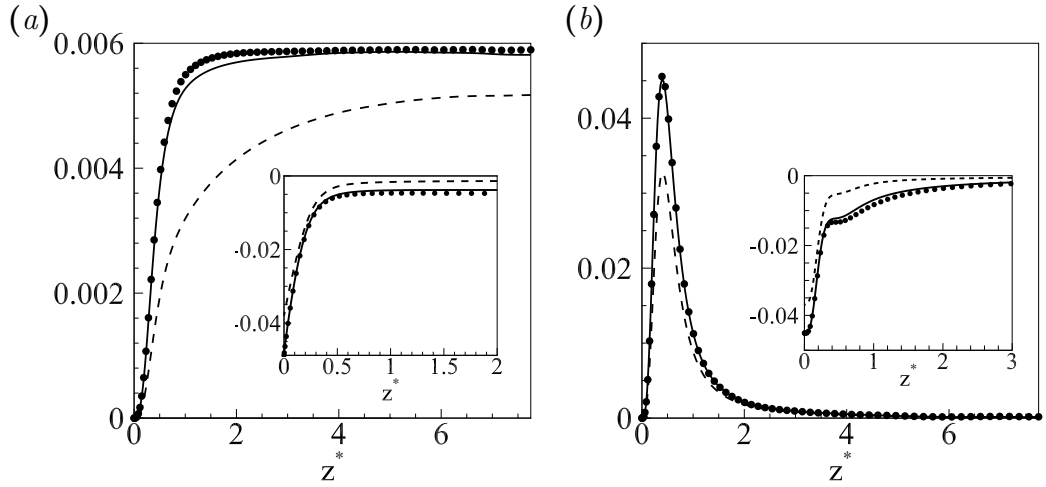

Figure 4.3: Main figure: unfiltered and resolved production of (a) turbulent kinetic energy (circles for the unfiltered case, solid line for $\ell_F^* = 1.0$ and dashed line for $\ell_F^* = 3.1$) and (b) temperature variance (circles for the unfiltered case, solid line for $\ell_F^* = 0.7$ and dashed line for $\ell_F^* = 2.1$). Insets: unfiltered and resolved (a) pseudo-dissipation of turbulent kinetic energy and (b) dissipation of temperature variance for the same filter lengths of the corresponding main plots.

thus this part aims to present some results that are both novel and preparatory to the multi-scale analysis of the filtered reduced Kolmogorov and Yaglom equations presented in sections 4.3.2 and 4.3.3 respectively.

The production of resolved turbulent kinetic energy and temperature variance, $\bar{\pi}^u$ and $\bar{\pi}^\theta$, are displayed in the main plots of figure 4.3(a,b) for two significant filter lengths and together with their unfiltered counterparts, $\pi^u = \langle w\theta \rangle$ and $\pi^\theta = -2\langle w\theta \rangle d\Theta/dz$. It can be seen that the depletions of $\bar{\pi}^u$ and $\bar{\pi}^\theta$ with respect to π^u and π^θ are rather small if the filter length is within the quasi-homogeneous range, namely $\ell_F^* < \ell_{c,min}^{u*} \approx 2.1$ and $\ell_F^* < \ell_{c,min}^{\theta*} \approx 0.8$, whereas they become important in case the filter length exceeds the minimum crossover scales and enters the inhomogeneous range. Although only two filter lengths are shown here, it is worth remarking that the depletion of production does not increase linearly with ℓ_F^*; indeed, an increase of the depletion rate is observed for $\ell_F^* > \ell_{c,min}^{u*}$ and $\ell_F^* > \ell_{c,min}^{\theta*}$ and this behaviour strengthens the role of ℓ_c^{u*} and $\ell_c^{\theta*}$ as physically relevant scales in RBC. The differences between resolved and unfiltered productions, $\pi^u - \bar{\pi}^u$ and $\pi^\theta - \bar{\pi}^\theta$, are maxima around $z^* = 1$ and $z^* = 0.5$ respectively. This behaviour can be explained by considering that the small scales, which are filtered out, produce mainly in the transitional layer and low bulk region rather than in other locations; see for example figures 2.9(a,b) and 2.12(a,b). Therefore, the depletion that follows the filtering operation is arguably more intense there than anywhere else.

The insets of figure 4.3(a,b) display the average pseudo-dissipation of resolved turbulent kinetic energy, $\langle \bar{\tilde{\epsilon}} \rangle$, and the average dissipation of resolved temperature

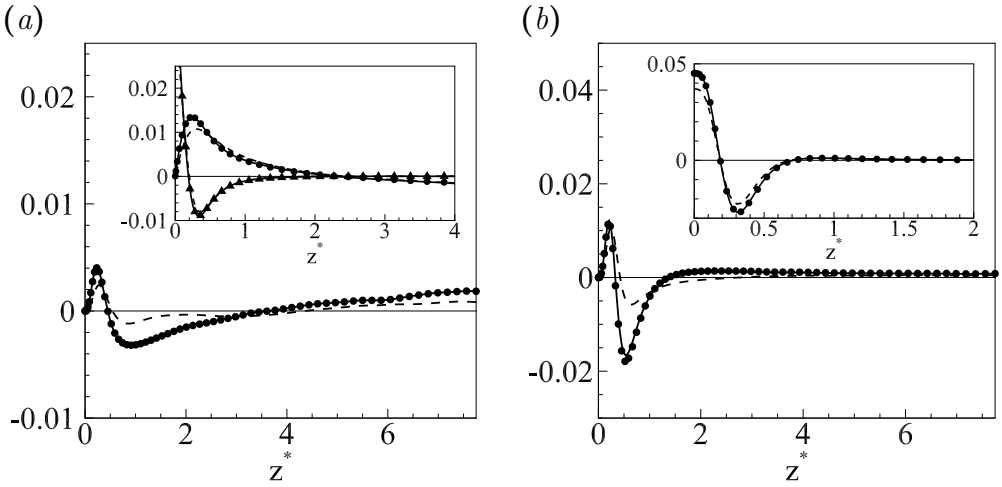

Figure 4.4: Main figure: unfiltered and resolved inertial transport of (a) turbulent kinetic energy (circles for the unfiltered case, solid line for $\ell_F^* = 1.0$ and dashed line for $\ell_F^* = 3.1$) and (b) temperature variance (circles for the unfiltered case, solid line for $\ell_F^* = 0.7$ and dashed line for $\ell_F^* = 2.1$). Insets: unfiltered and resolved (a) viscous and pressure transport of turbulent kinetic energy and (b) diffusive transport of temperature variance for the same filter lengths of the corresponding main plots.

variance, $\langle\bar{\chi}\rangle$, for the same filter lengths of the main plots and together with their fully-resolved counterparts, $\langle\tilde{\epsilon}\rangle$ and $\langle\chi\rangle$. The resolved dissipations decrease in magnitude as larger filter lengths are considered and, for $\ell_F^* > \ell_{c,min}^{u*}$ and $\ell_F^* > \ell_{c,min}^{\theta*}$, they become much smaller than the unfiltered counterparts inside the core of the flow, that is to say, the subgrid scales are the main responsible for dissipative mechanisms away from the boundaries. In the near-wall region, on the other hand, the resolved scales contribute substantially to the dissipation also at large filter lengths, as the ratios $\langle\bar{\tilde{\epsilon}}\rangle / \langle\tilde{\epsilon}\rangle$ and $\langle\bar{\chi}\rangle / \langle\chi\rangle$ have been found to increase monotonically when the wall is approached.

The inertial, pressure and viscous transports of $\langle\bar{k}\rangle$ and the inertial and diffusive transports of $\langle\bar{\theta}^2\rangle$ are plotted in figure 4.4(a,b). The resolved transports overlap the unfiltered ones for $\ell_F^* < \ell_{c,min}^{u*}$ and $\ell_F^* < \ell_{c,min}^{\theta*}$, whereas they do not match each other when larger ℓ_F^* are considered. The filtering operation seems to affect the inertial transports rather than the viscous/diffusive and pressure ones. In particular, the magnitudes of the inertial transports deplete mainly inside the transitional layer and low bulk region, where turbulent velocity and temperature fluctuations are transported away ($-d\langle\bar{k}\bar{w}\rangle/dz < 0$ and $-d\langle\bar{\theta}^2\bar{w}\rangle/dz < 0$) to sustain the remaining parts of the flow ($-d\langle\bar{k}\bar{w}\rangle/dz > 0$ and $-d\langle\bar{\theta}^2\bar{w}\rangle/dz > 0$). Once again, this behaviour can be explained by considering that most of the inertial transport from the transitional layer and low bulk region towards the center and the walls occurs at small, filtered-out scales. From the point of view of the flow topology, this seems to be related to the difficulty encountered by large filters in capturing the thermal

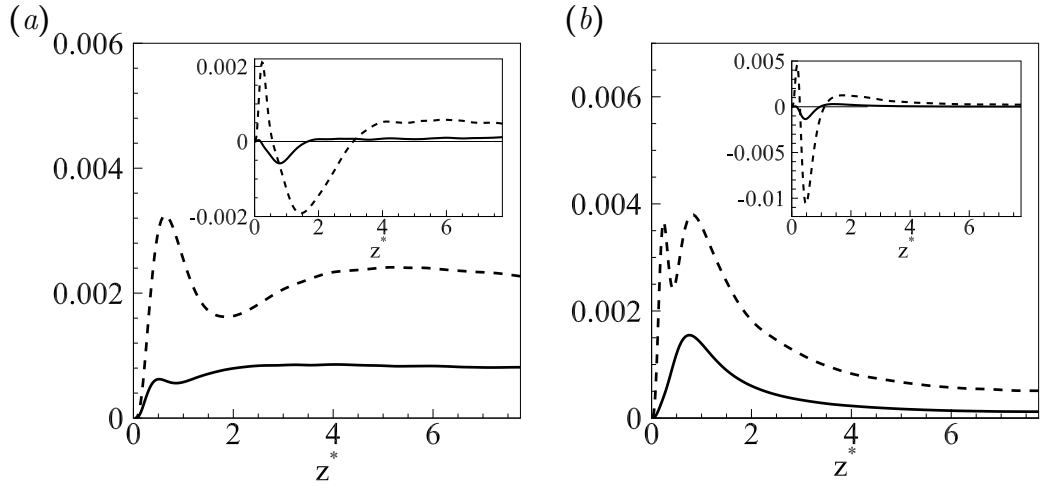

Figure 4.5: Main figure: profiles of the average subgrid dissipations, (a) $\langle \epsilon_{sgs} \rangle$ and (b) $\langle \chi_{sgs} \rangle$, as a function of z^*, for $\ell_F^* = 1.0$ (solid line) and $\ell_F^* = 3.1$ (dashed line). Inset: profiles of the SGS transports, (a) $t_{c,sgs}^u$ and (b) $t_{c,sgs}^\theta$, as a function of z^*, for $\ell_F^* = 0.7$ (solid line) and $\ell_F^* = 2.1$ (dashed line).

plumes. Indeed, the diameter of these structures, δ_p, is assumed to be of the order of the thermal boundary layer thickness, i.e. $\delta_p^* \approx 0.5$. As can be seen in figure 4.1(a,b), by filtering out the scales smaller than $\ell_F^* = 2.1$ or $\ell_F^* = 3.1$, we delete most of the coherent modes responsible for the advection of turbulent kinetic energy and temperature variance; hence, a consistent depletion of the inertial transports could be somehow expected.

The average subgrid dissipations $\langle \epsilon_{sgs} \rangle$ and $\langle \chi_{sgs} \rangle$ are represented in the main plots of figure 4.5(a,b). Both terms are non-negative at every distance from the wall and for all the filter lengths considered in this study. The subgrid scales are, on average, sinks of turbulent fluctuations even when the filter length overcomes the minimum boundary scales $\ell_{b,min}^{u*}$ and $\ell_{b,min}^{\theta*}$, although we observe that $\langle \epsilon_{sgs} \rangle$ and $\langle \chi_{sgs} \rangle$ start to decrease after the thresholds. The shape of the profiles depends on the filter length and the change is more evident for $\langle \chi_{sgs} \rangle$, as a local minimum appears around $z^* = 0.5$. Here, it should be mentioned that, to our knowledge, the only *a priori* calculation of subgrid dissipations in RBC has been presented by Kimmel *et al.* [45] for $Ra = 6.3 \times 10^5$, showing a reasonable agreement with the preset results.

We conclude the single-point analysis by considering the SGS transports $t_{c,sgs}^u$ and $t_{c,sgs}^\theta$ plotted in the insets of figure 4.5(a,b). As could be expected, these terms are rather negligible for small filter lengths, whereas they become relevant for $\ell_F^* > \ell_{c,min}^{u*}$ and $\ell_F^* > \ell_{c,min}^{\theta*}$. In the latter case, the SGS transports and the corresponding inertial transports have similar profiles, that is to say, the subgrid scales, apart from draining the resolved ones, as $\langle \epsilon_{sgs} \rangle < 0$ and $\langle \chi_{sgs} \rangle < 0$, redistribute energy and temperature variance within the fluid domain. It can be seen by comparing the main plots in figure 4.4(a,b) with the insets in 4.5(a,b) that the resolved inertial transports

and the SGS transports are fairly comparable in magnitude inside the transitional layer and low bulk region, meaning that the nonlinear triadic interactions between resolved and subgrid scales are as much important as the ones between resolved scales. Loosely speaking, this might be related to the coupling between a hierarchy of structures living at subgrid level, i.e. the thermal plumes, and the large-scale circulations which are always captured by the filtering operation, as can be seen in figure 4.1(a,b).

4.3.2 Analysis of the filtered reduced Kolmogorov equation

In this section, the filtered reduced Kolmogorov equation (4.4) is analyzed for two distinct locations in physical space, inside the bulk region at $z^* = 3$ and inside the transitional layer at $z^* = 0.7$, and for two relevant filter lengths, $\ell_F^* = 1.0$ and $\ell_F^* = 3.1$, which are smaller and larger than the minimum crossover scale for the velocity field, $\ell_{c,min}^{u*} \approx 2.1$.

Figure 4.6(a) represents the scale-by-scale budget inside the bulk region and for $\ell_F^* = 1.0$. As indicated by the overlapping between the resolved terms, $\bar{\Pi}^u$ and $\bar{T}_c^u$, and the unfiltered ones, Π^u and T_c^u, the mechanisms of production and transport in physical space are captured very well by the filtered fields. This behaviour has been observed at every wall-distance (see, for example, figure 4.6(b) for $z = 0.7$) and agrees with the choice of a filter length within the quasi-homogeneous range, where the direct cascade towards dissipation is dominant with respect to the net source/drain of energy due to the inhomogeneous production and overall transport in physical space. Under this condition, the viscous dissipation is the only physical phenomenon that is filtered out, as suggested by the clear depletion of the resolved effective dissipation with respect to the unfiltered one, i.e. $|\bar{E}_e^u| < |E_e^u|$. Hence, the only role of the subgrid scales is to drain the amount of energy that is not dissipated by the resolved motion, that is to say, $E_{sgs}^u < 0$ and $\bar{E}_e^u + E_{sgs}^u \approx E_e^u$; accordingly, the transports of resolved energy in physical space and scale space due to the subgrid scales are negligible ($T_{c,sgs}^u \approx 0$ and $T_{r,sgs}^u \approx 0$).

The resolved dynamics changes substantially for $\ell_F^* > \ell_{c,min}^{u*}$. Figure 4.7($a$) displays the scale-by-scale budget in the bulk for $\ell_F^* = 3.1$. As the filter length is larger than the minimum crossover scale, we expect a depletion of the net contribution of resolved production and resolved transport in physical space, i.e. $\bar{\Pi}^u + \bar{T}_c^u < \Pi^u + T_c^u$, in agreement with the definition of the crossover scale in (2.14). Figure 4.7(a) confirms the expectation and shows that the depletion is attributable only to the resolved production since $\bar{\Pi}^u < \Pi^u$ and $\bar{T}_c^u \approx T_c^u$. Moreover, the energy cascade is almost unaltered by the filtering operation ($\bar{I}_r^u \approx I_r^u$) whereas the effective dissipation is drastically reduced ($|\bar{E}_e^u| \ll |E_e^u|$). Contrary to the previous case for $\ell_F^* < \ell_{c,min}^{u*}$, the effects of the SGS stresses on the resolved motion cannot be ascribed only to the dissipative mechanisms acting at subgrid level. Indeed, the net energy exchange between resolved and subgrid scales, E_{sgs}^u, is not set by the dissipation alone but also by a non-negligible, unresolved production. The balance between production

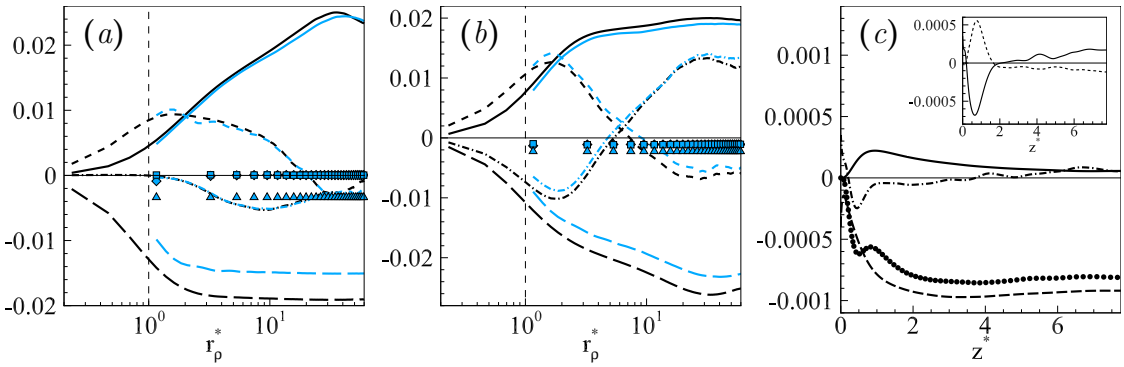

Figure 4.6: Scale-by-scale budgets (2.12) and (4.4) at (a) $z^* = 3$ and (b) $z^* = 0.7$ for $\ell^*_F = 1.0$. The plotted terms are the productions Π^u and $\bar{\Pi}^u$ (solid line), the overall transports in physical space T^u_c and $\bar{T}^u_c$ (dot-dashed line), the transfers in the space of scales I^u_r and $\bar{I}^u_r$ (dashed line), the effective dissipations E^u_e and $\bar{E}^u_e$ (long-dashed line), and the SGS terms $T^u_{c,sgs}$ (square), $T^u_{r,sgs}$ (diamond) and E^u_{sgs} (triangle); the quantities of the unfiltered budget (2.12) are represented in black, the others in blue. The vertical dashed lines denotes ℓ^*_F. (c) Main plot: behaviour of $-\langle\epsilon_{sgs}\rangle$ (circles), $-\langle\tilde{\epsilon}'\rangle$ (long-dashed line), $t^{u\prime}_c - t^u_{c,sgs}$ (dot-dashed line) and $\pi^{u\prime}$ (solid line) as a function of z^* and for $\ell^*_F = 1.0$. Inset: profiles of $t^{u\prime}_c$ (solid line) and $-t^u_{c,sgs}$ (dashed line).

and dissipation at subgrid scales does not allow for the recovery of the unfiltered dissipation, i.e. $|\bar{E}^u + E^u_{sgs}| \approx |E^u|$, but rather $|\bar{E}^u + E^u_{sgs}| \ll |E^u|$, as can be clearly seen in the figure. Finally, the redistributions of resolved energy in the compound physical/scale space domain due to SGS stresses is found to be negligible in this region of the flow ($T^u_{c,sgs} \approx 0$ and $T^u_{r,sgs} \approx 0$).

We still observe an erosion of the real physics closer to the wall (see figure 4.7(b) for $z^* = 0.7$); however, contrary to the bulk, not only a depletion of the resolved production is observed here ($\bar{\Pi}^u \ll \Pi^u$) but also a modification of the resolved transports in physical and scale space becomes evident. In particular, we observe that the reverse energy cascade at large scales ($I^u_r < 0$) is not resolved as $\bar{I}^u_r \approx 0$, whereas the forward cascade at small scales ($I^u_r > 0$) is copied rather well. This aspect suggests that the reverse cascade is nonlocal in the space of scales, in the sense that filtering out the small eddies drastically affects also the energy transfer at large scales. Another interesting behavior is that the resolved transport in physical space increases with respect to the unfiltered counterpart, becoming positive for $r^*_\rho > \ell^*_F$. This can be explained by recalling the double feature of T^u_c in the transitional layer, which has been previously discussed in section 2.3.2. In brief, the large scales gain energy from the spatial flux ($T^u_c < 0$) whereas the small ones feed the flux towards the wall ($T^u_c > 0$); that said, the main contribution to $\bar{T}^u_c$ comes from eddies transporting energy into the transitional layer, thus we would

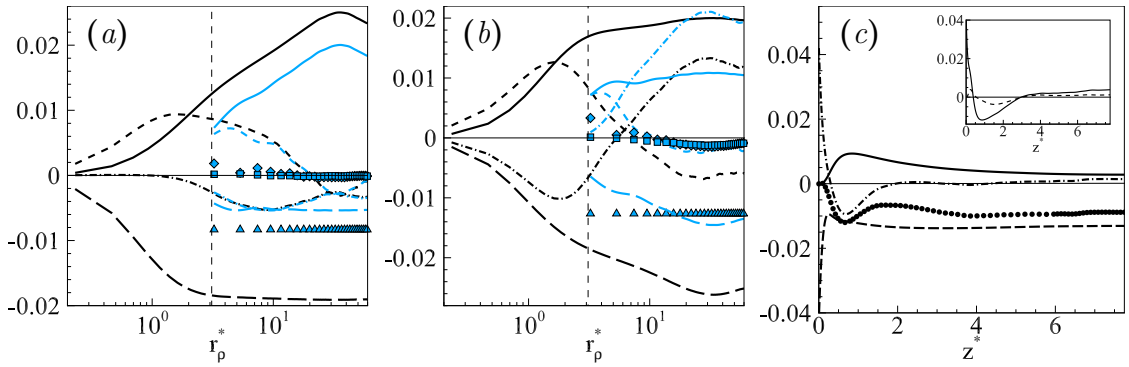

Figure 4.7: As figure 4.6 but for $\ell_F^* = 3.1$.

expect $\bar{T}_c^u$ to be positive and larger than T_c^u . Regarding the effects of the SGS stresses on the resolved dynamics, the average subgrid dissipation is negative as in the bulk region; however, it seems here to account only for the missed dissipation occurring at small scales, as $\bar{E}_e^u + E_{sgs}^u \approx E_e^u$. Furthermore, contrary to what occurs in the bulk, the SGS stresses contribute actively to redistribute the resolved energy both in physical and scale space, since $T_{c,sgs}^u$ and $T_{r,sgs}^u$ are different from zero.

To explain the non-trivial behaviour of the average subgrid dissipation, we analyze the subgrid turbulent kinetic energy budget (4.10) for the two filter lengths considered in this section, namely $\ell_F^* = 1.0$ and $\ell_F^* = 3.1$. Let us first consider the budget terms plotted in figure 4.6(c) as a function of z^* and for $\ell_F^* = 1.0$. The main plot shows that the average subgrid dissipation $\langle \epsilon_{sgs} \rangle$ almost balances the average viscous dissipation due to subgrid scales, $\langle \tilde{\epsilon}' \rangle$, at every wall-distance. Indeed, the transport $t_c^{u\prime} - t_{c,sgs}^u$ and the subgrid production $\pi^{u\prime}$ are both lower in magnitude than $\langle \tilde{\epsilon}' \rangle$. These findings are in agreement with the aforementioned role of the SGS stresses for $\ell_F^* < \ell_{c,min}^*$ consisting only in a drain of resolved energy to balance the viscous dissipation at subgrid scales. Though the sum of $t_c^{u\prime}$ and $-t_{c,sgs}^u$ is lower in magnitude than $\langle \tilde{\epsilon}' \rangle$, the distinct contributions are small throughout the bulk but comparable or even larger than $\langle \tilde{\epsilon}' \rangle$ close to the walls.

As shown by figure 4.7(c), the mechanisms driving the subgrid dissipation become more complex for $\ell_F^* > \ell_{c,min}^u$. Inside the bulk region ($z^* \gtrsim 2$), the resolved energy released to the subgrid motion, $\langle \epsilon_{sgs} \rangle$, balances the average viscous dissipation at subgrid scales, $\langle \tilde{\epsilon}' \rangle$, minus the subgrid production $\pi^{u\prime}$, whereas the transport $t_c^{u\prime} - t_{c,sgs}^u$ is nearly zero; therefore, the simplified relation $\langle \epsilon_{sgs} \rangle = \langle \tilde{\epsilon}' \rangle - \pi^{u\prime}$ is satisfied quite well away from the solid boundaries. The transport along z^* becomes important closer to the wall and balances the subgrid production. Since $\pi^{u\prime} \approx -t_c^{u\prime} + t_{c,sgs}^u$ around $z^* = 0.7$, then $\langle \epsilon_{sgs} \rangle \approx \langle \tilde{\epsilon}' \rangle$, thus explaining the anomalous relation $\bar{E}_e^u + E_{sgs}^u \approx E_e^u$ found in the transitional layer; see figure 4.7(b). These results confirm that, for $\ell_F^* > \ell_{c,min}^*$, the average subgrid dissipation is set by the combined action of viscous dissipation and inhomogeneous processes taking place at

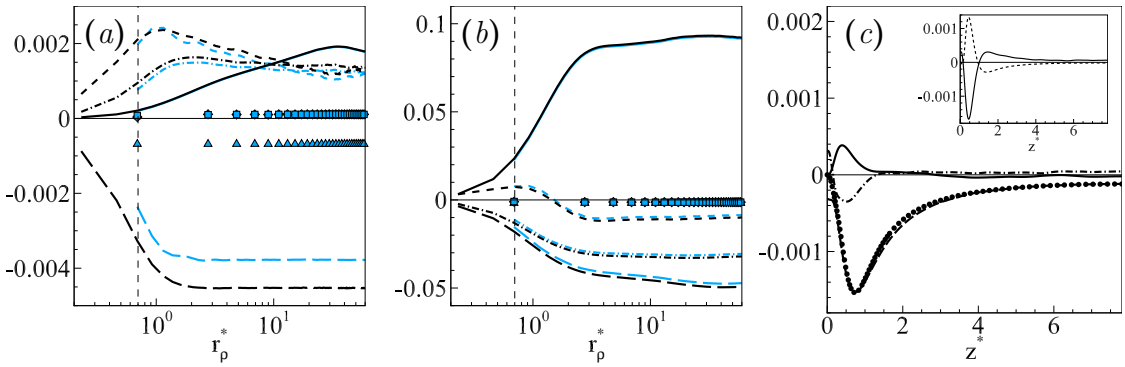

Figure 4.8: Scale-by-scale budgets (2.13) and (4.5) at (a) $z^* = 3$ and (b) $z^* = 0.4$ for $\ell_F^* = 0.7$. The plotted terms are the productions Π^θ and $\bar{\Pi}^\theta$ (solid line), the overall transports in physical space T_c^θ and $\bar{T}_c^\theta$ (dot-dashed line), the transfers in the space of scales I_r^θ and $\bar{I}_r^\theta$ (dashed line), the effective dissipation E_e^θ and $\bar{E}_e^\theta$ (long-dashed line), and the SGS terms $T_{c,sgs}^\theta$ (square), $T_{r,sgs}^\theta$ (diamond) and E_{sgs}^θ (triangle); the quantities of the unfiltered budget (2.13) are represented in black, the others in blue. The vertical dashed lines denotes ℓ_F^*. (c) Main plot: behaviour of $-\langle \chi_{sgs} \rangle$ (circles), $-\langle \chi' \rangle$ (long-dashed line), $t_c^{\theta\prime} - t_{c,sgs}^\theta$ (dot-dashed line) and $\pi^{\theta\prime}$ (solid line) as a function of z^* and for $\ell_F^* = 0.7$. Inset: profiles of $t_c^{\theta\prime}$ (solid line) and $-t_{c,sgs}^\theta$ (dashed line).

subgrid level; hence, it does not allow in general to recover the unfiltered dissipation, that is to say, $\bar{E}_e^u + E_{sgs}^u \neq E_e^u$.

4.3.3 Analysis of the filtered reduced Yaglom equation

We proceed with the analysis of the filtered reduced Yaglom equation (4.5) inside the thermal bulk, at $z^* = 3$, and inside the thermal transitional layer, at $z^* = 0.4$, for the filter lengths $\ell_F^* = 0.7$ and $\ell_F^* = 2.1$, which are smaller and larger than the minimum crossover scale for the temperature, $\ell_{c,min}^{\theta *} \approx 0.8$.

As can be seen in figure 4.8(a,b), the resolved physics is very rich for $\ell_F^* < \ell_{c,min}^{\theta *}$. The mechanisms of production and transport in physical space are captured well by the filtered fields ($\bar{\Pi}^\theta \approx \Pi^\theta$ and $\bar{T}_c^\theta \approx T_c^\theta$) and so is the transfer between scales ($\bar{I}_r^\theta \approx I_r^\theta$). In this case, the effect of the SGS heat flux is to drain resolved temperature variance ($E_{sgs}^\theta < 0$) with a negligible redistribution in the compound physical/scale space domain ($T_{c,sgs}^\theta \approx 0$ and $T_{r,sgs}^\theta \approx 0$). In analogy with the velocity field, the condition $\ell_F^* < \ell_{c,min}^\theta$ allows to resolve the inhomogeneous thermal processes, while it leaves the task of dissipating thermal fluctuations to the subgrid scales. Indeed, the rate at which temperature variance is transferred to subgrid scales is balanced by the missed dissipation at resolved scales, i.e. $\bar{E}_e^\theta + E_{sgs}^\theta \approx E_e^\theta$.

The scenario changes substantially for $\ell_F^* > \ell_{c,min}^{\theta *}$, as the resolved physics is

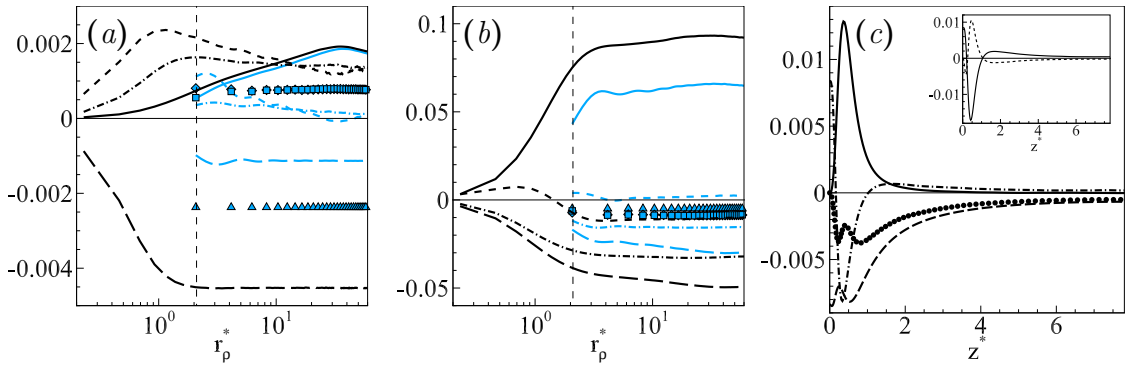

Figure 4.9: As figure 4.8 but for $\ell_F^* = 2.1$.

affected by the filtering operation and a significant portion of the inhomogeneous mechanisms is left to be taken into account by the SGS heat flux. The scale-by-scale budgets for $\ell_F^* = 2.1$, plotted in figure 4.9(a,b), reveal that $\bar{\Pi}^\theta + \bar{T}_c^u < \Pi^u + T_c^u$ both in the thermal bulk and in the thermal transitional layer. In particular, the production is adequately resolved inside the thermal bulk, where $\bar{\Pi}^\theta \approx \Pi^\theta$, but not inside the thermal transitional layer, where we observe a substantial depletion of $\bar{\Pi}^\theta$ with respect to Π^θ. This behavior can be explained by remarking that production processes are localized at large scales in the core of the flow, whereas small scales start to actively produce as the wall is approached. Contrary to production, the transport mechanisms in physical space are poorly resolved throughout the entire domain. This aspect is not surprising if we consider that a deterioration of the production mechanisms inside the transitional layer arguably implies a depletion of the spatial flux that departs from there to sustain the temperature fluctuations in the other regions of the flow ($|\bar{T}_c^\theta| \ll |T_c^\theta|$). The resolved transfer in the space of scales strongly depletes for the same reason and the reductions of the forward and reverse cascade, occurring in the bulk and transitional layer respectively, are more pronounced at large scales.

Based upon these premises, we can argue that the SGS heat flux plays an important role in the evolution of the resolved fields. In particular, the transport of resolved temperature variance in both physical and scale space is significantly modulated by the nonlinear interaction between resolved and subgrid scales, as the SGS redistribution terms $T_{c,sgs}^\theta$ and $T_{r,sgs}^\theta$ cannot be neglected in this case. The net exchange of temperature variance between resolved and subgrid scales is negative both in the thermal bulk and transitional layer, i.e. $E_{sgs}^\theta < 0$. However, the magnitude of the sink is not set solely by diffusive mechanisms but also by the inhomogeneous production and physical space transport mechanisms, which are significant at subgrid level for $\ell_F^* > \ell_{c,min}^{\theta *}$. Consequently, the subgrid dissipation does not allow to recover the unfiltered rate of dissipation, that is to say, $|\bar{E}_e^\theta + E_{sgs}^\theta| < |E_e^\theta|$.

To examine in more detail the behaviour of the average subgrid dissipation, we

analyze the subgrid temperature variance budget (4.11) for $\ell_F^* = 0.7$ and $\ell_F^* = 2.1$, which are plotted in figures 4.8(c) and 4.9(c) respectively. For $\ell_F^* < \ell_{c,min}^{\theta *}$, the average subgrid dissipation $\langle \chi_{sgs} \rangle$ balances the average dissipation due to the subgrid scales, $\langle \chi' \rangle$, at every wall-distance. The reason is that the subgrid production $\pi^{\theta'}$ and the subgrid transports along z^*, $t_c^{\theta'}$ and $-t_{c,sgs}^{\theta}$, are negligible inside the thermal bulk and, though they become significant closer to the wall, they balance together and thus do not modulate the average subgrid dissipation. These results suggest that, for $\ell_F^* < \ell_{c,min}^{\theta *}$, the single relevant phenomenon that the SGS heat flux should take into account is the dissipation occurring at subgrid level. For this reason, as anticipated so far in the analysis of the scale-by-scale budgets, the combination of resolved and subgrid dissipation allows us to recover the unfiltered rate of dissipation, i.e. $\bar{E}_e^{\theta} + E_{sgs}^{\theta} \approx E_e^{\theta}$. The picture becomes more complicated when $\ell_F^* > \ell_{c,min}^{\theta *}$. As can be seen in figure 4.9(c), $\langle \chi_{sgs} \rangle$ is not only driven by $\langle \chi' \rangle$ but also by $\pi^{\theta'}$, $t_c^{\theta'}$ and $-t_{c,sgs}^{\theta}$. In particular, inside the thermal bulk, the subgrid production is negligible; therefore, the average subgrid dissipation is set by the balance between space transport and dissipation at subgrid scales, i.e. $\langle \chi_{sgs} \rangle \approx -t_c^{\theta'} + t_{c,sgs}^{\theta} + \langle \chi' \rangle$. The production at subgrid scales becomes significant closer to the wall; hence, it does contribute to the value of the average subgrid dissipation.

In conclusion, for $\ell_F^* > \ell_{c,min}^{\theta *}$, subgrid scales are involved in strong inhomogeneous processes, so that subgrid dissipation does not take into account solely the dissipation at subgrid scales but also production and space transport mechanisms. Consequently, the sum of resolved and subgrid dissipation does not allow to recover the unfiltered rate of dissipation, since $|\bar{E}^{\theta} + E_s^{\theta}| \ll |E^{\theta}|$ as previously shown in the analysis of the filtered reduced Yaglom equation.

4.4 Modelling implications

As remarked in the introduction to this chapter, a proper SGS model should mimic, at least on average, the exchanges of turbulent kinetic energy and temperature variance between resolved and subgrid scales, that is to say, the average subgrid dissipations obtained from the modeled SGS stress tensor and heat flux should be similar, in magnitude and shape, to the ones obtained from the exact SGS stress tensor and heat flux. Because the real $\langle \epsilon_{sgs} \rangle$ and $\langle \chi_{sgs} \rangle$ depend on the balance between production, transport and dissipation occurring at subgrid scales, then the model for $\tau_{ij}^{\star}$ and $h_i^{\star}$ should reasonably account for the unresolved dynamics of the flow. This represents a challenge for RBC and wall-bounded flows in general, since the subgrid physics is complicated by the overlap between inhomogeneous and viscous/diffusive mechanisms sufficiently close to the solid boundaries.

In the first part of this section, we present an *a priori* assessment of two eddy-viscosity/diffusivity models that are commonly employed for the LES of thermally driven turbulence. It is worth anticipating that both models exhibit some evident limitations in copying the subgrid dissipations for large filter lengths due to

impossibility of reproducing the compound action of production and transport in physical space at subgrid level. In light of these shortcomings, we introduce a novel approach to derive a physics-based model of the SGS heat flux starting from the reduced Yaglom equation. This closure shows significative improvements with respect to the classic ones and paves the way for a future modelling of the SGS stress tensor using the Kolmogorov equation.

The earliest, but still most popular, SGS models for thermally-driven turbulence employ the eddy-viscosity/diffusivity approach [53, 32, 61, 11, 69] and they share the following form

$$\tau_{ij}^\star - 1/3\tau_{kk}^\star\delta_{ij} = -2C^u\ell_F^2\sigma\bar{S}_{ij}^\star, \tag{4.12a}$$

$$h_i^\star = -C^\theta\ell_F^2\sigma\bar{Q}_i^\star, \tag{4.12b}$$

where C^u and C^θ are the model coefficients and σ is the reciprocal of a characteristic subgrid time scale. Only the anisotropic part of the SGS stress tensor is modeled for consistency reason, as in incompressible flows the strain-rate tensor is trace-free, whereas the trace of $\tau_{ij}^\star$ differs in general from zero and, for a spectral cutoff filter, corresponds to two-times the subgrid turbulent kinetic energy. This requirement does not compromise the closure of the filtered governing equations since the trace of $\tau_{ij}^\star$ can be added to the filtered pressure to define a modified filtered pressure.

The SGS models of the form (4.12)(a,b) differentiate one from the other in the way σ is evaluated [11]. A subset estimates σ by accounting for buoyant effects explicitly; some of these closures, in particular, are derived from an equilibrium assumption that includes buoyancy forces in the local balance between production and viscous dissipation at subgrid level, e.g. [32, 61]. Complementary to the buoyancy models are the scalar models, which do not include a thermal correction, e.g. [53, 69]. The latter group include the well-known Smagorinsky model [86], for which

$$\sigma = |\bar{S}^\star| = \sqrt{2\bar{S}_{ij}^\star\bar{S}_{ij}^\star}. \tag{4.13}$$

The parameters C^u and C^θ can be either tuned *a priori* or computed with the dynamic procedure developed by Germano *et al.* [33] and later refined by Lilly [55], which allows the model coefficients to be a function of both space and time by extrapolating information from the smallest resolved scales [68]. This approach is based on the following identities,

$$\mathcal{L}_{ij} = T_{ij} - \hat{\tau}_{ij}^\star, \tag{4.14a}$$

$$\mathcal{E}_i = H_i - \hat{h}_i^\star, \tag{4.14b}$$

where $\widehat{\cdot}$ denotes a test filtering operation with a filter length $2\ell_F$, $\mathcal{L}_{ij} = \widehat{\bar{u}_i^\star\bar{u}_j^\star} - \hat{\bar{u}}_i^\star\hat{\bar{u}}_j^\star$ and $\mathcal{E}_i = \widehat{\bar{u}_i^\star\bar{\theta}^\star} - \hat{\bar{u}}_i^\star\hat{\bar{\theta}}^\star$ are the resolved turbulent stresses and heat flux, $T_{ij} = \widehat{u_i^\star u_j^\star} - \hat{\bar{u}}_i^\star\hat{\bar{u}}_j^\star$ and $H_i = \widehat{u_i^\star\theta^\star} - \hat{\bar{u}}_i^\star\hat{\bar{\theta}}^\star$ are the subtest stresses and heat flux. If the subtest

quantities in (4.14)(a,b) are calculated using the Smagorinsky model, then

$$\tau^\star_{ij}-1/3\tau^\star_{kk}\delta_{ij} = -2C^u\alpha^u_{ij},\ T_{ij}-1/2T_{kk}\delta_{ij} = -2C^u\beta^u_{ij},\ h^\star_i = -C^\theta\alpha^\theta_i \text{ and } H_i = -C^\theta\beta^\theta_i,$$

where $\alpha^u_{ij} = \ell^2_F|\bar{S}^\star|\bar{S}^\star_{ij}$, $\beta^u_{ij} = 4\ell^2_F|\hat{\bar{S}}^\star|\hat{\bar{S}}^\star_{ij}$, $\alpha^\theta_i = \ell^2_F|\bar{S}^\star|\bar{Q}^\star_i$ and $\beta^\theta_i = 4\ell^2_F|\hat{\bar{S}}^\star|\hat{\bar{Q}}^\star_i$. Upon substituting these into (4.14)(a,b), the identities (4.14)(a,b) can be satisfied only approximately because the stresses and the heat fluxes are replaced by models and because the system is overdetermined. Regarding the latter issue, the least-square minimization procedure suggested by Lilly [55] gives

$$C^u = -\frac{\left\langle \mathcal{L}_{ij}M^u_{ij}\right\rangle}{2\left\langle M^u_{ij}M^u_{ij}\right\rangle} \text{ and } C^\theta = -\frac{\left\langle \mathcal{E}_i M^\theta_i\right\rangle}{\left\langle {M_i}^\theta {M_i}^\theta\right\rangle}, \tag{4.15}$$

where $M^u_{ij} = \beta^u_{ij} - \hat{\alpha}^u_{ij}$ and $M^\theta_i = \beta^\theta_i - \hat{\alpha}^\theta_i$. Here, it should be remarked that C^u and C^θ in (4.15) can be calculated from the filtered velocity and temperature fields, $\bar{u}^\star_i$ and $\bar{\theta}^\star$, without the need for further information.

Most of the SGS models tailored for RBC are of the eddy-viscosity/diffusivity type [32, 98, 68, 83, 27], with few exceptions such as the the estimation model by Kimmel and Domaradzki [45]. The assessment is generally performed *a posteriori* by computing a LES and by comparing the results with experimental data [32, 11] or DNS data [98, 83]. Regarding the *a priori* assessment, Wong and Lilly [98] and Kimmel and Domaradzki [45] compare the model coefficients computed dynamically during LES with the ones obtained from a filtered DNS dataset, whereas only Kimmel and Domaradzki [45], to our knowledge, calculate the real and modeled SGS stress tensor and heat flux and the average subgrid dissipations using a filtered DNS data set.

The lack of literature on the subject justifies a deeper investigation; therefore, we proceed by assessing *a priori* the performances of two SGS models that have already been used in previous studies, namely the dynamic Smagorinsky model and the dynamic buoyancy model proposed by Peng and Davidson [68]. The latter, hereafter referred simply to as Peng model, represents an improved version of the Eidson model [32] intended to avoid non-real values of σ, which in this case is defined as

$$\sigma = \frac{1}{|\bar{S}^\star|}\left(|\bar{S}^\star|^2 - \frac{1}{Pr_t}\frac{\partial\bar{\theta}^\star}{\partial z}\right), \tag{4.16}$$

where the SGS Prandtl number Pr_t is usually set equal to 0.4 [11].

Figure 4.10(a,b) displays the average subgrid dissipations calculated from the exact SGS stress tensor and heat flux, from the dynamics Smagorinsky model and from the dynamic Peng model. As required by the *a priori* approach, the modeled SGS stress tensor and heat flux are computed using a filtered DNS data set (see DNS 3 in table 1.1). Although not shown here in detail, the dynamic Peng model leads to an average subgrid dissipation $\langle\epsilon_{sgs}\rangle$ that weakly depends on Pr_t; therefore, the buoyant correction that distinguish (4.16) from (4.13) has a negligible effect on the

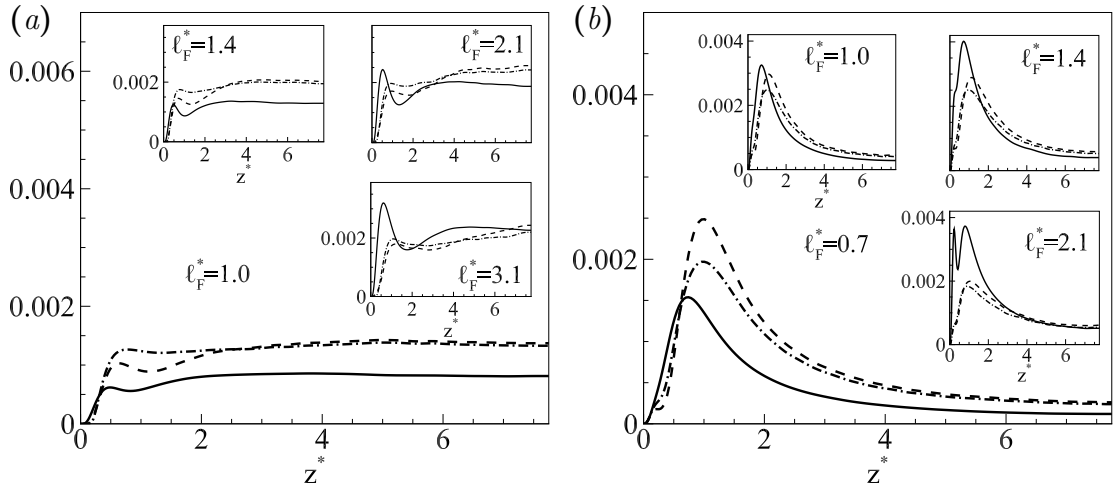

Figure 4.10: Profiles of (a) $\langle \epsilon_{sgs} \rangle$ and (b) $\langle \chi_{sgs} \rangle$ computed from the exact SGS stress tensor $\tau_{ij}^\star = \overline{u_i^\star u_j^\star} - \bar{u}_i^\star \bar{u}_j^\star$ and the exact SGS heat flux $h_i^\star = \overline{u_i^\star \theta^\star} - \bar{u}_i^\star \bar{\theta}^\star$ (solid line), from the dynamic Smagorinsky model (dashed line) and from the dynamic Peng model for $Pr_t = 0.4$ (dot-dashed line) as a function of z^* and for different filter lengths.

modeled SGS stress tensor. The same behaviour does not characterise the modeled SGS heat flux, as the dependence of $\langle \chi_{sgs} \rangle$ on the SGS Prandtl number has been proved to be relevant. Independently from the closure employed, the resulting $\langle \epsilon_{sgs} \rangle$ and $\langle \chi_{sgs} \rangle$ display a rather weak dependence on the filter length, that is to say, the dynamic procedure to calculate C^u and C^θ is unable to copy the real ℓ_F^*-behaviour of the subgrid dissipations. Finally, the shapes of the modeled profiles with respect to z^* are similar to the real ones when small filter lengths are considered, whereas they drift by a significant amount for large filters. This seems to be particularly true regarding the thermal behaviour, as both models fail to copy the first maximum of $\langle \chi_{sgs} \rangle$ around $z^* = 0.25$; see the lower inset in figure 4.10(b).

The relative position of ℓ_F^* with respect to the crossover scales $\ell_{c,min}^{u*}$ and $\ell_{c,min}^{\theta*}$ determines to what extent a SGS model is capable to copy the effect of the residual velocity and temperature field. As discussed in section 4.3, the transfer rates between resolved and subgrid scale, namely $\langle \epsilon_{sgs} \rangle$ and $\langle \chi_{sgs} \rangle$, are driven by the dissipations occurring at subgrid level when $\ell_F^* \lesssim \ell_{c,min}^{\theta*}$, thus classic eddy-viscosity/diffusivity models arguably contain enough physics to provide good results. On the other hand, by considering ℓ_F^* sufficiently larger than $\ell_{c,min}^{u*}$, the linear closures for $\tau_{ij}^\star$ and $h_i^\star$ are inadequate to mimic the subgrid scales, especially in the near-wall region, due to the relevance of production and space transport at scales below the filter. What emerges from the *a priori* study conducted up to now is that filter lengths around $\ell_{c,min}^{\theta*} \approx 0.8$ would likely capture most of the turbulent kinetic energy and temperature variance in actual LES. This behaviour should non change with the Rayleigh number as

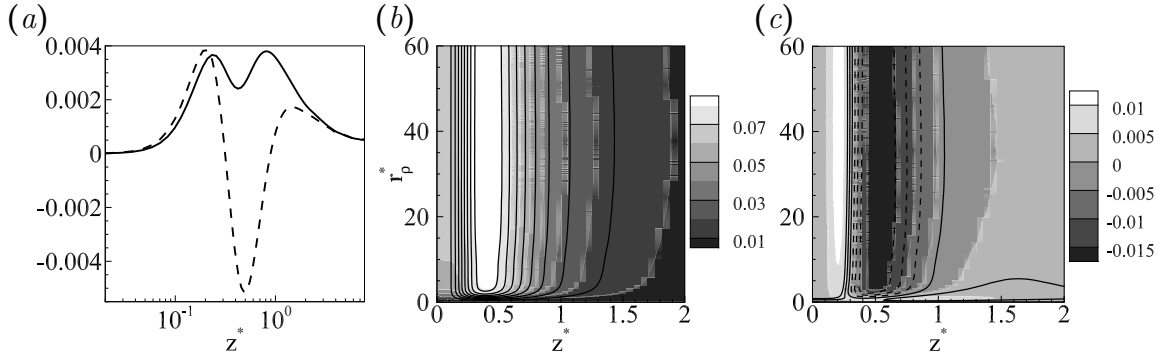

Figure 4.11: (a) Profiles of $\langle \chi_{sgs} \rangle (z^*; \ell_F^* = 2.1)$ (solid line) and $0.5 I_r^\theta (z^*; r_\rho^* = 2.1)$ (dashed line) as a function of z^*. (b) Isocontours of $\Pi^\theta + T_c^\theta$ (shadows of grey) and $c^\theta \Pi^\theta$ (solid lines) for $c^\theta = 0.7$. (c) Isocontours of I_r^θ (shadows of grey) and $-c^\theta \Pi^u - E_e^u$ (lines); the solid and dashed lines represent positive and negative contour levels respectively.

$\ell_{c,min}^{\theta *}$ is Ra-invariant and $\ell_{c,min}^{u*}$ increases with Ra; see figure 2.15(a,b). The eddy-viscosity/diffusivity models presented so far are expected to provide good results at small filter lengths, as they correctly reproduce the shape of the average subgrid dissipations. However, the resolution requirement $\ell_F^* \lesssim \ell_{c,min}^{\theta *}$ cannot be satisfied for very high Rayleigh numbers due to evident computational limitations; indeed, the maximum grid spacing along the homogeneous directions is upper bounded by $\ell_F \lesssim \ell_{c,min}^{\theta *}/Nu$, while the Nusselt number increases approximately with the $2/7$ power of the Rayleigh number [18]. For filter widths larger than $\ell_{c,min}^{\theta *}$, the inhomogeneous mechanisms of production and space transport are poorly resolved and the effect of the subgrid scales become even more complex, thus the improvement of SGS models become a sensible issue.

Because the Kolmogorov and the Yaglom equations have been proved to be of great support in describing the turbulent processes at different scales and locations in physical space, then we might consider the scale-by-scale analysis as an intriguing starting point for the development of a physics-based SGS models. This idea has been conceived by Cimarelli and De Angelis [21] and has brought to the formulation of a novel SGS stress model for the turbulent channel flow starting from the Kolmogorov equation [22]. This closure, which shares some basic aspects with the classic mixed models (e.g. the modeled SGS stress tensor presents an eddy-viscosity part and a scale-similar part), captures the near-wall dynamics for very large filter lengths, reproducing the reverse energy transfer from subgrid to resolved scales.

We now discuss how this approach can be extended to the modelling of the SGS heat flux in turbulent RBC. Here, it should be mentioned that a similar methodology has never been employed for thermally driven turbulence and future works will also address a closure for $\tau_{ij}^\star$. Let us start by considering a homogeneous and isotropic filtering operation with a filter length ℓ_F along the wall-parallel directions x and z.

If we evaluate the reduced Yaglom equation (2.13) for a separation $\boldsymbol{r} = (r_\rho, r_\phi, r_z) = (\ell_F, 0, 0)$, then I_r^θ should be proportional, at least from a conceptual point of view, to the average subgrid dissipation $\langle \chi_{sgs} \rangle$. Indeed, as previously remarked, $I_r^\theta(r_\rho, z)$ roughly measures the amount of temperature variance that is transferred, per unit time, from scales larger than r_ρ to scales smaller than r_ρ at the wall-distance z. Hence, it is reasonable to write

$$\langle \chi_{sgs} \rangle (z; \ell_F) \sim I_r^\theta(z; \ell_F) = -T_c^\theta(z; \ell_F) - \Pi^\theta(z; \ell_F) - E_e^\theta(z; \ell_F), \tag{4.17}$$

As can be seen in figure 4.11(a), the profiles of $\langle \chi_{sgs} \rangle (z; \ell_F)$ and $I_r^\theta(z; \ell_F)$ plotted for $\ell_F^* = 2.1$ are similar in shape and overlap perfectly inside the thermal bulk and the diffusive layer when I_r^θ is divided by two. Moreover, it has been proved that this behaviour does not change with the filter length.

Though the scale-by-scale analysis of the reduced Yaglom equation in section 2.3.3 has revealed a remarkable and apparently unavoidable complexity due to the interrelated processes of production, dissipation, transport in physical space and in the space of scales, a closer inspection of the budgets suggests an appealing simplification. Figure 4.11(b) compares the net source/drain of scale variance due to production and transport in physical space, i.e. $\Pi^\theta + T_c^\theta$, with the production Π^θ multiplied by a constant, $c^\theta = 0.7$. The two terms overlap rather well inside the thermal transitional layer, where they are maximum around $z^* \approx 0.5$, but they diverge closer to the wall and inside the thermal bulk. The magnitudes of both $\Pi^\theta + T_c^\theta$ and its simplification, $c^\theta \Pi^\theta$, decrease outside the thermal transitional layer, thus the discrepancies observed in the near-wall region and in the core can be neglected, at least on first approximation. Let us further test the accuracy of $\Pi^\theta + T_c^\theta \approx c^\theta \Pi^\theta$ by considering the consequent relation,

$$I_r^\theta \approx -c^\theta \Pi^\theta - E_e^\theta, \tag{4.18}$$

and by comparing the cascade term I_r^θ on the left-hand side with the modeled cascade $-c^\theta \Pi^\theta - E_e^\theta$ on the right-hand side. As can be seen in figure 4.11(c), the modeled transport in the space of scales captures the transition from a direct cascade inside the thermal bulk ($z^* \gtrsim 1$) to a reverse cascade inside the thermal transitional layer ($0.3 \lesssim z^* \lesssim 1$) and again to a direct cascade inside the diffusive layer ($z^* \lesssim 0.3$), although I_r^θ is far to be reproduced in magnitude apart for $0.3 \lesssim z^* \lesssim 1$.

If we substitute (4.18) into (4.17) and we recall the definition of subgrid dissipation, we obtain

$$2 \left\langle h_i \bar{Q}_i \right\rangle (z; \ell_F) \sim c^\theta \Pi^\theta(z; \ell_F) + E_e^\theta(z; \ell_F). \tag{4.19}$$

Then, it follows that the SGS heat flux can be modelled as

$$h_i^\star = \widetilde{C}^\theta \delta \bar{u}_i^\star \delta \bar{\theta}^\star - C^\theta \ell_F^2 |\bar{S}^\star| \bar{Q}_i^\star, \tag{4.20}$$

where $\widetilde{C}^\theta(z)$ and $C^\theta(z)$ are non-dimensional coefficients to be determined, and the increments $\delta \bar{u}_i^\star$ and $\delta \bar{\theta}^\star$ are evaluated between two points in the horizontal planes

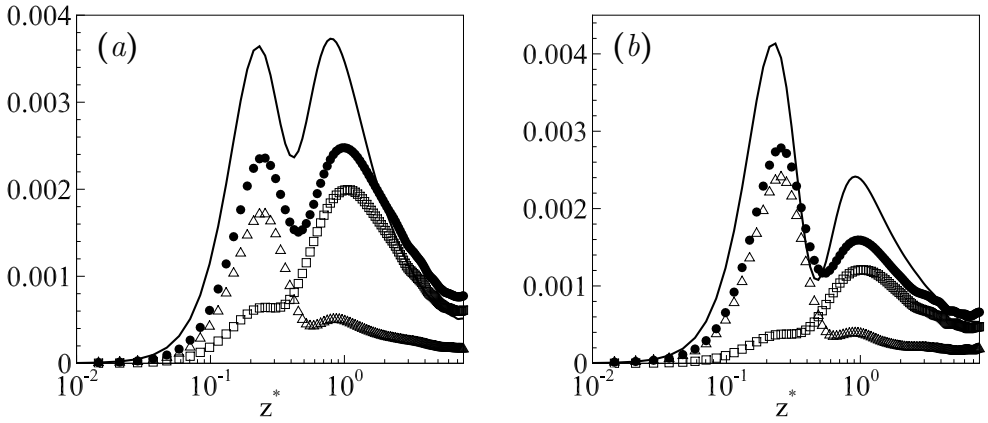

Figure 4.12: Average subgrid dissipation $\langle \chi_{sgs} \rangle$ computed from the exact SGS heat flux $h_i^\star = \overline{u_i^\star \theta^\star} - \bar{u}_i^\star \bar{\theta}^\star$ (solid line) and from the model (4.20) (filled circles) for (a) $\ell_F^* = 2.1$ and (b) $\ell_F^* = 3.1$. Here, $\widetilde{C}^\theta$ is a constant chosen *ad hoc* for each filter lenght: (a) $\widetilde{C}^\theta = 0.33$ and (b) $\widetilde{C}^\theta = 1$. The contribution of the scale-similar part, $\widetilde{C}^\theta \delta\bar{u}_i^\star \delta\bar{\theta}^\star$, and of the eddy-diffusivity part, $-C^\theta \ell_F^2 |\bar{S}^\star| \bar{Q}_i^\star$, to the modeled average subgrid dissipation are represented with empty squares and triangles respectively.

separated by a distance ℓ_F. The first term on the right-hand side, which is designed to mimic the filtered production $\bar{\Pi}^\theta$ when multiplied by $\bar{Q}_i^\star$, should reproduce the effect of the inhomogeneous mechanisms of production and transport occurring at subgrid level, whereas the second term, namely the Smagorinsky model, should account for the unresolved dissipation. This model belongs to the family of mixed models, as it presents an eddy-diffusivity part, (i.e. $-C^\theta \ell_F^2 |\bar{S}^\star| \bar{Q}_i^\star$) designed to mimic the global dissipative effect of the subgrid scales, and a scale-similar part (i.e. $\widetilde{C}^\theta \delta\bar{u}_i^\star \delta\bar{\theta}^\star$), deputed to modulate the transfer on a local level, as it can partially copy the correlation between resolved and subgrid scales.

Figure 4.12(a,b) represents the average subgrid dissipations computed from the exact SGS heat flux and from the model (4.20) for $\ell_F^* = 2.1$ and $\ell_F^* = 3.1$. While the coefficient C^θ of the Smagorinsky model is computed via the dynamic procedure (see the definition of C^θ in (4.15)), the coefficient $\widetilde{C}_\theta$ is chosen to be constant and tuned to achieve a good shape similarity between the real and the modeled average subgrid dissipations. The separate contributions of the scale-similar and eddy-diffusivity parts to the modeled $\langle \chi_{sgs} \rangle$ are also displayed to assess their different roles. As can be observed, the scale-similar term allows for a better reproduction of the real average subgrid dissipation at every z^*. The improvement is particularly evident close to the wall, where the first peak around $z^* = 0.25$ is copied well by the new model (4.20) rather than the Smagorinsky model (4.12)(b). Despite the use of *ad hoc* constants, the good reproduction of the profile shape suggests that the mixed formulation contains the necessary information to account for the subgrid dynamics

in a wide range of conditions, from small to large filter lengths. Moreover, the model coefficient $\widetilde{C}^\theta$ is closely related to c^θ that, in turn, corresponds to the ratio between the maximum of $\Pi^\theta + T_c^\theta$ and the maximum of Π^θ; hence, $\widetilde{C}^\theta$ has a non-trivial physical meaning that can be exploited, as an example, to develop a dynamic procedure for the computation of the model coefficient, in a similar way as it was done by Cimarelli *et al.* [22]. Despite these promising results, only the development of a dynamic technique and the *a posteriori* test of the resulting model may confirm the effective improvement, which will be addressed in future works.

4.5 Summarizing remarks

The resolved and subgrid dynamics of turbulent RBC have been assessed *a priori* using single-point and two-points budgets. Referring to the latter ones, the theoretical framework based on the filtered Kolmogorov and Yaglom equations, where the second is presented here for the first time, has been proved to be valuable in describing the resolved and subgrid physics of thermally driven turbulence in the compound physical/scale space domain and as a function of the filter length. All the balances are computed from a filtered DNS data set and analyzed for filter lengths that are selected in comparison with the minimum crossovers between inhomogeneous and quasi-homogeneous scales, namely $\ell_{c,min}^{u*}$ and $\ell_{c,min}^{\theta*}$.

In case $\ell_F^* < \ell_{c,min}^{\theta*}$, the inhomogeneous scales, which are responsible for production and transport in physical space, are properly resolved in the entire domain, whereas the main role of the subgrid scales is to drain turbulent kinetic energy and temperature variance at rates E_{sgs}^u and E_{sgs}^θ to recover the unfiltered dissipations, i.e. $E_e^u \approx \bar{E}_e^u + E_{sgs}^u$ and $E_e^\theta \approx \bar{E}_e^\theta + E_{sgs}^\theta$. For $\ell_{c,min}^{\theta*} \lesssim \ell_F^* \lesssim \ell_{c,min}^{u*}$, the energy production and transport mechanisms are still captured quite well, whereas the thermal counterparts are in general poorly resolved and the effects of the subgrid scales on the resolved temperature field become even more complex. In particular, the transfer rate of temperature variance between resolved and subgrid scales, E_{sgs}^θ, is not given by the unresolved dissipation alone but also by the inhomogeneous mechanisms occurring at subgrid level; hence, the recovery of the unfiltered dissipation, namely $E_e^\theta \approx \bar{E}_e^\theta + E_{sgs}^\theta$, is not generally observed. Finally, for $\ell_F^* \gtrsim \ell_{c,min}^{u*}$, the inhomogeneous energy processes are also poorly resolved and E_{sgs}^θ appears to be actively modulated by the unresolved production and transport in physical space.

The *a priori* test of two typical eddy-viscosity/diffusivity models reveals their capability to reproduce the subgrid dynamics for $\ell_F^* \lesssim \ell_{c,min}^{u*}$, as the only physics that needs to be copied is the dissipation of turbulent fluctuations occurring at subgrid level. On the other hand, both the dynamic Smagorinsky and Peng models show some deficiencies close to the walls and for $\ell_F^* \gtrsim \ell_{c,min}^{u*}$ since they do not consider the mechanisms induced by spatial inhomogeneity, namely the subgrid production and transport in physical space. The analysis of the reduced Yaglom equation suggests an alternative formulation for the SGS heat flux that combines the classic Smagorinsky

model and a scale-similar part, which account for the unresolved dissipation and the unresolved producion/transport in physical space, respectively. An *a priori* test of the mixed model shows some relevant improvements with respect to the other closures; hence, the proposed formulation seems to include the basic ingredients that are necessary to mimic the subgrid dynamics of thermally driven flows.

Chapter 5

Conclusions

Due to the ubiquity across many phenomena and the high level of complexity that derives from the coupling between temperature and velocity, thermally driven turbulence remains one of the most interesting and studied topics in fluid dynamics. Great progress has been made over the last years in understanding the dynamics of natural and industrial flows via the analysis of simplified systems, although many of the subtler effects still elude the researchers. This thesis aims to investigate some of these aspects by combining classic and novel approaches to the study of turbulent RBC with and without a complexity, namely the rotation around the vertical axis. The results can be divided into two parts that, however, are closely related to each other. The first one focuses on the behaviour of turbulent processes at different scales and locations in physical space, whereas the second addresses the filtered dynamics of RBC and some modelling aspects that are important for LES.

Physical and scale-by-scale analysis

A numerical study of turbulent RBC and RRBC has been pursued using DNS data at different Rayleigh numbers ($Ra = 1.7 \times 10^5$, 1.0×10^6 and 1.0×10^7), Rossby numbers ($1/Ro$ from 0 to 3.33) and for a single Prandtl number ($Pr = 0.7$). The self-sustained cycle of turbulence, along which fluctuations are produced, transported and dissipated, is initially depicted in terms of the coherent structures that emerge from the chaotic background and interact with each other. The flow topology provides only an intuitive description of the systems and thus needs to be enriched with the proper statistical analysis. In this respect, the turbulent kinetic energy and temperature variance equations play an important role, as they allow for the assessment of the different processes occurring in physical space. A novel division of the fluid domain into bulk, transitional and viscous/diffusive regions has been proposed on the basis of the single-point budgets to rationalize the dynamics of the flows at different wall-distances. Velocity fluctuations are produced by buoyancy inside the bulk region and then transported by pressure-velocity correlations into the transitional layer, from where they are redistributed by inertial and viscous

mechanisms to sustain the energy dissipation. The coupling between the temperature gradient and the convective heat flux generates temperature fluctuations inside the thermal transitional layer and the net amount produced is transported towards the core and the wall through inertia and diffusion, where it is finally dissipated. The rotation modulates the flow dynamics by reversing the inertial transport of turbulent kinetic energy inside the transitional layer. This statistical evidence has been associated with the fluid suction induced by rotating plumes or Ekman pumping, and the relative position between this process and the thermal boundary layer seems to determine the transition from a weakly rotating regime, characterized by heat flux enhancement, to a rapidly rotating regime, where the heat flux depletes.

The autonomous cycle of wall-turbulence is inherently multi-scale, that is to say, the processes involved depend not only on the location inside the domain but also on the length scale considered. In this regard, a theoretical framework based on the equations for the second-order velocity and temperature structure functions, namely the Kolmogorov and Yaglom equations, has been described and employed to address, for the first time, the dynamics of RBC and RRBC in the compound physical/scale space domain. These budgets represent the proper mathematical tool for studying inhomogeneous flows, as they allow for a neat description of the turbulent processes occurring at different scales and locations in physical space. Of particular interest is the scale-by-scale modulation of the turbulent processes due to spatial inhomogeneity. It has been observed, as an example, that the space of scales can be organised into three parts inside the bulk region: an inhomogeneity-dominated range at large scales, an inertial-like at intermediate scales and a dissipative one at small scales. This clear partition disappears inside the near-wall regions, as the inhomogeneous mechanisms of production and transport involve even smaller scales as the wall is approached and superimpose on viscous and diffusive processes. Another statistical evidence that characterizes the low bulk region and the transitional layer of both RBC and RRBC is the transfer of energy and temperature variance from small to large scales. The reverse cascade of energy seems to be a characteristic of wall-bounded turbulence rather than a specific feature of channel and pipe flows, for which it has already been observed in past studies.

The multi-scale analysis also supports and enriches the autonomous cycle introduced with the flow topology. According to the results obtained from the Kolmogorov equation, the large-scale circulations or rolls are responsible for most of the production and vertical transport of energy in RBC, whereas the rotation hinders the development of these structures and forces the system to produce and transport energy mainly at the scale of the thermal plumes. The process through which the thermal plumes group together into rolls has been associated with the reverse cascade of energy and temperature variance observed in the bulk region, while the statistical footprint of individual plumes is evident close to the wall, where the impingement and the Ekman pumping occur. In summary, the scale-by-scale analysis allows to identify the scales at which the turbulent processes develop and, consequently, to assign different dynamic roles to the coherent structures that populate the flows.

Analysis of the filtered dynamics and implications for LES modelling

The resolved and subgrid dynamics of turbulent RBC has been investigated *a priori* using a filtered DNS data set at $Ra = 1.0 \times 10^7$ and $Pr = 0.7$. The analysis of the filtered single-point budgets and their multi-scale extension, namely the filtered Kolmogorov and Yaglom equations, allows for a novel assessment of the resolved and subgrid physics in the compound physical/scale space domain and for different values of the filter length. Two characteristic scales have been identified in the first part of this thesis: a velocity crossover scale ℓ_c^u and a temperature crossover scale ℓ_c^θ. They both change as a function of the wall-distance and split the space of scales in two regions, namely the large, energy-containing scales and the small, dissipative ones. The results from the filtered budgets single out the prominent role of the filter length compared to ℓ_c^u and ℓ_c^θ. In particular, for filter lengths below the identified thresholds (i.e. $\ell_F < \ell_{c,min}^\theta$, as $\ell_c^\theta < \ell_c^u$ everywhere), it as been observed that the resolved processes almost correspond to the exact ones except for a depletion of the resolved dissipations. In this case, the only role of the subgrid scales is to drain the amounts of energy and temperature variance that are not dissipated by resolved motion and temperature, that is to say, $E_{sgs}^u \approx E_e^u - \bar{E}_e^u$ and $E_{sgs}^\theta \approx E_e^\theta - \bar{E}_e^\theta$. In the LES framework, this kind of phenomenology can be accurately reproduced with typical eddy-viscosity/diffusivity models, as it has been demonstrated by the *a priori* test of the dynamic Smagorisnky and Peng models.

When ℓ_F is sufficiently larger than $\ell_{c,min}^\theta$, a substaintial fraction of the inhomogeneous range belongs to the subgrid scales; therefore, the physics of the flow is poorly resolved and the role of the subgrid scales is not only dissipative. With reference to the second issue, the exchanges of energy and temperature variance between resolved and subgrid scales, E_{sgs}^θ and E_{sgs}^θ, are set by the unresolved dissipations plus the inhomogeneous processes occurring at subgrid level; hence, the recovery of the unfiltered dissipation, namely $E_e^\theta \approx \bar{E}_e^\theta + E_{sgs}^\theta$ and $E_e^\theta \approx \bar{E}_e^\theta + E_{sgs}^\theta$, does not occur in general. According to this phenomenology, both the dynamic Smagorinsky and Peng models have been proved to hardly reproduce the effect of the subgrid scales when $\ell_F^* > 2\ell_{c,min}^{\theta *} \approx 1.4$, especially in the near-wall region. This is related to the fact that inhomogeneous mechanisms, like production and transport in physical space, are not accounted by the eddy-viscosity/diffusivity formulation.

Finally, a novel approach for the development of physics-based SGS models has been outlined. Starting from the Yaglom equation, a model is formulated for the SGS heat flux that combines an eddy-diffusivity part and a scale-similar one. The latter contains the product of the filtered velocity and temperature increments, which should mimic the unresolved production and transport in physical space that are relevant at large filter lengths. An *a priori* test of the model shows some relevant improvements in the near-wall region. However, further tests are required to validate or not the effective improvement of the new model in LES of turbulent RBC and, in general, of wall-bounded thermally driven flows.

Appendix A

Generalized and specialized Kolmogorov equation

In this appendix, the Kolmogorov equation is derived for a generic buoyancy driven flow that is governed by the Boussinesq equations, and then specialized to the Rayleigh-Bénard convection (RBC). Note that a similar procedure can be followed also for deriving the Yaglom equation, although it is not presented here for brevity. Let us start by subtracting the averaged momentum equation from (1.1)(b). The equation for the fluctuating momentum reads as

$$\begin{aligned}&\frac{\partial u_i}{\partial t}+\frac{\partial\left(u_iu_j+u_iU_j+U_iu_j-\langle u_iu_j\rangle\right)}{\partial x_j}+\frac{1}{Ro}\epsilon_{i3k}u_k=-\frac{\partial p}{\partial x_i}\\&+\sqrt{\frac{Pr}{Ra}}\frac{\partial^2u_i}{\partial x_j\partial x_j}+\theta\delta_{i3},\end{aligned}\tag{A.1}$$

where U_i is the average velocity field. We proceed by subtracting equation (A.1) evaluated at x_i^{II} from the same evaluated at x_i^{I}, where x_i^{II} and x_i^{I} are two generic and independent locations in the fluid domain. The resulting equation reads as

$$\begin{aligned}&\frac{\partial\left(u_i^{\mathrm{II}}-u_i^{\mathrm{I}}\right)}{\partial t}+u_j^{\mathrm{II}}\frac{\partial u_i^{\mathrm{II}}}{\partial x_j^{\mathrm{II}}}-u_j^{\mathrm{I}}\frac{\partial u_i^{\mathrm{I}}}{\partial x_j^{\mathrm{I}}}+U_j^{\mathrm{II}}\frac{\partial u_i^{\mathrm{II}}}{\partial x_j^{\mathrm{II}}}-U_j^{\mathrm{I}}\frac{\partial u_i^{\mathrm{I}}}{\partial x_j^{\mathrm{I}}}+u_j^{\mathrm{II}}\frac{\partial U_i^{\mathrm{II}}}{\partial x_j^{\mathrm{II}}}-u_j^{\mathrm{I}}\frac{\partial U_i^{\mathrm{I}}}{\partial x_j^{\mathrm{I}}}\\&-\frac{\partial\left\langle u_i^{\mathrm{II}}u_j^{\mathrm{II}}\right\rangle}{\partial x_j^{\mathrm{II}}}+\frac{\partial\left\langle u_i^{\mathrm{I}}u_j^{\mathrm{I}}\right\rangle}{\partial x_j^{\mathrm{I}}}+\frac{1}{Ro}\epsilon_{i3k}\left(u_k^{\mathrm{II}}-u_k^{\mathrm{I}}\right)=-\frac{\partial p^{\mathrm{II}}}{\partial x_i^{\mathrm{II}}}+\frac{\partial p^{\mathrm{I}}}{\partial x_i^{\mathrm{I}}}\\&+\sqrt{\frac{Pr}{Ra}}\left(\frac{\partial^2u_i^{\mathrm{II}}}{\partial x_j^{\mathrm{II}}\partial x_j^{\mathrm{II}}}-\frac{\partial^2u_i^{\mathrm{I}}}{\partial x_j^{\mathrm{I}}\partial x_j^{\mathrm{I}}}\right)+\left(\theta^{\mathrm{II}}-\theta^{\mathrm{I}}\right)\delta_{i3}.\end{aligned}\tag{A.2}$$

Since $\partial\beta^{\mathrm{I}}/\partial x_i^{\mathrm{II}} = 0$ and $\partial\beta^{\mathrm{II}}/\partial x_i^{\mathrm{I}} = 0$ for a generic β, we can rewrite (A.2) as

$$\begin{aligned}
&\frac{\partial\left(u_i^{\mathrm{II}}-u_i^{\mathrm{I}}\right)}{\partial t}+u_j^{\mathrm{II}}\frac{\partial\left(u_i^{\mathrm{II}}-u_i^{\mathrm{I}}\right)}{\partial x_j^{\mathrm{II}}}+u_j^{\mathrm{I}}\frac{\partial\left(u_i^{\mathrm{II}}-u_i^{\mathrm{I}}\right)}{\partial x_j^{\mathrm{I}}}+U_j^{\mathrm{II}}\frac{\partial\left(u_i^{\mathrm{II}}-u_i^{\mathrm{I}}\right)}{\partial x_j^{\mathrm{II}}}\\
&+U_j^{\mathrm{I}}\frac{\partial\left(u_i^{\mathrm{II}}-u_i^{\mathrm{I}}\right)}{\partial x_j^{\mathrm{I}}}+u_j^{\mathrm{II}}\frac{\partial\left(U_i^{\mathrm{II}}-U_i^{\mathrm{I}}\right)}{\partial x_j^{\mathrm{II}}}+u_j^{\mathrm{I}}\frac{\partial\left(U_i^{\mathrm{II}}-U_i^{\mathrm{I}}\right)}{\partial x_j^{\mathrm{I}}}-\frac{\partial\left\langle u_i^{\mathrm{II}}u_j^{\mathrm{II}}\right\rangle}{\partial x_j^{\mathrm{II}}}\\
&+\frac{\partial\left\langle u_i^{\mathrm{I}}u_j^{\mathrm{I}}\right\rangle}{\partial x_j^{\mathrm{I}}}+\frac{1}{Ro}\epsilon_{i3k}\left(u_k^{\mathrm{II}}-u_k^{\mathrm{I}}\right)=-\frac{\partial\left(p^{\mathrm{II}}-p^{\mathrm{I}}\right)}{\partial x_i^{\mathrm{II}}}-\frac{\partial\left(p^{\mathrm{II}}-p^{\mathrm{I}}\right)}{\partial x_i^{\mathrm{I}}}\\
&+\sqrt{\frac{Pr}{Ra}}\left(\frac{\partial^2\left(u_i^{\mathrm{II}}-u_i^{\mathrm{I}}\right)}{\partial x_j^{\mathrm{II}}\partial x_j^{\mathrm{II}}}+\frac{\partial^2\left(u_i^{\mathrm{II}}-u_i^{\mathrm{I}}\right)}{\partial x_j^{\mathrm{I}}\partial x_j^{\mathrm{I}}}\right)+\left(\theta^{\mathrm{II}}-\theta^{\mathrm{I}}\right)\delta_{i3}.
\end{aligned}\tag{A.3}$$

It is appropriate to change the independent variables as $x_i^{\mathrm{I}} = x_i - r_i/2$ and $x_i^{\mathrm{II}} = x_i + r_i/2$, where $r_i = x_i^{\mathrm{II}} - x_i^{\mathrm{I}}$ is the separation vector and $x_i = 0.5\left(x_i^{\mathrm{I}} + x_i^{\mathrm{II}}\right)$ is the mid-point. The rules for the derivatives are

$$\frac{\partial}{\partial x_i^{\mathrm{I}}} = -\frac{\partial}{\partial r_i}+\frac{1}{2}\frac{\partial}{\partial x_i} \text{ and } \frac{\partial}{\partial x_i^{\mathrm{II}}} = \frac{\partial}{\partial r_i}+\frac{1}{2}\frac{\partial}{\partial x_i}.$$

Equation (A.3) can be rewritten as

$$\begin{aligned}
&\frac{\partial\delta u_i}{\partial t}+\delta u_j\frac{\partial\delta u_i}{\partial r_j}+u_j^{\dagger}\frac{\partial\delta u_i}{\partial x_j}+\delta U_j\frac{\partial\delta u_i}{\partial r_j}+U_j^{\dagger}\frac{\partial\delta u_i}{\partial x_j}+\delta u_j\frac{\partial\delta U_i}{\partial r_j}+u_j^{\dagger}\frac{\partial\delta U_i}{\partial x_j}\\
&-\frac{\partial\left\langle u_i^{\mathrm{II}}u_j^{\mathrm{II}}\right\rangle}{\partial r_j}-\frac{1}{2}\frac{\partial\left\langle u_i^{\mathrm{II}}u_j^{\mathrm{II}}\right\rangle}{\partial x_j}-\frac{\partial\left\langle u_i^{\mathrm{I}}u_j^{\mathrm{I}}\right\rangle}{\partial r_j}+\frac{1}{2}\frac{\partial\left\langle u_i^{\mathrm{I}}u_j^{\mathrm{I}}\right\rangle}{\partial x_j}+\frac{1}{Ro}\epsilon_{i3k}\delta u_k=\\
&-\frac{\partial\delta p}{\partial x_i}+2\sqrt{\frac{Pr}{Ra}}\frac{\partial^2\delta u_i}{\partial r_j\partial r_j}+\frac{1}{2}\sqrt{\frac{Pr}{Ra}}\frac{\partial^2\delta u_i}{\partial x_j\partial x_j}+\delta\theta\delta_{i3},
\end{aligned}\tag{A.4}$$

where $\delta u_i = u_i^{\mathrm{II}} - u_i^{\mathrm{I}}$, $\delta p = p^{\mathrm{II}} - p^{\mathrm{I}}$, $\delta\theta = \theta^{\mathrm{II}} - \theta^{\mathrm{I}}$ are the fluctuating increments and the dagger denotes the mid-point average $\beta^{\dagger} = (\beta(x_j - r_j/2) + \beta(x_j + r_j/2))/2$. Let us multiply (A.4) by δu_l and average the resulting equation,

$$\begin{aligned}
&\left\langle\delta u_l\frac{\partial\delta u_i}{\partial t}\right\rangle+\left\langle\delta u_l\delta u_j\frac{\partial\delta u_i}{\partial r_j}\right\rangle+\left\langle\delta u_l u_j^{\dagger}\frac{\partial\delta u_i}{\partial x_j}\right\rangle+\left\langle\delta u_l\delta U_j\frac{\partial\delta u_i}{\partial r_j}\right\rangle\\
&+\left\langle\delta u_l U_j^{\dagger}\frac{\partial\delta u_i}{\partial x_j}\right\rangle+\left\langle\delta u_l\delta u_j\frac{\partial\delta U_i}{\partial r_j}\right\rangle+\left\langle\delta u_l u_j^{\dagger}\frac{\partial\delta U_i}{\partial x_j}\right\rangle+\frac{1}{Ro}\left\langle\delta u_l\epsilon_{i3k}\delta u_k\right\rangle\\
&=-\left\langle\delta u_l\frac{\partial\delta p}{\partial x_i}\right\rangle+2\sqrt{\frac{Pr}{Ra}}\left\langle\delta u_l\frac{\partial^2\delta u_i}{\partial r_j\partial r_j}\right\rangle+\frac{1}{2}\sqrt{\frac{Pr}{Ra}}\left\langle\delta u_l\frac{\partial^2\delta u_i}{\partial x_j\partial x_j}\right\rangle\\
&+\left\langle\delta u_l\delta\theta\delta_{i3}\right\rangle.
\end{aligned}\tag{A.5}$$

We sum (A.5) with (A.4) written for δu_l and multiplied by δu_i,

$$\begin{aligned}
&\frac{\partial \langle \delta u_i \delta u_l \rangle}{\partial t} + \frac{\partial \langle \delta u_i \delta u_j \delta u_l \rangle}{\partial r_j} + \frac{\partial \left\langle \delta u_i u_j^\dagger \delta u_l \right\rangle}{\partial x_j} + \frac{\partial \langle \delta u_i \delta U_j \delta u_l \rangle}{\partial r_j} \\
&+ \frac{\partial \left\langle \delta u_i U_j^\dagger \delta u_l \right\rangle}{\partial x_j} + \left\langle \delta u_l \delta u_j \frac{\partial \delta U_i}{\partial r_j} \right\rangle + \left\langle \delta u_i \delta u_j \frac{\partial \delta U_l}{\partial r_j} \right\rangle + \left\langle \delta u_l u_j^\dagger \frac{\partial \delta U_i}{\partial x_j} \right\rangle \\
&+ \left\langle \delta u_i u_j^\dagger \frac{\partial \delta U_l}{\partial x_j} \right\rangle + \frac{1}{Ro} \langle (\delta u_l \epsilon_{i3k} + \delta u_i \epsilon_{l3k}) \, \delta u_k \rangle = - \left\langle \delta u_l \frac{\partial \delta p}{\partial x_i} \right\rangle \\
&- \left\langle \delta u_i \frac{\partial \delta p}{\partial x_l} \right\rangle + 2\sqrt{\frac{Pr}{Ra}} \left(\frac{\partial^2 \langle \delta u_i \delta u_l \rangle}{\partial r_j \partial r_j} - 2 \left\langle \frac{\partial \delta u_l}{\partial r_j} \frac{\partial \delta u_i}{\partial r_j} \right\rangle \right) \\
&+ \frac{1}{2}\sqrt{\frac{Pr}{Ra}} \left(\frac{\partial^2 \langle \delta u_l \delta u_i \rangle}{\partial x_j \partial x_j} - 2 \left\langle \frac{\partial \delta u_l}{\partial x_j} \frac{\partial \delta u_i}{\partial x_j} \right\rangle \right) + \langle \delta\theta \, (\delta_{i3} \delta u_l + \delta_{l3} \delta u_i) \rangle \, .
\end{aligned} \tag{A.6}$$

For $i = l$, we obtain the generalized Kolmogorov equation

$$\begin{aligned}
&\frac{\partial \langle \delta u^2 \rangle}{\partial t} + \frac{\partial \langle \delta u^2 \delta u_j \rangle}{\partial r_j} + \frac{\partial \left\langle u_j^\dagger \delta u^2 \right\rangle}{\partial x_j} + \frac{\partial \left(\delta U_j \langle \delta u^2 \rangle \right)}{\partial r_j} + \frac{\partial \left(\delta U_j^\dagger \langle \delta u^2 \rangle \right)}{\partial x_j} \\
&+ 2 \langle \delta u_i \delta u_j \rangle \frac{\partial \delta U_i}{\partial r_j} + 2 \left\langle \delta u_i u_j^\dagger \right\rangle \frac{\partial \delta U_i}{\partial x_j} = -2 \frac{\partial \langle \delta p \delta u_i \rangle}{\partial x_i} \\
&+ 2\sqrt{\frac{Pr}{Ra}} \frac{\partial^2 \langle \delta u^2 \rangle}{\partial r_j \partial r_j} + \frac{1}{2}\sqrt{\frac{Pr}{Ra}} \frac{\partial^2 \langle \delta u^2 \rangle}{\partial x_j \partial x_j} - 4 \left\langle \tilde{\epsilon}^\dagger \right\rangle + 2 \langle \delta\theta \delta w \rangle \, ,
\end{aligned} \tag{A.7}$$

where the two-point averaged pseudo-dissipation is

$$\left\langle \tilde{\epsilon}^\dagger \right\rangle = \sqrt{\frac{Pr}{Ra}} \left\langle \frac{\partial \delta u_i}{\partial r_j} \frac{\partial \delta u_i}{\partial r_j} + \frac{1}{4} \frac{\partial \delta u_i}{\partial x_j} \frac{\partial \delta u_i}{\partial x_j} \right\rangle . \tag{A.8}$$

Fully-developed turbulent RBC is statistically stationary, homogeneous and isotropic in horizontal directions, thus $U_i = 0$. In this case, equation (A.7) reduces to the Kolmogorov equation specialized for RBC,

$$\begin{aligned}
&\frac{\partial \left\langle w^\dagger \delta u^2 \right\rangle}{\partial z} + \frac{\partial \langle \delta u^2 \delta u_j \rangle}{\partial r_j} = -2 \frac{\partial \langle \delta p \delta w \rangle}{\partial z} \\
&+ 2\sqrt{\frac{Pr}{Ra}} \frac{\partial^2 \langle \delta u^2 \rangle}{\partial r_j \partial r_j} + \frac{1}{2}\sqrt{\frac{Pr}{Ra}} \frac{\partial^2 \langle \delta u^2 \rangle}{\partial z^2} - 4 \left\langle \tilde{\epsilon}^\dagger \right\rangle + 2 \langle \delta\theta \delta w \rangle \, .
\end{aligned} \tag{A.9}$$

For $r = \sqrt{r_i r_i} \gg \ell_0$, where $\ell_0 = \ell_0(z)$ is the local integral scale of the flow, the variables evaluated at x_i^{I} and x_i^{II} are uncorrelated, which implies that

$$\left\langle \delta u^2 \right\rangle = \left\langle u_i^{\mathrm{I}} u_i^{\mathrm{I}} \right\rangle + \left\langle u_i^{\mathrm{II}} u_i^{\mathrm{II}} \right\rangle - 2 \left\langle u_i^{\mathrm{I}} u_i^{\mathrm{II}} \right\rangle \xrightarrow{r \gg \ell_0} 2 \langle u_i u_i \rangle^\dagger = 4 \langle k \rangle^\dagger \, ,$$

$$\frac{\partial\left\langle w^{\dagger}\delta u^{2}\right\rangle}{\partial z}\xrightarrow{r\gg\ell_0}\frac{1}{2}\left(\frac{d\left\langle w^{\mathrm{I}}u_i^{\mathrm{I}}u_i^{\mathrm{I}}\right\rangle}{dz^{\mathrm{I}}}+\frac{d\left\langle w^{\mathrm{II}}u_i^{\mathrm{II}}u_i^{\mathrm{II}}\right\rangle}{dz^{\mathrm{II}}}\right)=2\left(\frac{d\left\langle wk\right\rangle}{dz}\right)^{\dagger},$$

$$\frac{\partial\left\langle \delta u^{2}\delta u_j\right\rangle}{\partial r_j}\xrightarrow{r\gg\ell_0}\frac{1}{2}\left(\frac{\partial\left\langle u_i^{\mathrm{I}}u_i^{\mathrm{I}}u_j^{\mathrm{I}}\right\rangle}{\partial x^{\mathrm{I}}}+\frac{\partial\left\langle u_i^{\mathrm{II}}u_i^{\mathrm{II}}u_j^{\mathrm{II}}\right\rangle}{\partial x^{\mathrm{II}}}\right)=2\left(\frac{d\left\langle wk\right\rangle}{dz}\right)^{\dagger},$$

$$-2\frac{\partial\left\langle \delta p\delta w\right\rangle}{\partial z}\xrightarrow{r\gg\ell_0}-2\left(\frac{\partial\left\langle p^{\mathrm{I}}w^{\mathrm{I}}\right\rangle}{dz^{\mathrm{I}}}+\frac{\partial\left\langle p^{\mathrm{II}}w^{\mathrm{II}}\right\rangle}{dz^{\mathrm{II}}}\right)=-4\left(\frac{d\left\langle pw\right\rangle}{dz}\right)^{\dagger},$$

$$2\sqrt{\frac{Pr}{Ra}}\frac{\partial^{2}\left\langle \delta u^{2}\right\rangle}{\partial r_j\partial r_j}\xrightarrow{r\gg\ell_0}\frac{1}{2}\sqrt{\frac{Pr}{Ra}}\left(\frac{\partial^{2}\left\langle u_i^{\mathrm{I}}u_i^{\mathrm{I}}\right\rangle}{\partial x_i^{\mathrm{I}}\partial x_i^{\mathrm{I}}}+\frac{\partial^{2}\left\langle u_i^{\mathrm{II}}u_i^{\mathrm{II}}\right\rangle}{\partial x_i^{\mathrm{II}}\partial x_i^{\mathrm{II}}}\right)=2\sqrt{\frac{Pr}{Ra}}\left(\frac{d\left\langle k\right\rangle}{dz^{2}}\right)^{\dagger},$$

$$\frac{1}{2}\sqrt{\frac{Pr}{Ra}}\frac{\partial^{2}\left\langle \delta u^{2}\right\rangle}{\partial z^{2}}\xrightarrow{r\gg\ell_0}\frac{1}{2}\sqrt{\frac{Pr}{Ra}}\left(\frac{\partial^{2}\left\langle u_i^{\mathrm{I}}u_i^{\mathrm{I}}\right\rangle}{\partial x_i^{\mathrm{I}}\partial x_i^{\mathrm{I}}}+\frac{\partial^{2}\left\langle u_i^{\mathrm{II}}u_i^{\mathrm{II}}\right\rangle}{\partial x_i^{\mathrm{II}}\partial x_i^{\mathrm{II}}}\right)=2\sqrt{\frac{Pr}{Ra}}\left(\frac{d\left\langle k\right\rangle}{dz^{2}}\right)^{\dagger},$$

$$2\left\langle \delta\theta\delta w\right\rangle=\left\langle \theta^{\mathrm{I}}w^{\mathrm{I}}\right\rangle+\left\langle \theta^{\mathrm{II}}w^{\mathrm{II}}\right\rangle-2\left\langle \theta^{\mathrm{I}}w^{\mathrm{II}}\right\rangle\xrightarrow{r\gg\ell_0}4\left\langle \theta w\right\rangle^{\dagger}.$$

Hence, the Kolmogorov equation converges to four-times the mid-point average of the turbulent kinetic energy budget (2.1) when $r=\sqrt{r_ir_i}\gg\ell_0$.

Acknowledgements

Firstly, I would like to express my sincere gratitude to my supervisor, Prof. Elisabetta De Angelis, for the support in my Ph.D study and research, for her patience, motivation, and guidance that made this work possible. I learned from her (hopefully) to do good science, to be self-critical and humble. I am also grateful to her for having welcomed me in Cardiff during my experience as a visiting student, for having shared happy and tough moments, and for the work that she has been doing for me to ensure a continuity to this fruitful cooperation.

Besides my supervisor, I would like to thank Andrea Cimarelli for his constant help during the last three years. Besides the essential contribution to my research and to this thesis, not to mention his great support during the Multiflow Summer Workshop in Madrid, Andrea always brought cheerfulness to the workplace and taught me many things in both science and life.

I am grateful to my friends in Forlì for the discussions, for the days spent together in the office, and for all the fun we have had in the last three years; thank you Tommaso, Matteo and, last but not least, Michael and Jessica to whom I wish the best for their Ph.D studies. A special thank goes also to Prof. Marco Lorenzini for the honesty and the sympathy towards me; his rare sagacity and humour made the workplace a better place.

My immense gratitude goes to my father Agostino, my mother Tina and my brothers Roberto and Alessandro for their support, encouragement, and love. They have been my safe harbour, even when I was far away from home. A special thank goes to my girlfriend Birgit, as her vicinity, love and joy have been of great help during the last period of my Ph.D and especially during the writing process. I am also grateful to her family and especially to her father, Eric, who assisted me in the proofreading.

Finally, I would like to thank the Advanced Research Computing at Cardiff (ARCCA) for providing me with the computational resources and Cardiff University for having accepted me as a visiting postgraduate student.

Bibliography

[1] G. Ahlers. Trend: turbulent convection. *Physics*, 2:74, 2009.

[2] R. A. Antonia, L. Djenidi, and P. R. Spalart. Anisotropy of the dissipation tensor in a turbulent boundary layer. *Physics of Fluids (1994-present)*, 6(7):2475–2479, 1994.

[3] M. Antonopoulos-Domis. Large-eddy simulation of a passive scalar in isotropic turbulence. *Journal of Fluid Mechanics*, 104:55–79, 1981.

[4] R. Bolgiano. Turbulent spectra in a stably stratified atmosphere. *Journal of Geophysical Research*, 64(12):2226–2229, 1959.

[5] J. Boussinesq. *Théorie analytique de la chaleur: mise en harmonie avec la thermodynamique et avec la théorie mécanique de la lumière*, volume 2. Gauthier-Villars, 1903.

[6] A. D. Brent, V. R. Voller, and K. T. J. Reid. Enthalpy-porosity technique for modeling convection-diffusion phase change: application to the melting of a pure metal. *Numerical Heat Transfer, Part A Applications*, 13(3):297–318, 1988.

[7] E. Brown and G. Ahlers. Rotations and cessations of the large-scale circulation in turbulent Rayleigh-Bénard convection. *Journal of Fluid Mechanics*, 568:351–386, 2006.

[8] G. H. Bryan, J. C. Wyngaard, and J. M. Fritsch. Resolution requirements for the simulation of deep moist convection. *Monthly Weather Review*, 131(10):2394–2416, 2003.

[9] P. Burattini, R. A. Antonia, and L. Danaila. Scale-by-scale energy budget on the axis of a turbulent round jet. *Journal of Turbulence*, 6:19, 2005.

[10] F. H. Busse. Convection driven zonal flows and vortices in the major planets. *Chaos: An Interdisciplinary Journal of Nonlinear Science*, 4(2):123–134, 1994.

[11] W. H. Cabot. Large eddy simulations of time-dependent and buoyancy-driven channel flows. *Annual Research Briefs, 1992*, pages 45–60, 1993.

[12] C. Canuto, M. Y. Hussaini, A. M. Quarteroni, and A. Thomas Jr. *Spectral methods in fluid dynamics*. Springer Science & Business Media, 2012.

[13] P. Cardin and P. Olson. Chaotic thermal convection in a rapidly rotating spherical shell: consequences for flow in the outer core. *Physics of the earth and planetary interiors*, 82(3-4):235–259, 1994.

[14] F. Cattaneo, T. Emonet, and N. Weiss. On the interaction between convection and magnetic fields. *The Astrophysical Journal*, 588(2):1183, 2003.

[15] S. Chandrasekhar. The instability of a layer of fluid heated below and subject to Coriolis forces. In *Proceedings of the Royal Society of London A: Mathematical, Physical and Engineering Sciences*, volume 217, pages 306–327. The Royal Society, 1953.

[16] S. Chandrasekhar. *Hydrodynamic and hydromagnetic stability*. Courier Corporation, 2013.

[17] A. X. Chavanne, F. Chillà, B. Castaing, B. Hebral, B. Chabaud, and J. Chaussy. Observation of the ultimate regime in Rayleigh-Bénard convection. *Physical Review Letters*, 79(19):3648, 1997.

[18] F. Chillà and J. Schumacher. New perspectives in turbulent Rayleigh-Bénard convection. *The European Physical Journal E*, 35(7):1–25, 2012.

[19] E. S. C. Ching, H. Guo, X.-D. Shang, P. Tong, and K.-Q. Xia. Extraction of plumes in turbulent thermal convection. *Physical Review Letters*, 93(12):124501, 2004.

[20] A. Cimarelli and E. De Angelis. Analysis of the Kolmogorov equation for filtered wall-turbulent flows. *Journal of Fluid Mechanics*, 676:376–395, 2011.

[21] A. Cimarelli and E. De Angelis. Anisotropic dynamics and sub-grid energy transfer in wall-turbulence. *Physics of Fluids (1994-present)*, 24(1):015102, 2012.

[22] A. Cimarelli and E. De Angelis. The physics of energy transfer toward improved subgrid-scale models. *Physics of Fluids (1994-present)*, 26(5):055103, 2014.

[23] A. Cimarelli, E. De Angelis, and C. M. Casciola. Paths of energy in turbulent channel flows. *Journal of Fluid Mechanics*, 715:436–451, 2013.

[24] A. Cimarelli, E. De Angelis, and C. M. Casciola. Paths of energy in turbulent channel flows. *Journal of Fluid Mechanics*, 715:436–451, 2013.

[25] A. Cimarelli, E. De Angelis, J. Jiménez, and C. M. Casciola. Cascades and wall-normal fluxes in turbulent channel flows. *Journal of Fluid Mechanics*, 796:417–436, 2016.

[26] S. Corrsin. On the spectrum of isotropic temperature fluctuations in an isotropic turbulence. *Journal of Applied Physics*, 22(4):469–473, 1951.

[27] F. Dabbagh, F. X. Trias, A. Gorobets, and A. Oliva. New subgrid-scale models for large-eddy simulation of Rayleigh-Bénard convection. In *Journal of Physics: Conference Series*, volume 745, page 032041. IOP Publishing, 2016.

[28] L. Danaila, F. Anselmet, T. Zhou, and R. A. Antonia. Turbulent energy scale budget equations in a fully developed channel flow. *Journal of Fluid Mechanics*, 430:87–109, 2001.

[29] P. A. Davidson, B. R. Pearson, and P. Staplehurst. How to describe turbulent energy distributions without the Fourier transform. In *Proceedings of the Fifteenth Australasian Fluid Mechanics Conference, AFMC 15*. University of Sydney, 2004.

[30] J. W. Deardorff. Three-dimensional numerical study of the height and mean structure of a heated planetary boundary layer. *Boundary-Layer Meteorology*, 7(1):81–106, 1974.

[31] J. A. Domaradzki, W. Liu, C. Härtel, and L. Kleiser. Energy transfer in numerically simulated wall-bounded turbulent flows. *Physics of Fluids (1994-present)*, 6(4):1583–1599, 1994.

[32] T. M. Eidson. Numerical simulation of the turbulent Rayleigh-Bénard problem using subgrid modelling. *Journal of Fluid Mechanics*, 158:245–268, 1985.

[33] M. Germano, U. Piomelli, P. Moin, and W. H. Cabot. A dynamic subgrid-scale eddy viscosity model. *Physics of Fluids A: Fluid Dynamics (1989-1993)*, 3(7):1760–1765, 1991.

[34] G. A. Glatzmaier, R. S. Coe, L. Hongre, and P. H. Roberts. The role of the Earth's mantle in controlling the frequency of geomagnetic reversals. *Nature*, 401(6756):885–890, 1999.

[35] L. R. Glicksman. Energy efficiency in the built environment. *Physics Today*, 61(7):35, 2008.

[36] S. Grossmann and D. Lohse. Scaling in thermal convection: a unifying theory. *Journal of Fluid Mechanics*, 407:27–56, 2000.

[37] S. Grossmann and D. Lohse. Fluctuations in turbulent Rayleigh-Bénard convection: the role of plumes. *Physics of Fluids (1994-present)*, 16(12):4462–4472, 2004.

[38] C. Härtel, L. Kleiser, F. Unger, and R. Friedrich. Subgrid-scale energy transfer in the near-wall region of turbulent flows. *Physics of Fluids (1994-present)*, 6(9):3130–3143, 1994.

[39] D. L. Hartmann, L. A. Moy, and Q. Fu. Tropical convection and the energy balance at the top of the atmosphere. *Journal of climate*, 14(24):4495–4511, 2001.

[40] R. J. Hill. Exact second-order structure-function relationships. *Journal of Fluid Mechanics*, 468:317–326, 2002.

[41] B. Jacob, C. M. Casciola, A. Talamelli, and P. H. Alfredsson. Scaling of mixed structure functions in turbulent boundary layers. *Physics of Fluids (1994-present)*, 20(4):045101, 2008.

[42] K. Julien, S. Legg, J. McWilliams, and J. Werne. Rapidly rotating turbulent Rayleigh-Bénard convection. *Journal of Fluid Mechanics*, 322:243–273, 1996.

[43] L. P. Kadanoff. Turbulent heat flow: Structures and scaling. *Physics today*, 54(8):34–39, 2001.

[44] R. M. Kerr and J. R. Herring. Prandtl number dependence of Nusselt number in direct numerical simulations. *Journal of Fluid Mechanics*, 419:325–344, 2000.

[45] S. J. Kimmel and J. A. Domaradzki. Large eddy simulations of Rayleigh-Bénard convection using subgrid scale estimation model. *Physics of Fluids (1994-present)*, 12(1):169–184, 2000.

[46] E. M. King and J. M. Aurnou. Thermal evidence for Taylor columns in turbulent rotating Rayleigh-Bénard convection. *Physical Review E*, 85(1):016313, 2012.

[47] E. M. King, S. Stellmach, J. Noir, U. Hansen, and J. M. Aurnou. Boundary layer control of rotating convection systems. *Nature*, 457(7227):301–304, 2009.

[48] A. N. Kolmogorov. Dissipation of energy in locally isotropic turbulence. In *Dokl. Akad. Nauk SSSR*, volume 32, pages 16–18. JSTOR, 1941.

[49] A. N. Kolmogorov. The local structure of turbulence in incompressible viscous fluid for very large Reynolds numbers. In *Dokl. Akad. Nauk SSSR*, volume 30, pages 301–305. JSTOR, 1941.

[50] R. H. Kraichnan. Turbulent thermal convection at arbitrary Prandtl number. *Physics of Fluids (1958-1988)*, 5(11):1374–1389, 1962.

[51] R. P. J. Kunnen, H. J. H. Clercx, and B. J. Geurts. Heat flux intensification by vortical flow localization in rotating convection. *Physical Review E*, 74(5):056306, 2006.

[52] R. P. J. Kunnen, B. J. Geurts, and H. J. H. Clercx. Turbulence statistics and energy budget in rotating Rayleigh-Bénard convection. *European Journal of Mechanics-B/Fluids*, 28(4):578–589, 2009.

[53] D. K. Lilly. On the numerical simulation of buoyant convection. *Tellus*, 14(2):148–172, 1962.

[54] D. K. Lilly. On the application of the eddy viscosity concept in the inertial sub-range of turbulence, 1966.

[55] D. K. Lilly. A proposed modification of the Germano subgrid-scale closure method. *Physics of Fluids A: Fluid Dynamics (1989-1993)*, 4(3):633–635, 1992.

[56] S. Liu, C. Meneveau, and J. Katz. On the properties of similarity subgrid-scale models as deduced from measurements in a turbulent jet. *Journal of Fluid Mechanics*, 275:83–119, 1994.

[57] D. Lohse and K.-Q. Xia. Small-scale properties of turbulent Rayleigh-Bénard convection. *Annual Review of Fluid Mechanics*, 42:335–364, 2010.

[58] A Lundbladh, , D. S. Henningson, and A. V. Johansson. An efficient spectral integration method for the solution of the Navier-Stokes equations. *NASA STI/Recon Technical Report N*, 93:29009, 1992.

[59] N. Marati, C. M. Casciola, and R. Piva. Energy cascade and spatial fluxes in wall turbulence. *Journal of Fluid Mechanics*, 521:191–215, 2004.

[60] J. Marshall and F. Schott. Open-ocean convection: Observations, theory, and models. *Reviews of Geophysics*, 37(1):1–64, 1999.

[61] P. J. Mason. Large-eddy simulation of the convective atmospheric boundary layer. *Journal of the Atmospheric Sciences*, 46(11):1492–1516, 1989.

[62] P. J. Mason and D. J. Thomson. Stochastic backscatter in large-eddy simulations of boundary layers. *Journal of Fluid Mechanics*, 242:51–78, 1992.

[63] A. Oberbeck. Über die Wärmeleitung der Flüssigkeiten bei Berücksichtigung der Strömungen infolge von Temperaturdifferenzen. *Annalen der Physik*, 243(6):271–292, 1879.

[64] A. Obukhov. Effect of Archimedean forces on the structure of the temperature field in a turbulent flow. In *Dokl. Akad. Nauk SSSR*, volume 125, page 1246, 1959.

[65] A. M. Obukhov. Structure of the temperature field in turbulent flow. Technical report, DTIC Document, 1968.

[66] R. L. Panton. Overview of the self-sustaining mechanisms of wall turbulence. *Progress in Aerospace Sciences*, 37(4):341–383, 2001.

[67] A. Parodi, J. von Hardenberg, G. Passoni, A. Provenzale, and E. A. Spiegel. Clustering of plumes in turbulent convection. *Physical Review Letters*, 92(19):194503, 2004.

[68] S.-H. Peng and L. Davidson. Comparison of subgrid-scale models in LES for turbulent convection flow with heat transfer. *Turbulent Heat Transfer*, 2:5–24, 1998.

[69] S.-H. Peng and L. Davidson. Large eddy simulation for turbulent buoyant flow in a confined cavity. *International Journal of Heat and Fluid Flow*, 22(3):323–331, 2001.

[70] A. B. Pieri, F. Falasca, J. von Hardenberg, and A. Provenzale. Plume dynamics in rotating Rayleigh-Bénard convection. *Physics Letters A*, 380(14):1363–1367, 2016.

[71] U. Piomelli. Large-eddy simulation: achievements and challenges. *Progress in Aerospace Sciences*, 35(4):335–362, 1999.

[72] U. Piomelli and E. Balaras. Wall-layer models for large-eddy simulations. *Annual Review of Fluid Mechanics*, 34(1):349–374, 2002.

[73] U. Piomelli, W. H. Cabot, P. Moin, and S. Lee. Subgrid-scale backscatter in turbulent and transitional flows. *Physics of Fluids A: Fluid Dynamics (1989-1993)*, 3(7):1766–1771, 1991.

[74] U. Piomelli, T. A. Zang, C. G. Speziale, and M. Y. Hussaini. On the large-eddy simulation of transitional wall-bounded flows. *Physics of Fluids A: Fluid Dynamics (1989-1993)*, 2(2):257–265, 1990.

[75] S. B. Pope. Turbulent flows, 2001.

[76] F. Porté-Agel, M. B. Parlange, C. Meneveau, and W. E. Eichinger. A priori field study of the subgrid-scale heat fluxes and dissipation in the atmospheric surface layer. *Journal of the atmospheric sciences*, 58(18):2673–2698, 2001.

[77] F. Porté-Agel, M. B. Parlange, C. Meneveau, W. E. Eichinger, and M. Pahlow. Subgrid-scale dissipation in the atmospheric surface layer: Effects of stability and filter dimension. *Journal of Hydrometeorology*, 1(1):75–87, 2000.

[78] L. F. Richardson. Weather prediction by numerical process, 2007.

[79] R. S. Rogallo and P. Moin. Numerical simulation of turbulent flows. *Annual Review of Fluid Mechanics*, 16(1):99–137, 1984.

[80] H. T. Rossby. A study of Bénard convection with and without rotation. *Journal of Fluid Mechanics*, 36(02):309–335, 1969.

[81] S. Sakai. The horizontal scale of rotating convection in the geostrophic regime. *Journal of Fluid Mechanics*, 333:85–95, 1997.

[82] U. Schumann. Direct and large eddy simulation of turbulence: Summary of the state of the art 1993. *VKI An Introduction to Modeling Turbulence*, 1, 1993.

[83] A. Sergent, P. Joubert, and P. Le Quéré. Large Eddy Simulation of turbulent thermal convection using a mixed scale diffusivity model. *Progress in Computational Fluid Dynamics, an International Journal*, 6(1-3):40–49, 2006.

[84] O. Shishkina and C. Wagner. Analysis of sheet-like thermal plumes in turbulent Rayleigh-Bénard convection. *Journal of Fluid Mechanics*, 599:383–404, 2008.

[85] E. D. Siggia. High Rayleigh number convection. *Annual Review of Fluid Mechanics*, 26(1):137–168, 1994.

[86] J. Smagorinsky. General circulation experiments with the primitive equations: I. the basic experiment. *Monthly weather review*, 91(3):99–164, 1963.

[87] R. J. A. M. Stevens, H. J. H. Clercx, and D. Lohse. Heat transport and flow structure in rotating Rayleigh-Bénard convection. *European Journal of Mechanics-B/Fluids*, 40:41–49, 2013.

[88] R. J. A. M. Stevens, R. Verzicco, and D. Lohse. Radial boundary layer structure and Nusselt number in Rayleigh-Bénard convection. *Journal of Fluid Mechanics*, 643:495–507, 2010.

[89] D. J. Tritton. *Physical fluid dynamics*. Springer Science & Business Media, 2012.

[90] P. C. Valente and J. C. Vassilicos. The energy cascade in grid-generated non-equilibrium decaying turbulence. *Physics of Fluids (1994-present)*, 27(4):045103, 2015.

[91] E. R. Van Driest. On turbulent flow near a wall. *Journal of the Aeronautical Sciences*, 2012.

[92] M. Van Reeuwijk, H. J. J. Jonker, and K. Hanjalić. Identification of the wind in Rayleigh-Bénard convection. *Physics of Fluids (1994-present)*, 17(5):051704, 2005.

[93] R. Verzicco and R. Camussi. Numerical experiments on strongly turbulent thermal convection in a slender cylindrical cell. *Journal of Fluid Mechanics*, 477:19–49, 2003.

[94] A. Vögler, S. Shelyag, M. Schüssler, F. Cattaneo, T. Emonet, and T. Linde. Simulations of magneto-convection in the solar photosphere-equations, methods, and results of the MURaM code. *Astronomy & Astrophysics*, 429(1):335–351, 2005.

[95] B. Vremen, B. Geurts, and H. Kuerten. Large-eddy simulation of the turbulent mixing layer. *Journal of Fluid Mechanics*, 339:357–390, 1997.

[96] P. Wei, S. Weiss, and G. Ahlers. Multiple Transitions in Rotating Turbulent Rayleigh-Bénard Convection. *Physical Review Letters*, 114(11):114506, 2015.

[97] T. Weidauer, O. Pauluis, and J. Schumacher. Cloud patterns and mixing properties in shallow moist Rayleigh-Bénard convection. *New Journal of Physics*, 12(10):105002, 2010.

[98] V. C. Wong and D. K. Lilly. A comparison of two dynamic subgrid closure methods for turbulent thermal convection. *Physics of Fluids (1994-present)*, 6(2):1016–1023, 1994.

[99] M. Wörner and G. Grötzbach. Pressure transport in direct numerical simulations of turbulent natural convection in horizontal fluid layers. *International Journal of Heat and Fluid Flow*, 19(2):150–158, 1998.

[100] H.-D. Xi, Q. Zhou, and K.-Q. Xia. Azimuthal motion of the mean wind in turbulent thermal convection. *Physical Review E*, 73(5):056312, 2006.

[101] A. M. Yaglom. On the local structure of a temperature field in a turbulent flow. In *Dokl. Akad. Nauk SSSR*, volume 69, page 743, 1949.

[102] Q. Zhou, C. Sun, and K.-Q. Xia. Morphological evolution of thermal plumes in turbulent Rayleigh-Bénard convection. *Physical Review Letters*, 98(7):074501, 2007.

List of pubblications

[L1] A. Cimarelli, R. Togni, and E. De Angelis. Analysis of the Yaglom equation and subgrid modelling approaches for thermally driven turbulence (extended abstract). In *15th European Turbulence Conference, ETC 15*. TU Delft, 2015.

[L2] R. Togni, A. Cimarelli, and E. De Angelis. Production scales and spatial fluxes in turbulent Rayleigh-Bénard convection. In *Proceedings of THINS 2014 International Workshop*. Università degli Studi di Modena e Reggio Emilia, 2014.

[L3] R. Togni, A. Cimarelli, and E. De Angelis. Analysis of turbulent Rayleigh-Bénard convection in the compound physical/scale space domain (extended abstract). In *15th European Turbulence Conference, ETC 15*. TU Delft, 2015.

[L4] R. Togni, A. Cimarelli, and E. De Angelis. Physical and scale-by-scale analysis of Rayleigh–Bénard convection. *Journal of Fluid Mechanics*, 782:380–404, 2015.

[L5] R. Togni, A. Cimarelli, and E. De Angelis. Multi-scale analysis of turbulent Rayleigh-Bénard convection. In *Progress in Turbulence VI*, pages 295–298. Springer International Publishing, 2016.

[L6] R. Togni, A. Cimarelli, and E. De Angelis. Towards an improved subgrid-scale model for thermally driven flows. In *Progress in Turbulence VII*. Springer International Publishing (accepted for publication), 2016.

[L7] R. Togni, A. Cimarelli, A. Lozano-Durán, and E. De Angelis. Space and time behaviour of the temperature second-order structure function in Rayleigh-Bénard convection. *Journal of Physics: Conference Series*, 708:012007, 2016.